DESIGN, FABRICATION AND PERFORMANCE TESTING OF A TWISTED 2-BLADED HORIZONTAL AXIS WIND TURBINE

by
Ronit Kumar Singh

A thesis submitted in fulfillment of the
requirements for the degree of
Master of Science in Engineering

School of Engineering and Physics
Faculty of Science, Technology and Environment
The University of the South Pacific
Suva, Fiji Islands

March, 2012

Declaration of Originality

I hereby declare that the write up of the research project is purely my own work without the inclusion of any other research materials that has already been published or written. Any individuals' work or idea that has been included within the report has been clearly referenced and credit given to the person.

…….

Ronit Kumar Singh

S11012928

20/03/2011

I hereby confirm that the work contained in this supervised research project is the work of Ronit Kumar Singh unless otherwise stated.

……

Dr. M. Rafiuddin Ahmed

Principal Supervisor

20/03/2011

Acknowledgement

I would foremost like to acknowledge the presence of almighty God in my life for giving me the wisdom, knowledge and vision to endeavor into the research project that I chose because of my interest and have it finished successfully.

I would like to thank my mother for pushing me to strive forward with my project and my extended family for their encouragement and support.

I give my sincere thanks to my supervisor Dr. M. Rafiuddin Ahmed for his guidance, patience and support in my MSc research project.

Finally I would like to thank the staff of the School of Engineering and Physics, Clay Energy and CBS power solutions for their advice, support and technical assistance to the project. Without their help the project would not have been a success. I would like to thank the technicians of the metal workshop and electrical and electronics division: - Mr. Shui Dayal, Mr. Sanjay Singh and Mr. Iafeta La'ava (Jeff) for their advice and assistance in the manufacture of airfoil sections and other technical dealings of the project. I thank the staff and technicians of the Physics division: - Mr. Viti Buadromo, Mr. Radesh Lal, Mr. Joape, Mr. Amit Deo, Mr. Shanil Deo, Mr. Neil and Mr. Rajneel Prasad for their continuous advice and assistance and help with data acquisition, a vital component in the finalization of the project.

To my colleagues Mr. Sumesh Narayan, Dr. Rajeshkannan Ananthanarayanan, Mr. Hamendra Reddy, Dr. Daniel M. Wood Mr. Mohammed Tazil, Mr. Sheikh Izzal, Mr. Krishneel Ram, Mr. Mohammed Faizal, Mr. Shivneel Prasad, Mr. Sandeep Patel and Mr. Jai Goundar many thanks for their endless support and eager help during all the stages of my MSc research project.

I would like to thank all of you once again for making me accomplish my Masters Degree, a big milestone in my life's journey, destined for the purpose as God intended.

Nomenclature

A rectangular area of airfoil = chord x span (m^2)

a axial induction factor (dimensionless)

b span of airfoil (m)

c chord length of airfoil (m)

C test section cross sectional area (m^2)

C_p coefficient of pressure (dimensionless)

C_P coefficient of power (dimensionless)

C_L coefficient of lift (dimensionless)

C_{Lmax} maximum coefficient of lift at stalling angle (α_{stall}) (dimensionless)

C_D coefficient of drag (dimensionless)

C_n coefficient of normal force (dimensionless)

d local diameter (m)

D total diameter (m)

D drag force (N)

dr blade elemental section

dT tangential force (N)

dN normal force (N)

dL lift force (N)

dD drag force (N)

dM torque (Nm)

F Prandtl tip loss factor

K_1 wind-tunnel correction constant for solid blockage effects (0.74)

K acceleration factor ($K > 0$)

L lift force (N)

M_v model volume (m^3)

N_b number of blades present

P_∞ freestream static pressure (Pa)

P_T total pressure (Pa)

P_{atm} atmospheric pressure (101.3kPa)

P_i incremental airfoil surface pressure (Pa)

r local radius (m)

r_1 incremental distance from the centre of the rotor blade to the radial location of one of the airfoil sections

R total radius (m)

R gas constant (0.287 kJ/kg.K)

Re $\rho V_\infty c/\mu$, Reynolds number (dimensionless)

T ambient air temperature (Kelvin)

V_∞ freestream velocity (m/s)

V_u uncorrected freestream velocity (m/s)

V_{rel} relative velocity (m/s)

V_{axial} axial component of velocity triangle (m/s)

V_{tan} tangential component of velocity triangle (m/s)

V_D velocity upstream of actuator disc (m/s)

x distance measured along chord line from leading edge (m)

a' tangential induction factor (dimensionless)

α angle of attack (angle between the freestream flow direction and chord line of airfoil) (°)

α_{stall} stalling angle of attack where maximum value of lift coefficient occurs (°)

α_o angle of attack at zero lift (°)

α_t angle of attack measured at the tip of rotor blade (°)

β pitch angle measured between rotor plane of rotation and chord line (°)

β_t pitch angle measured at the tip of the rotor blade (°)

Φ angle between rotor plane of rotation and V_{rel} (degrees)

ω angular velocity of rotor blades (rad/s)

ε^{sb} solid blockage correction factor

σ rotor solidity (dimensionless)

μ dynamic viscosity (kg/(m.s))

ρ density of air (kg/m^3)

λ tip speed ratio (TSR) (dimensionless)

Ψ wind turbine rotor azimuth angle (°)

γ yaw angle measured between wind direction and axis of rotation (°)

Abstract

The introduction of micro and small horizontal axis wind turbines in Fiji are 'off the shelf' products that are not tailored to the low wind conditions of Fiji. These 'off the shelf' wind turbines produce effective power at wind speeds above the average wind speeds of 5 – 6m/s experienced in Fiji [1] and thus the probability of producing effective power is very low. A low speed wind turbine that is tailored for Fiji's wind conditions is thus vital.

The Masters thesis undertaken focuses on the designing of a low speed rotor of a small, 400W wind turbine suited for effective operation at 5m/s wind speeds. Since the rotor blades are the primary energy extracting device of a wind turbine, its optimization is of utmost importance in increasing the overall efficiency of the wind turbine.

As part of rotor design, extensive design and testing went into low Reynolds number, high lift airfoils. The new airfoil designated as *airfish AF300* airfoil was used for the rotor blade section. As part of geometry optimization, the AF300 airfoil has a flatback trailing edge benefiting the rotor design aerodynamically and structurally. The operation of the AF300 airfoil was carried out in the Reynolds number range of 38000 – 205000 (6 – 32m/s freestream velocity). It was found that the airfoil performed well from Re = 75000 to Re = 205000, showing attached flow regime up to a stall angle of attack of 14°. At Reynolds numbers of 75000, 128000 and 205000; C_{Lmax} = 1.72, 1.81 and 1.86 respectively at the stall angle, α_{stall} of 14°. The lift coefficient increased from 0.41 to 1.05 at Re = 38000 in α range of 0° to 18°, in which no stalling was documented. Computational fluid dynamics (CFD) was performed as a validation to experimental results with smoke flow visualization done to analyze the flow around the airfoil.

A 2-bladed system was incorporated with an Air X marine wind turbine with the AF300 airfoil section and chord and twist distribution for an increased performance. The pitch of the blade was changed to yield maximum performance and faster startup time. Pitch angle setting of 15, 18 and 20° was set for the blades for the field test with the turbine performing best at 18°. On average the wind turbine yielded an efficiency of 25.5% at an altitude of 8m above sea level at a wind speed of 6m/s and 18° pitch angle. Maximum efficiency based on 10sec data at 6m/s was 29.1%. The turbine performance ranged from 0.41 – 25.5% in the wind speed range of 3 – 6m/s. Cut-in

wind speed for the wind turbine at the optimum pitch angle was 3.24m/s. In comparison with the stock 3-bladed rotor, the new 2-bladed rotor produced more electrical power at the same given freestream velocities. Turbine performance of Air X marine wind turbine with the stock rotor ranged from 0 – 14.96% in V_∞ range of 3 – 6m/s.

Table of Contents

List of Figures

List of Tables

Chapter 1 Introduction

Renewable energy resources within the Pacific region have not been fully exploited; wind, solar and wave that are potential sources of clean energy available in abundance to the Pacific Island countries (PIC's). With extensive resource assessment of these renewable energy sources, implementation of properly sized renewable energy devices such as wind turbines, solar photo voltaic, tidal current turbines and oscillating water columns can be placed in locations where the viable sources of renewable energy are available. Such implementation of renewable energy devices have already been carried out in the Fiji Islands but at a small scale. A 10MW wind farm in Butoni, Sigatoka and 10kW photo voltaic solar panels at Navutu, Lautoka have been proposed and embarked on by the national electricity provider, Fiji Electricity Authority (FEA) in its quest to lower the consumption of fossil fuels to produce electricity.

Fiji is not a windy place and experiences, on average 5 – 6m/s wind speeds only [1]. Electricity produced in Fiji comes from a combination of hydro dams, wind power, solar, biomass and diesel of which diesel supplies 50% of the total electric power generated [1]. The total national electricity produced in Fiji reaches to only 70% of the total population. The other 30% of the total population are at a disadvantage as they live in communities that are mostly isolated from one another and situated in remote places, out of reach of the more reliable national electricity grid lines. Therefore the introduction of wind turbines and solar systems to the domestic sector seems inexpensive and feasible.

The present research paper aims to attain a high level of performance from a small horizontal axis wind turbine rated at 400W with a 1.26m, 2-bladed rotor designed for low *Re* application in the wind speed range of 3 – 6m/s. The blades incorporate twist, taper and a low *Re* AF300 airfoil throughout the blade cross section to yield good performance in the low wind conditions experienced in Fiji. The AF300 airfoil was designed to operate in the *Re* range of 0.75×10^5 to 2×10^5 for application on rotor blades of the small wind turbine. The AF300 airfoil has a flatback trailing edge for structural integrity and to achieve a high stalling angle of 14°.

1.1 Objectives

The aim of the thesis is to design an aerodynamically efficient 2-bladed rotor for a small wind turbine for operation in the low wind speed range of 3 – 6m/s. The objectives are as follows:-

- Form a database of low Reynolds number airfoils and test their aerodynamics characteristics using xfoil software. Choose and rank best airfoils accordingly and improve their geometry to achieve optimum aerodynamic properties for application under low Reynolds numbers.

- Devise a method and a qualitative approach in manufacturing test airfoils for testing the new airfoil in the wind tunnel for evaluation.

- Validate experimental results with CFD and xfoil results

- Perform smoke flow visualization in the wind tunnel together with P.I.V tests to observe flow phenomenon common to low *Re* airfoils like flow separation on the airfoil top surface.

- To design rotor blades for Air X wind turbine for low wind speed application of 3 – 6m/s through the use of BEM theory by adding taper and twist to the rotor geometry.

- To plan a procedure for the accurate and identical fabrication of the 2 blades from wood together with the hub and pitch control mechanism.

- Field test the blades on the Air X wind turbine and evaluate its performance for low wind speed application at different pitch angles.

- Compare the designed 2–bladed rotor to the 3–bladed stock rotor of Air X wind turbine.

1.2 Thesis structure

The thesis is divided into three major parts that makes the idea of a small wind turbine rotor, suited for Fiji's low wind speed condition a reality. These 3 major parts consists of:-

1 - airfoil design for low Reynolds number application

2 - rotor blade design

3 - fabrication and field testing of rotors for performance evaluation under low wind speed conditions.

These 3 parts incorporate 6 chapters that are as follows:-

Chapter 2 provides an overview on the historical background on wind turbines that narrows down to small horizontal axis wind turbines, discussing the importance of small wind turbines and its place in society. Lastly the aerodynamic operation and extraction of energy of the rotor blades in low wind conditions is discussed in detail.

Chapter 3 presents the design process of choosing and optimizing airfoil geometry for small wind turbine rotor blades. In this chapter low Reynolds number airfoils are chosen, tested, evaluated and optimized through geometric alterations in *xfoil* software to yield optimum aerodynamic performance at the set Reynolds number range.

Chapter 4 evaluates the aerodynamic performance of the new low Reynolds number airfoil designated as AF300 through wind tunnel testing, smoke flow visualization, particle image velocimetry (PIV) and through numerical simulation through computational fluid dynamics (CFD) – *ansys* CFX. It discusses the airfoil's aerodynamic properties that include lift, lift to drag ratio, stalling angle of attack and most importantly flow separation on the upper surface of airfoil.

Chapter 5 presents the design process for blade design for low wind speed application. The blade design is based on criteria dictated by conditions faced by a small wind turbine. *Blade element momentum* (BEM) theory was used to provide the chord and twist distribution to the rotor.

Lastly, the chapter discusses some of the technicalities of the manufacturing process of the rotor blades in brief.

Chapter 6 evaluates the performance of the 2-bladed rotor on an Air X 400W wind turbine. The first half of the chapter provides detailed methodology of the field testing of the wind turbine with the new low wind speed rotors at different pitch angles. The second part presents the analysis and discussion of the results obtained from the field tests and compares the performance of the new rotor with the stock 3-bladed rotor of Air X wind turbine.

Chapter 7 provides the conclusion to the results from the preceding chapters.

Chapter 2 Literature Review

2.1 Background

Wind turbines are popular energy harnessing devices that produce electrical power derived from the wind. The idea of power extraction from the wind goes back hundreds of years. Windmills and wind wheels were used in the past centuries to grind wheat and pump water for irrigation. As these windmills evolved, they were able to yaw into the wind and the blades could be pitched to fully utilize the kinetic energy available in the wind just like modern wind turbines. Yawing was accomplished passively by a fan tail that positioned the main rotors of the windmill into the wind, mechanically. Windmills survived into the mid 20th century and declined slowly at first due to industrialization and the introduction of steam power. Windmills died altogether due to electrification of the rural areas [2]. All in all there were around 200,000 windmills around Europe with Netherlands having 9,000 and Germany, 29,000 [2]. During the periods of 17th and 18th century scientific development evolved from ideas in the Renaissance era from artists like Leonardo da Vinci. These were basically novice ideas which held no scientific fundamental grounds. Nevertheless the novice and novel ideas were realized and made real by the likes of Gottfried Wilhelm Leibniz (1646–1716) who made new windmill designs, Daniel Bernoulli (1700–1782) who applied the famous basic laws of fluid mechanics to the design of windmill sails and mathematician Leonhard Euler (1707–1783), who pioneered in the calculation of twist in the sail rotors of a windmill [2].

2.2 The evolution of wind turbines

The idea of generating electricity from wind power began as early as the 19th century. Generation of electricity by means of coal and fossil fuels had already begun in the late eighteen hundreds. As a result there was rapid movement towards electrification of cities and rural areas in America and Europe, although electricity was slow to reach the greater parts of the rural areas. In response to this, generation of electricity from the wind was pioneered. The first person to generate electricity from wind through a wind turbine was Poul La Cour. Poul La Cour perfected windmill technology and developed the first commercial wind turbine in 1891 [2]. He was one of the first to start wind tunnel tests of wind turbines [2]. The idea of generating electricity from wind turbines was of little importance in the mid 19th century due to abundance of fossil fuels like coal and petroleum. Not until the break of World War 2, did interest kindle into wind turbine

technology due to the increase in fuel prices. Research into wind turbine technology continued to grow, with Germany investing into large scale off-shore wind turbines. During the post-War times the developments of wind turbines progressed slowly since the fuel prices after World Wars had normalized. In relation to power from crude oil, wind power had no chance economically of competing with the primary energy source. The global fuel crises of 1973 rekindled interest in wind turbines again when the price of crude oil had risen a number of times its normal price [2,3]. During these hard times, interest into renewable energy sources grew. The western industrialized countries poured in millions of dollars in revenue for research and development of large scale wind turbines for the industrial sector and small scale wind turbines for the domestic sector. The 1980s saw a large investment in large scale wind turbines like the MOD series wind turbines, Nibe, Growian and Darrieus types [2]. These were experimental wind turbines which were later commercially produced to produce power in isolated systems or as clusters (wind farms). Interest in small wind turbines was little as there was a need to boost the energy sector with power generated from wind turbines on a large scale which could only be met by large wind turbines.

2.3 Types of wind turbines and their basic operations

In general wind turbines are categorized into horizontal and vertical axis wind turbines (HAWT and VAWT). The first one has its rotor axis positioned horizontally while the latter has it in a vertical position. Vertical axis wind turbines are of many types but the 3 most important or the ones that have been developed on a commercial scale are the Darrieus, savonius and the H-type rotor turbines. Of the 3, the savonius rotor is a drag device while the other 2 rotors are lift devices. Although simple in design, these VAWTs are not as popular as the HAWTs. The Derreus and H-type rotors may sometimes require external power to startup and have low tip speeds as they are on the ground where the wind velocity is very less. Power output cannot be regulated by the Darrieus turbine as there is no pitch control present. The savonius rotor being a drag device has low tip-speeds and can produce a maximum efficiency of 25% [2]. Its application is therefore limited and is not suited to produce power at a large scale.

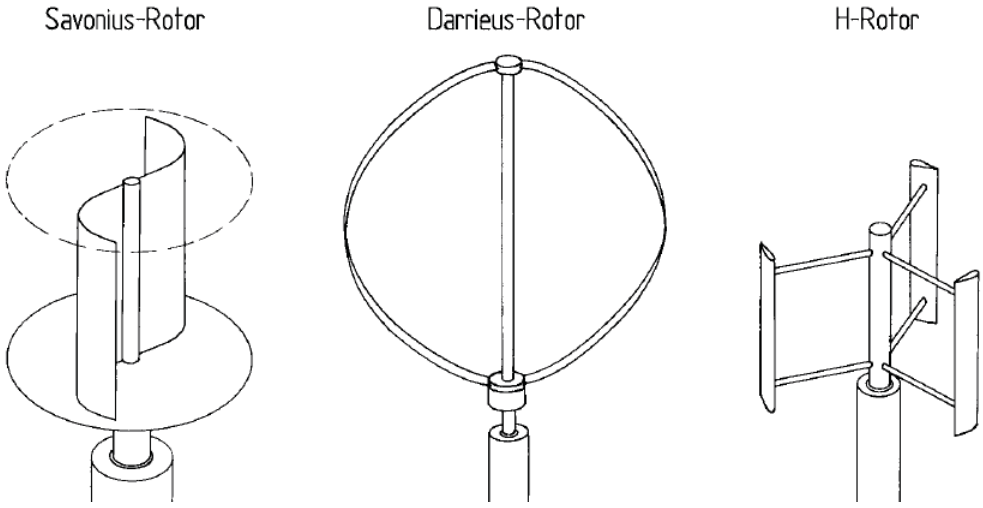

Fig. 2.1 The 3 most common types of vertical axis wind turbines [2]

The HAWTs operate on the principle of aerodynamic lift and thus the blades can be optimized to yield more power and efficiency. Due to a propeller like design, the blades can be pitched to varying angles to regulate power output and safeguard the turbine from strong winds. Pitch control is the main form of protection and power regulation in large and small wind turbines alike.

Horizontal axis wind turbines are further classified as up-wind and down-wind systems. For up-wind, the rotors are the first to make contact with the wind followed by the turbine nacelle and then the tower. For a downwind turbine the nacelle is the first to make contact with the wind followed by the tower and lastly the rotors. Both have their advantages and disadvantages. Upwind turbines need passive or active form of yaw control while downwind turbines turn automatically into the wind due to the placement of the rotor hub with respect to yaw axis and incoming wind direction. With the rotor plane behind the yaw axis of rotation, moment due to change in wind direction causes the system to easily yaw. This is not possible with up-wind turbines as the rotor plane with respect to the oncoming wind is very close to the yaw axis.

HAWTs can have any number of rotor blades irrespective of them being upwind or downwind. Turbines can have rotors starting up with just one blade to many. The most common configuration is 2 or 3 blades. A 2-bladed rotor operates at a greater tip speed ratio (TSR) compared a 3-bladed rotor but generates a less amount of torque. Both have their advantages and

disadvantages. The initial cost of a 2-bladed turbine is less compared to a 3-bladed turbine of the same diameter and comparable power output as it has less rotor solidity, σ due to a higher TSR [2]. Three bladed turbines operate at lower rpm compared to 2-bladed configurations making them less noisy and low maintenance. At higher TSR, a 2-bladed configuration eliminates the need for a gearbox and can be made having less structural strength as compared to 3-bladed turbine as a 2-bladed turbine encounters less thrust force. Due to the 3-bladed configuration, there is less dynamic loading on the turbine structure and the operation of the blades is less disturbing to the eyes compared to a 2-bladed rotor.

2.4 Improving performance of HAWTs

Ideally a horizontal axis wind turbine can extract energy up to Betz limit of 59.2% [4]. It is the theoretical maximum that a HAWT can extract of the kinetic energy available in the wind. Wind turbines developed so far have power coefficient ranging from 20-45% [4,5]. It is known that by increasing the flow of air there is dramatic increase in the available power to the turbine due to the fact that power from the wind is proportional to the cube power of wind velocity [6]. An increase in flow velocity by 2 times increases the available power by eight folds. To achieve power coefficients within the range of Betz limit, static, non-rotating devices have been used around the wind turbine to increase the primary source of energy by increasing its flow velocity across the rotor blades. Devices like shrouds or ducts, vortex towers, concentrators and thermal updrafts have all aided in performance increase of wind turbines that exceeds Betz limit. Ducts around the periphery of the wind turbine increase the turbine power by not allowing the approaching stream of air in front of the rotors from narrowing down. The result is an increase in performance that exceeds the Betz limit. Reents [7] investigated ducted turbines and found that the duct increased performance of the turbine to 0.66. A diffuser duct was also proposed by Abe and Nishida [6]. They developed a flanged diffuser that increased the power coefficient of the wind turbine by 4 times compared to a bare turbine. The flanged diffuser increased the pressure difference across the wind turbine resulting in the acceleration of flow across the turbine blades. Similar results were presented by Wang and Bai [3] where a contractor-diffuser scoop increased the power of a small wind turbine by 2.2 times compared to a bare turbine. Another type of device known as the vortex tower increases performance of the turbine by inducing vortex to the flow above the turbine blades that result in a low pressure region inside the rotating vortex of air.

Vortex is generated by means of vertical slatted openings on the cylinder walls that house the turbine. Air flows in tangentially around the vertical windows around the cylinder causing generation of vortex inside, above the turbine. Air is then sucked from below and the accelerated flow across the turbine increasing its performance. A thermal updraft power plant is another device that works like the vortex tower, but instead of vortex generation, it uses thermal energy from the sun to accelerate flow across the turbine that is inside the thermal draft tube. Air beneath the collector roof is heated by the sun and begins to rise in the duct across the turbine and out through the chimney tower due to difference in air density caused by a difference in air temperature between air under the collector roof and the surrounding air near the ground. In contrast to other devices which merrily increase the flow rate of the natural wind, a solar updraft power plant generates the full flow through the duct to the turbine with the help of solar radiation. Although all these devices help to increase the performance of the wind turbine to and in excess of Betz limit, the cost of material, manufacture and installation are too great and become decisive factors in deciding the functionality of such devices to be used with turbines for power generation.

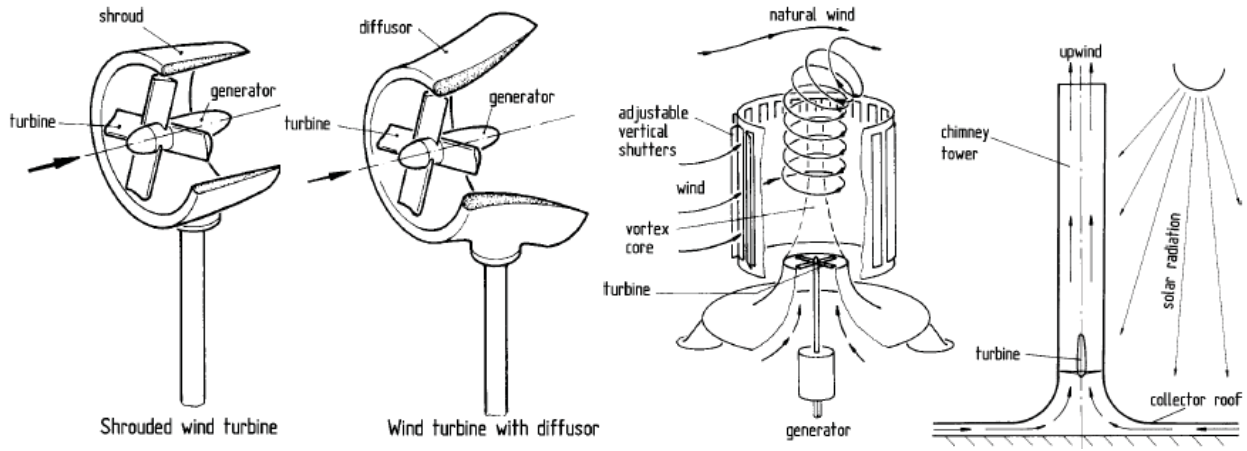

Fig. 2.2 Devices that increase performance of a wind turbine by accelerating flow across it. [2]

2.5 Small wind turbines

Growing awareness of rising levels of greenhouse gases [8], global warming and increasing prices of fossil fuels have led to a shift towards investing into low-cost small wind turbines. Simple structure, compact in design, portable and low noise [9] make small wind turbines vital wind power extracting devices in the rural, suburban and even in the populated city areas where installation of large scale wind turbines would not be accepted due to space confinement and

generation of noise. Compared to large turbines which have performance around 45%, small wind turbines are able to operate at 30% or greater efficiency [10]. Small wind turbines have been integrated on domestic house roof tops, farms, remote communities and boats [4]. In contrast to larger horizontal axis wind turbines (HAWT's) that are located in areas dictated by optimum wind conditions, small wind turbines are required for producing power without necessarily the best of wind conditions [3,4,11]. A small wind turbine is one that relies on aerodynamic forces to start and has a tail vane for passive yawing. Small wind turbines are categorized as micro (1kW), mid-range (5kW) and mini wind turbines (20kW+) [12]. A more detailed description of micro wind turbines is given by Cooper [8] as rated less than 2.5kW and commercially produces power in the range of 0.4kW – 1.5kW at 12.5m/s wind speed. Although the potential of small wind turbines is great in the sense that it is able to supply power to rural to metropolitan dwellings easily and cost effectively, they have not been widely accepted. This is due to the fact that small wind turbines operate in low wind conditions, which coupled with high turbulence degrades the kinetic energy extractable by the wind turbine. Together with low availability of wind speeds, small wind turbines operate at very high tip speed ratios, or high rpm. This produces aerodynamic noise that diminishes the popularity of small wind turbines and their acceptance into society even further [8,13].

Table 2.1 Categorization of small wind turbines according to their power output and rotor sizes [11]

Category	Power (kW)	Radius (m)	Max rotor speed (rpm)	Typical uses	Generator type(s)
Micro	1	1.5	700	Electric fences, yachts	Permanent magnet (PM)
Mid-range	5	2.5	400	Remote houses	PM or induction
Mini	20+	5	200	Mini grids, remote communities	PM or induction

2.6 Laminar separation bubble

Small wind turbines operate within 100 m above sea level where the lowest portion of the planetary boundary layer (PBL) is found. Within the PBL, the laminar air flow is made turbulent and slowed down by obstacles and topology [3,4,13]. Due to their small rotor size and low wind speeds; small wind turbines operating at low Reynolds numbers suffer from laminar separation

bubble [10,14,15]. Laminar separation bubble is a phenomenon associated with low Reynolds number where laminar flow separates before it can transit to turbulent flow as a result of adverse pressure gradient, APG [16]. The separated laminar flow gets re-energized and reattaches back to the surface as turbulent flow forming the so called separation bubble. The separation bubble leads to an increase in the boundary layer thickness above it causing excessive increase in pressure drag, a loss in aerodynamic lift and noise [11,15,17]. Separation bubble degrades the overall aerodynamic performance of an airfoil resulting in the reduction of a turbine's startup and power coefficient [4].

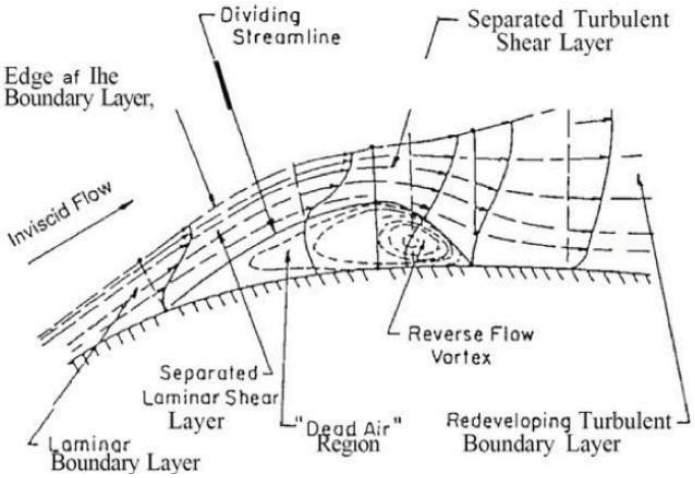

Fig. 2.3 Laminar separation bubble that is associated with low number Reynolds number airfoils [4]

2.7 Low Reynolds number airfoils for small wind turbines

Low *Re* airfoils operate below *Re* = 500,000 [15,18,19] where the flow across the upper surface of the airfoil is predominantly laminar. Airfoils within this *Re* range suffer from laminar separation bubble and are susceptible to laminar flow separation that occurs when the laminar separated flow does not reattach to the surface, downstream of the flow, resulting in loss in aerodynamic performance. Low *Re* airfoils suited for small wind turbine application must be designed to have a high degree of tolerance in avoiding high leading suction peaks and high adverse pressure gradients that leads to laminar flow separation. A small degree of roughness needs to be associated with airfoils operating at low *Re* conditions as explained by Lissaman [20] where introduction of 'turbulators' or trip wire devices, promote early transition from laminar to turbulent flow to eliminate laminar separation bubbles and delay the possible chance of separation from the upper surfaces at higher angles of attack. The use of specifically sized trip

wires has been employed near the leading edges of high *Re* airfoils to show this effect as studied by Selig and Giguère [15] where the devices 'trip' laminar flow into high energy turbulent flow able to negotiate the APG. Roughness can easily be introduced to airfoils at low *Re* as it does not appear significant in relation to boundary layer thickness whereas the opposite happens at high *Re.* Since boundary layer thickness is inversely proportional to *Re*, a small amount of roughness would appear noticeable with decreasing boundary layer thickness as *Re* is increased as the physical size of the introduced roughness stays same [10]. Figure 2.6 shows the effects of surface roughness on the Go 769 airfoil with respect to Reynolds number with increasing *Re*. Since the effects of roughness is inversely proportional to *Re*, boundary layer thickness decreases, increasing the effects of drag and decreasing lift. For low *Re* airfoils, low *Re* promotes a thick boundary layer whereby the effects of roughness becomes negligible.

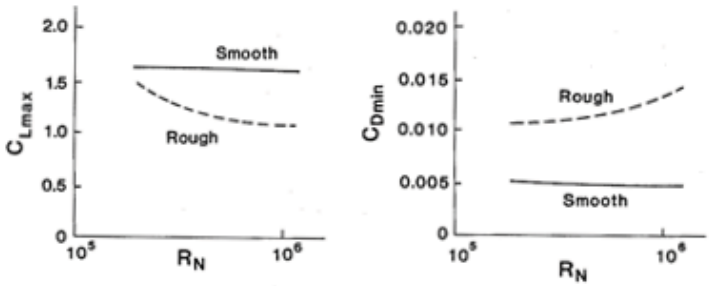

Fig. 2.4 Effects of surface roughness of Go 769 airfoil on the lift and drag coefficients with increasing *Re* [18]

2.8 Airfoil shape, magnitude of maximum suction peak and adverse pressure gradient

Low *Re* airfoils are designed to be thinner than traditional airfoils that operate at high *Re* [11,15, 21]. Thin airfoils are chosen for low *Re* application to decrease the suction peak near the leading edge of the airfoil to decrease the APG on the upper surface [18,20]. A decrease in APG ensures that the laminar flow does not separate from the surface. Selig and Giguère [21] discuss the use of thin airfoil that consist of SG60XX series of thin airfoil families (SG6040 – SG6043) suited for application in small wind turbine blades operating in the *Re* range of 1 x 10^5 – 5 x10^5. Selig and Giguère [15] in another paper discuss the applicability of 15 airfoils consisting of mainly thin airfoil, along the span of small wind blades. Other geometric parameters such as the increasing of leading edge nose radius and cusping of trailing edge have increased aerodynamic performance at the low *Re.* Increasing nose radius decreases APG and cusping of trailing edge increases aerodynamic loading within the cusped region [22]. A cusped trailing edge is

compatible with a concave pressure recovery and has the least amount of pressure drag [23]. Such airfoils have been proposed for small wind turbines by Selig and McGranahan [14] where test of 6 airfoils was conducted in the *Re* range of $10^5 – 5 \times 10^5$ of which 2 airfoils (SH3055 and FX63-137) were cusped. These airfoils produced C_L values of around 1.75 in the set *Re* range. Likewise Henriques and Silva [24] developed a new high lift cusped airfoil (T.Urban 10/193) characterized to work well within the urban environment through xfoil. The airfoil produced C_L values close to 2 in the *Re* range of $6 \times 10^4 – 1 \times 10^6$.

In the figure 2.7 airfoils 1-3 show different upper surface maximum peaks as a result of the difference in their geometry. The higher the upper surface suction, the greater the APG to which the accelerated flow would have to recover to. Greater suction means higher acceleration in the upper surface which means greater generation of lift. Airfoils 1 and 2 have the same maximum low pressure on the upper surface but different pressure for the lower surfaces. Airfoil 2 has greater lower pressure compared to airfoil 1 and thus has more APG on the lower surface than airfoil 1. Airfoil 3 has less low pressure on the upper surface and produces most of its lift from the high pressure on the lower surface. Airfoil 2 is suited for high Reynolds number application whereas airfoil 3 for low *Re* application because with low *Re*, the flows ability to stay turbulent decreases and majority of the flow (almost 75%) across the upper surface is laminar. Laminar flow does not have the ability to overcome high APG and thus the particular shape of airfoil 3 to decrease the upper surface APG. It is noticed that low *Re* airfoils are thinner in nature to have minimum APG. Flow would certainly separate from airfoils 1 and 2 at low *Re* operation as the laminar flow across the upper surface would not be able to negotiate the high APG offered by these two airfoils and separate. Small wind turbines can have thin airfoil sections without the need for high strength and expensive blade materials to sustain against the effects of thrust from the wind as they operate at high rpm. The high rpm of the blades induces a very strong centrifugal force causing the blades to be stiff and maintain parallelism with the rotor plane of rotation.

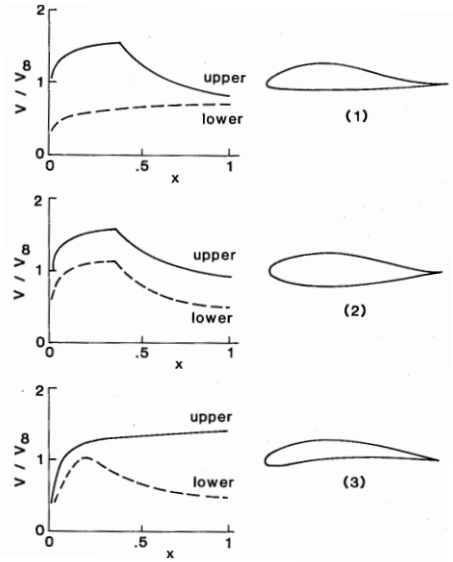

Fig. 2.5 Low *Re* airfoil geometry selection based on the upper surface and lower surface pressure distributions [18]

2.9 Small wind turbine rotor blades

It is mainly the size of the rotor blades that determine whether the airfoil section is a low *Re* airfoil or a high one. Smaller blades of radius 2 meters and below combined with low wind conditions leads to the blades operating at low Reynolds numbers from the root to tip [21]. The smaller sized blades have smaller airfoil chord size contributing to operation at low Reynolds numbers in low wind speed conditions.

It is vital that small wind turbine rotors have a good startup response to low wind speeds in order to generate maximum possible power [4,15,24]. Most of the starting torque comes from near the blade root whereas the tip generates most of the power producing torque [25] as shown below in figure 2.6. During the startup the starting torque of small wind turbines is small due to their small rotor size making it insufficient to start at low wind speeds [11]. Small wind turbines suffer from a lot of resistive torque generated by friction linked to gearbox train, bearings and generator, all of which the rotor has to overcome before it can start rotating. As wind turbines get smaller, cogging friction associated with the generator increases [25] as most of the generators are of the synchronous permanent magnet type [3]. To overcome this difficulty, small wind turbines have multiple rotor blades to compensate for the low starting torque [11]. The increased number of blades aid in the quick start of the rotors and allows the turbine to operate at much lower cut-in wind speeds. As a result of the added number of blades, rotor solidity, σ is increased. Rotor solidity increases startup torque [26] but at the same time decreases rpm of rotors at moderate to

rated wind speed operation [9]. With high σ the airflow 'sees' the rotors as an obstruction and diverges around it rather than going through the rotor swept area. It is therefore not a good strategy, considering the added cost associated of the extra blades but this is not a problem as the cost is negligible due to the small size of the turbine [17]. Nevertheless, high performance gains from the wind must be accomplished through aerodynamic optimization of the rotor blades. Aerodynamic optimization of the rotor blades is associated with optimization of the chord and twist distribution, number of blades, choice of airfoil shape, and the tip speed ratio, λ [9]. With blade optimization, power coefficients of wind turbines close to the Betz limit of 59.2% can be realized. There is always a trade-off between aerodynamic optimization of the blades and economic costs associated with it thus limiting the full potential of aerodynamic optimization as a result of the high cost of production.

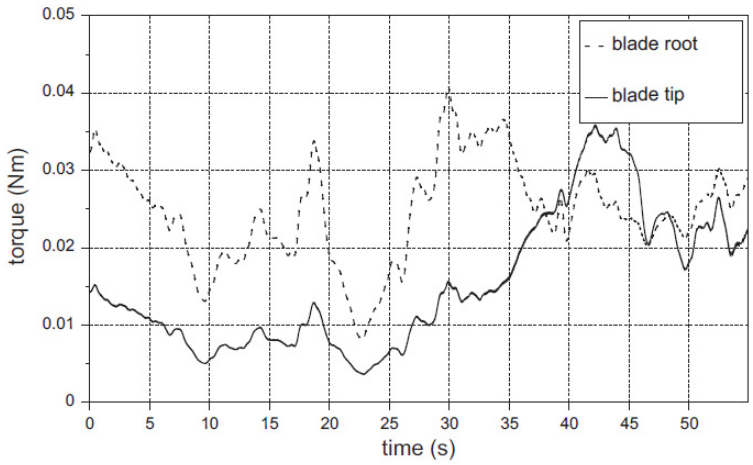

Fig. 2.6 Comparison of torque generated near the root and tip during a low wind speed startup of a 3-bladed 2m wind turbine [25]

Parameters associated with blade geometry optimization are important, because once optimized, shorter rotor blades would produce comparable power compared to larger and less optimized blades. The efficiency of the rotor largely depends on the blade's profile [11,20] in increasing the lift to generate sufficient torque. As discussed earlier, the airfoil is one of the fundamental parts of a rotor blade design. Its purpose is to induce suction on the upper surface of the blade to generate lift. Drag is also generated perpendicular to the lift and its presence is highly undesirable. In order to maximize the power coefficient and the torque generated, the lift coefficient, C_L and the lift to drag ratio, L/D ratio for the airfoil must be maximized [11,27,28].

Higher *L/D* ratios contribute to higher values of torque and it is desirable that at favorable *L/D* ratios, there is maximum C_L in order to have a small sized rotor [13]. Airfoils resistant to laminar flow separation and laminar bubbles will greatly increase performance of small wind turbines without the need for higher rotor solidity or larger diameter blades. Together with aerodynamic optimization, lighter blades with low rotational inertia would yield better performance at lower cut-in wind speeds.

2.10 Aerodynamic forces experienced by a wind turbine blade – Blade element momentum theory (BEM)

2.10.1 Blade element momentum theory (BEM theory)

The Blade Element Momentum theory is based on the Glauert propeller theory [29,30] modified to be applied in the analysis of wind turbines. With the introduction of Prandtl's tip loss factor, BEM theory accurately predicts rotor thrust, torque, power and performance by considering elemental blade sections, *dr* and analyzing each elemental section along the span of the blades. The elemental sections are basically 2-D airfoil sections (figure. 2.7) on which lift and drag forces act. The lift and drag forces contribute to the thrust and tangential forces experienced by the airfoil. The tangential force is responsible for the rotation of the blades through the generation of torque.

Figure 2.7 shows the velocity triangle associated with the airfoil. Axial velocity, V_{axial} and tangential velocity, V_{tan} form the components of relative velocity, V_{rel} which the airfoil 'sees' as an incoming flow making an angle of attack, α with the chordline. The angle between V_{rel} and the plane of rotation is Φ and is easily calculated from the velocity triangle. The angle between the plane of rotation and chordline of the airfoil is β. It changes along the span of the blade for each elemental airfoil section according to the twist distribution.

$$V_{axial} = V_{\infty}(1- a) \quad (2.1)$$

$$V_{tan} = \omega r(1+a') \quad (2.2)$$

Where a and a' are the axial and tangential induction or interference factors respectively and ω is the rotational velocity of the blade given in rad^{-1}.

2.10.2 Calculating the angle of attack, α

The value of α is simply the difference between Φ and β. The pitch angle, β is provided while Φ needs to be calculated from the velocity triangle (figure 2.7). During the calculation of Φ, the induction factors are taken to be zero for simplicity, making $V_{axial} = V_\infty$ and $V_{tan} = \omega r$. Therefore:-

$$\Phi = tan^{-1} \frac{V_\infty}{\omega r} \quad (2.3)$$

and

$$\alpha = tan^{-1} \frac{V_\infty}{\omega r} - \beta \quad (2.4)$$

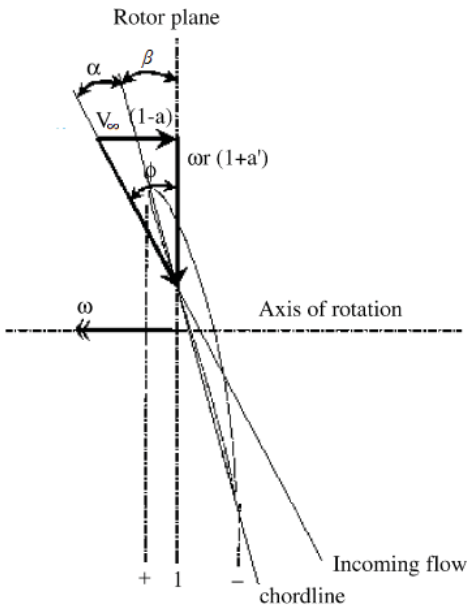

Fig. 2.7 Flow velocity vector associated with an airfoil [29]

The relative velocity is responsible for generating lift and drag forces on the airfoil as seen in figure 2.8. Lift acts perpendicular to the incoming relative velocity and drag acts inline to it. The relative velocity is greater in magnitude to V_{axial} and V_{tan} and increases with increase in rotor radius. When traversing from the blade's root to the tip, V_∞ stays constant while V_{tan} increases, increasing V_{rel}. As the relative velocity is made up of the vector additions of V_∞ and V_{tan} the relative velocity is zero when the tangential velocity is zero even when the axial velocity is of some finite value apart from zero. This condition indicates a non revolving rotor blade. That means that rotation gives rise to the existence of the relative velocity (vector addition of V_{axial} and V_{tan}) that leads to generation of lift and drag forces on each elemental section of the blade, denoted as dL and dD. This show that initially to get a stationary rotor blade to start rotating, the

torque that needs to be generated for start-up comes from the axial velocity alone in the form of thrust force (*dN*). Once the rotor blades start rotating, the axial and tangential velocity components add up to form the relative velocity that gives rise to lift and drag forces.

2.10.3 Tangential and normal force, *dT* and *dN*

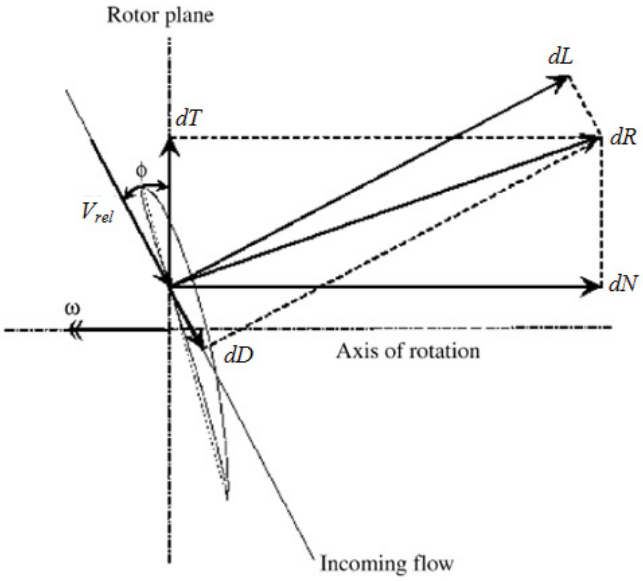

Fig. 2.8 Forces associated with an airfoil [29]

The lift and drag (*dL* and *dD*) are resolved into the resultant force, *dR* that yields the normal force, *dN* and tangential force, *dT* in the axial and tangential direction respectively. Vector addition of *dL* and *dD* in the tangential direction show that the component of drag adds onto the lift component to decrease it. In the axial direction the drag component adds onto the lift component to increase it. Figure 2.9 below shows the resolution of *dL* and *dD* into tangential (vertical) and axial (horizontal) components to yield tangential and normal forces respectively.

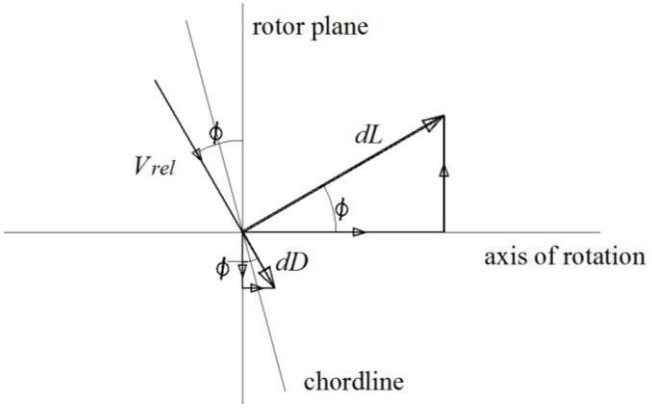

Fig. 2.9 Resolution of lift and drag force into normal and tangential force

The forces, dT and dN are related by the angle Φ that forms between the rotor plane and V_{rel}.

$$dT = dDcos\phi + dLsin\phi \quad (2.5)$$

$$dN = dDsin\phi + dLcos\phi \quad (2.6)$$

2.10.4 Lift and *L/D* ratio

It is desired that the torque on the rotor blades be maximized to generate more power and have faster start-ups in low wind conditions. From equation 2.5 it is clear that the component of drag force adds to decrease the torque, dT and lift force increases it. Therefore high lift, C_L and low drag, C_D is desired in a good airfoil design. In summary, high C_L and low C_D produces high L/D ratio where high C_L and L/D ratio are important factors in designing high lift, low speed airfoils. As a result of optimizing an airfoil to produce greater C_L and L/D ratio to increase torque, the thrust force, dN also increases (eqn 2.6). Both drag and lift contribute towards the increase. This increase in C_L and L/D ratio to improve rotor performance aerodynamically makes the structure of the rotor to suffer as a result of the increase in thrust force. As wind turbine rotors become larger, the issue of economics and cost become important and the margin between aerodynamic optimization and cost of rotor structure become ever closer. As a result, aerodynamic optimization of the rotor has to give way to a more structurally sound design. For this reason one does not opt for a very high value of C_L during airfoil optimization. For micro and small scale wind turbine rotors, structural integrity is not a problem as small rotors can be manufactured with higher factor of safety as compared to large scale wind turbine rotors. Nevertheless, high torque generation without the cost of increased thrust can be achieved by giving more priority to increase L/D ratio rather than C_L. This means reducing C_D. Drag is present on the airfoil surface in the form of *skin friction* and *form* or *pressure* drag. During stall, when flow separates, form drag increases immensely, and thus to reduce drag, the chance of separation has to be avoided [31].

2.10.5 Calculation of normal force (thrust) and torque on the rotor blade

From BEM theory, the normal force, dN and torque, dM can be evaluated from each elemental airfoil section across the span of each blade and integrated from r = 0-R, i.e. from root to tip to yield the rotor's normal force and torque. The elemental normal force and torque are given below

$$dN = \frac{\rho V_\infty^2 (1-a)^2}{2sin^2\emptyset} N_b (C_L cos\emptyset + C_D sin\emptyset)cdr_1 \quad (2.7)$$

$$dM = \frac{\rho V_\infty (1-a)}{2sin\emptyset} \frac{\omega r_1 (1+a')}{cos\phi} N_b (C_L sin\emptyset - C_D cos\emptyset)cr_1 dr_1 \quad (2.8)$$

Where

r_1 is the incremental distance from the centre of the rotor blade to the radial location of one of the airfoil sections.

N_b denotes the number of blades present.

C_L and C_D are obtained from experiments. C_L and C_D are dependent on the Reynolds number and angle of attack. The Reynolds number is dependent on the local chord and local relative velocity present at the particular airfoil location. The local chord is governed by the chord distribution for the rotor blade and relative velocity on the freestream and tangential velocity.

c is the local chord at the particular airfoil location. It is dependent on the chord distribution of the rotor blade.

2.11 Wind turbine rotor aerodynamics – generation of torque by the rotor blades

The rotor blades are responsible for the capture of kinetic energy from the blowing wind and have it converted to mechanical form. In doing so, all it does is to rotate and turn the kinetic energy of the air flow to rotational mechanical energy. To the observer the operation may look simple but it is in fact a very complicated interaction of fluid (air) with the rotor blades that is to this day not been fully understood. The aerodynamics associated with rotor blade design is complex and designing the blade geometry to exact or to an approximation is governed by the BEM and strip theory [2] for achieving an aerodynamically optimum shape. This would later be degraded to some extent due to economic, strength, material and manufacturing constraints.

2.11.1 Number of rotor blades

In theory as the number of rotor blades increase, the peak power coefficient also increases. Figure 2.10 shows the effects of increasing blade number and the effect it has on power coefficient, C_P. With increasing blade number, the peak C_P is seen to increase dramatically from 1 – 2 blades and then slowly as blade number increases beyond the 2-bladed configuration mark.

With increase in blade number, the solidity increases and tip speed ratio decreases. Comparing 3 and 2-bladed rotors, the 3-bladed rotors produce more torque and can be loaded up more to take advantage of its torque producing capability, eliminating the need for high rpm as in the case of a 2-bladed rotor design. It is known that rotor power = $T\omega$. For 2-bladed rotor, torque is low and it compensates this with higher rotational speed, ω to achieve the same level of power coefficient, C_P as a 3-bladed rotor. The opposite is for a 3-bladed rotor. This gives rise to the difference in tip speed ratios, λ for the 2 and 3-bladed rotors as ω is one of the variables in the calculation of λ. It seems impractical to keep on increasing the number of blades on a rotor for the gain of 1- 3% increase in performance. The 2 and 3-bladed rotor configurations have been preferred as standard as they fulfill both the aerodynamic, economic and structural requirements of the wind turbine well. Contrary to theory, C_P was found to decrease for the American type multi-bladed wind turbines [2]. With increase in the rotor solidity with increasing blades, cascade flow begins to occur making the aerodynamic flow conditions quite complex. This cascade flow phenomenon cannot be explained through theoretical means.

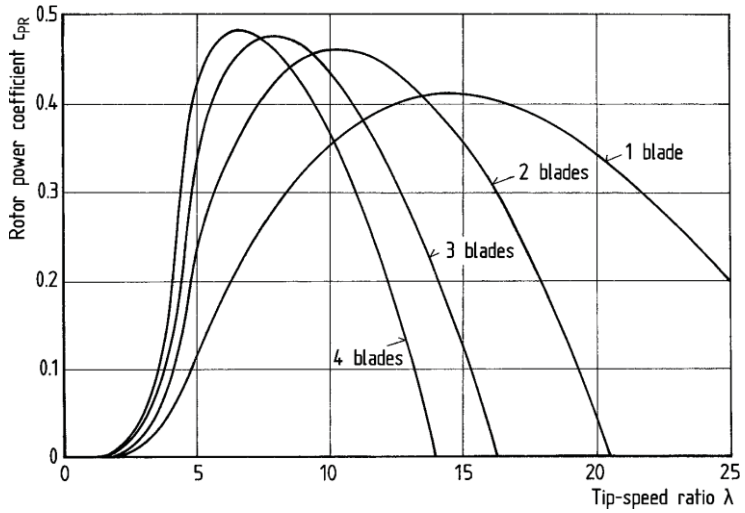

Fig. 2.10 Variation of rotor power coefficient with respect to number of rotor blades [2]

2.11.2 Taper, twist and pitch angle

2.11.2.1 Chord distribution

Apart from aerodynamic optimization associated with the blade airfoil section to improve on the performance of the rotor, twist, taper are as important and go hand in hand to airfoil selection.

The twist and taper demand that the radius, tip speed ratio and lift characteristics at each radial station be known before BEM theory is applied to yield the respective distributions. The taper or chord distribution governs the rotor solidity along the radial distance. As the chord distribution is changed such that the overall solidity is kept constant, sectional rotor solidity can be controlled along the radial distance and increased or decreased as required for maximum power production for a specific wind speed range. Chord distribution and tip speed ratio go hand in hand as the deciding factors in controlling the Reynolds number across airfoil sections along the radial distance of the blade. Figure 2.11 shows an evaluation of chord distribution for different tip speed ratios and different number of blades based on BEM theory. The chosen airfoil is a NACA 4415 airfoil with a chosen design C_L of 1.1. With increasing λ and blade number, the rotor solidity decreases making the blade very slender and structurally weak. It is noticed that the blade geometry is thicker near the root and becomes thinner towards the tip. Since the blade sections near the root do not contribute much towards power production, they are made as thick as possible since most of the stress is concentrated at the root during rotor operation. The outer sections are responsible for producing most of the power and thus the chord distribution within the outer region must remain identical to the theoretical optimum shape.

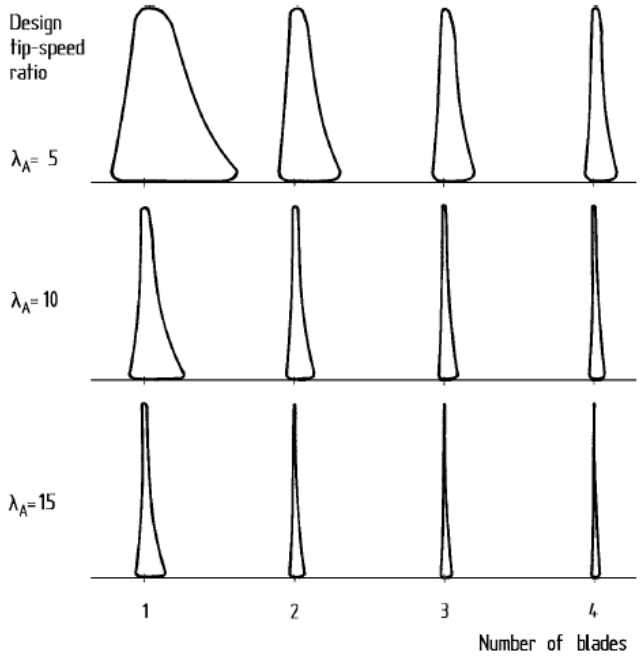

Fig. 2.11 Variation of blade geometry based on the number of blades and tip speed ratio for blade with NACA 4415 airfoil section and design C_L=1.1calculated through BEM theory [2]

2.11.2.2 Twist distribution

The relative velocity, V_{rel} changes both in magnitude and direction along the span of the rotor of a rotating blade. The V_{rel} increases in magnitude from the root towards the tip since the tangential velocity, V_{tan} increases along each radial station towards the tip. During the increase in V_{rel}, the effective angle, α formed between its direction and the chord line at each radial station decreases from the root towards the tip. This decrease in α degrades the lift being generated by each of the airfoil sections along the blade span. Therefore in order to keep α constant, a twist distribution has been introduced to the whole of the blade span. The twist distribution allows for each airfoil section across the span of the rotating blades to be within an optimal α range with respect to V_{rel} and thus improve the blade's performance by keeping L/D ratio at a maximum [32]. The optimum twist distribution can only be done for one tip speed ratio, λ which is usually chosen around the turbine's rated power operating point [2]. This means that at other tip speed ratios, the twist would not be optimum and a loss in turbine rotor performance would be noticed, either if λ is decreasing or increasing from the rated λ. Twist distribution in the inner blade region, i.e. near the root does not follow the twist distribution as closely to the optimum twist distribution for ease of manufacture since the flow field velocities are not great near the root. Figure 2.12 shows how twist distribution influences power coefficient. Twists A and B show aerodynamically optimum and simplified linear twists respectively while C shows zero twist. In the graph of performance vs. tip speed ratio, twist A dominates followed by B and C.

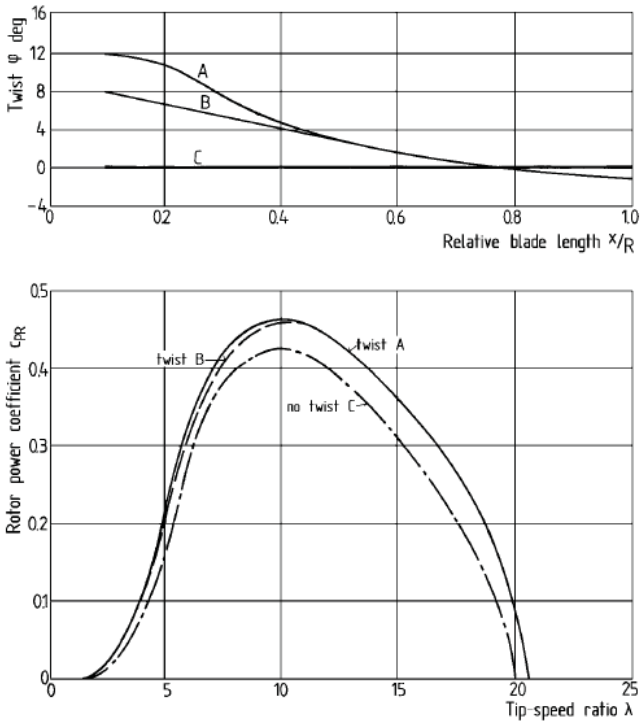

Fig. 2.12 Influence of twist distribution on the performance of a rotor blade [2]

2.11.2.3 Pitch angle

The pitch angle, β for a wind turbine rotor blade is measured from the rotor plane to the chordline of the airfoil section and unlike Φ or α which are aerodynamic parameters, β is a design parameter and can be set to any value depending on the rotor design and wind condition. The setting of the blade pitch angle for the rotor involves β being measured from the rotation plane to chordline of airfoil section at the root, (x/C = 0). For a rotor with variable pitch, the angle is varied with respect to the variation in wind speed to extract as much of the energy in the wind or in the case of high wind speeds, slow down the rotors. For low wind speed condition, β is kept very low to promote quick start up sequence. In this condition the angle, α formed between the airfoil chordline and freestream velocity is very large and undesirable for lift generation. As the wind speed increases, β begins to increase to maintain optimum Φ between the relative velocity and chordline of airfoil for optimum aerodynamic performance. The figure 2.13 below shows that β increases with freestream velocity to maintain peak torque and thus peak performance. Using the least square fit with a third order polynomial, Thumthae and Chitsomboon [33] found the blade pitch angles for producing the maximum mechanical power to be 4.12°, 5. 28°, 6.66° and 8.76° at wind speeds of 7.2, 8.0, 9.0 and 10.5 m/s respectively.

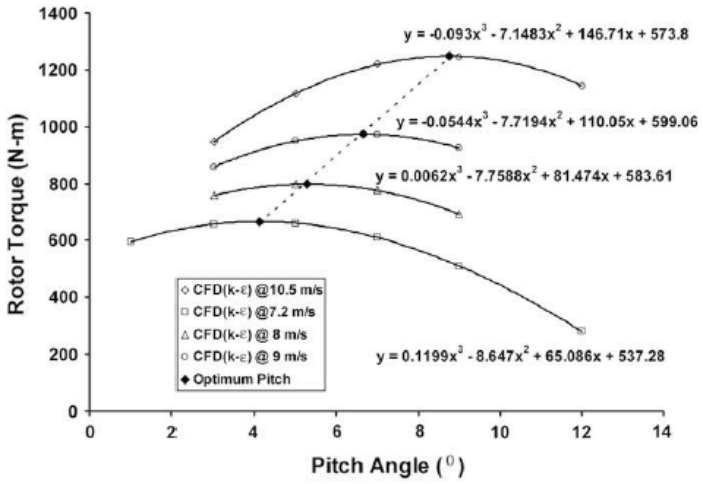

Fig. 2.13 Computed rotor torque at different freestream velocities and pitch angle [33]

Figure 2.14 shows the relationship between powers generated by the rotor at 5 different pitch settings for increasing wind speed. The shaded box in the graph indicates the turbines operating wind speed and power range. At the low pitch settings of 5° and 10°, the rotor peaks to the rated power at around 10m/s wind speed. As β increases to 20°, 30° and 40°, the rotor achieves the rated power within a very high wind speed range due to the rotor not performing within its optimum α value. On the other hand the graph shows that outside the operating range of the WKA-60 rotor, a higher pitch setting achieves more power at very high wind speed range compared to the lower pitch settings. With increase in freestream velocity, α increases considerably, so much that the blade gets stalled at the lower pitch settings resulting in flow separation. At the higher pitch settings of 20°, 30° and 40°, α is kept below the stalling angle and so the blades are able to produce considerable power with increasing wind speed.

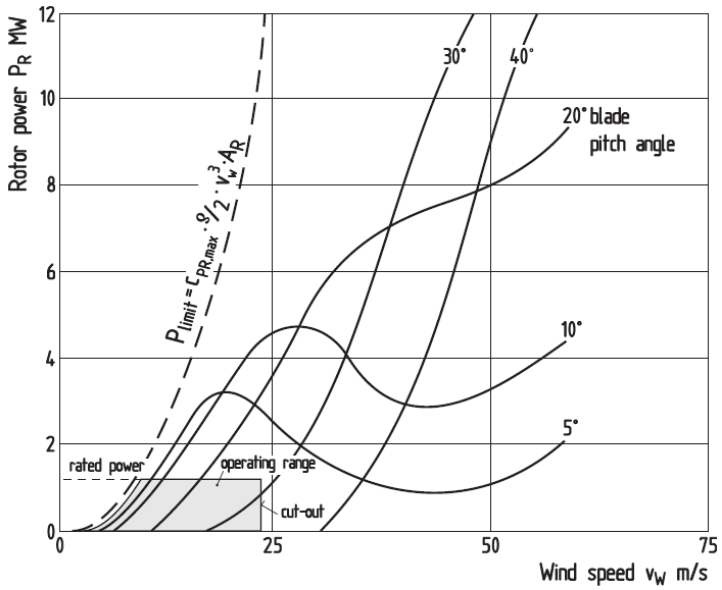

Fig. 2.14 Power input of the WKA-60 rotor to generator at different fixed pitch settings and fixed rotor rpm [2]

2.12 Power control through aerodynamic means

As the wind is never steady, a wind turbine needs to have some form of power regulation so that there is no structural and generator damage when the wind speed goes past the rated wind speed or past the cut-off wind speed of the turbine. Different forms of power control mechanisms have been employed depending on the situation, turbine type and size of turbines.

2.12.2 Pitch control

Pitch control is one such means of slowing down the rotor during heavy wind speeds to alleviate the stresses on the rotor and structure and regulate electrical power of the generator. Pitch control is of 2 forms – passive and active. Passive pitch control is usually mechanically controlled by means of masses and spring systems that require no feedback system and require no source of external power. For active pitch control, there is a continual feedback so as to monitor the pitch angle of each blade and change them accordingly through electrical means. For large scale wind turbines, active form of pitch control is most common where electric motors change the pitch. Passive pitch control is mostly associated with small wind turbines and for micro wind turbines, there is no form of pitch control [2] with stall regulation and electronic braking being the most common forms of power regulation.

Pitch control basically slows down the rotors through pitching of the blades. There are 2 ways in which the rotor can be slowed through pitching, either by increasing (feathering) or decreasing (stalling) the rotor pitch. Figure 2.15 shows the 2 scenarios where the first schematic shows the normal position of airfoil section of blade. The second schematic shows an increase in the pitch angle in the positive direction. As the pitch angle increases, α decreases leading to a reduction in C_L that slows down the rotor. For a complete stop of the blades, the pitch angle may be increased to 90° as shown (feathered position). In the third schematic, pitch is increased in the negative direction, doing so increases α and if $\alpha > \alpha_{crit}$ (stall angle), the flow separates from the airfoil surface inducing a dramatic loss in lift and an increase in form drag that ultimately slows the rotor. Pitching the blades towards feather has the advantage of decreasing wind loading on the rotor by decreasing the exposed area of rotor as it is pitched out of the strong winds. In the case of pitching towards stall, the area exposed to the wind increases, increasing the stress on the rotor (figure 2.16, left). While feathering seem to be the logical form of power control, the response time for pitching towards feather is greater compared to pitching towards stall as a greater angle has to be covered to achieve feather. Despite this, feathering achieves consistent control of power from the rotor at all wind speeds compared to stall control as shown in figure 2.16 for the Nibe wind turbine with 2 variants of rotor blades – A and B for stall control and pitch (feather) control respectably.

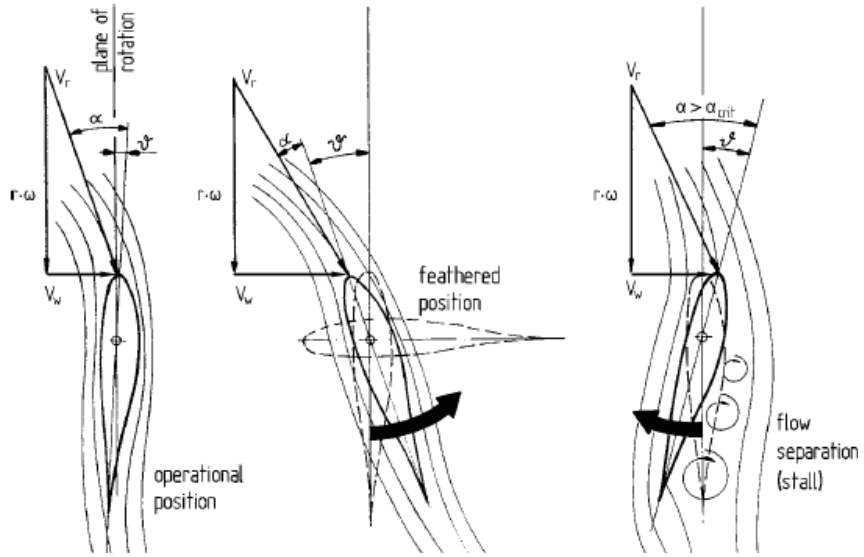

Fig 2.15 Controlling the rotor power through pitching towards feather or stall [2]

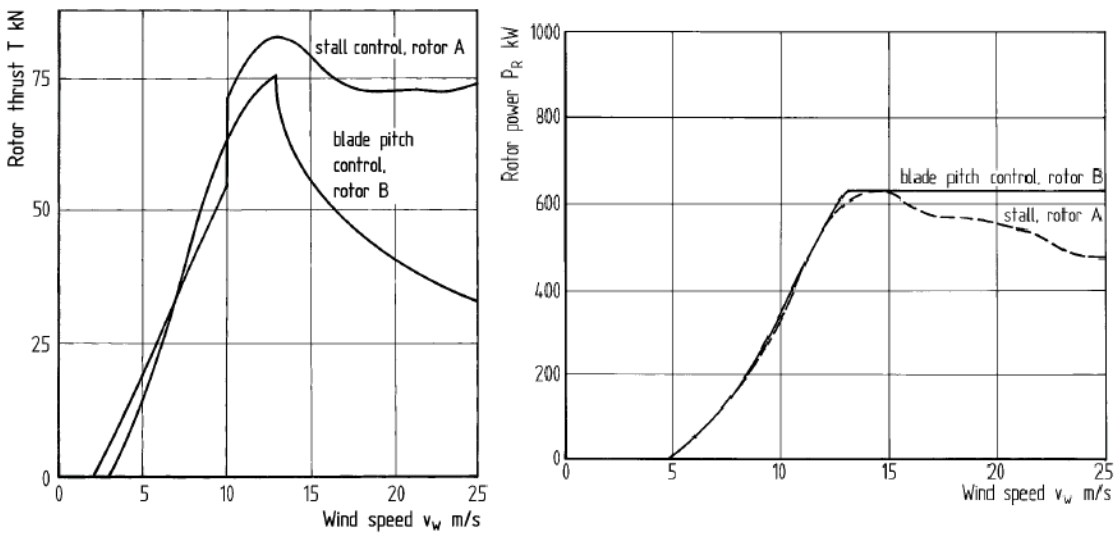

Fig 2.16 Pitch (feather) and stall control of the Nibe wind turbine. On the left, variation of thrust on the rotor vs. wind speed. On the right, power regulation by pitch and stall control past the cut-off wind speed [2]

2.12.3 Fixed pitch passive stall control

Another method of controlling the rotor speed is through fixed pitch stall control where the occurrence of stalling is dependent on design feature of the blade geometry and the airfoil section. The fixed pitch form of stall control requires no mechanical form of pitching, thus simplifying the design of stall control. This type of stall control is most common in small wind turbines where due to their size, any form of pitch control would deem the turbine too expensive. For the fixed pitch stall to occur careful design of the blade and selection of rotor speed must be done and the rotors must operate at rated power at speeds below the aerodynamically optimum rotor speed so as to not stall during normal operation. Stalling is achieved passively at the critical wind speed where the rotor has reached its maximum rpm due to geometric constraints and as a result only the freestream component of the velocity triangle increases, increasing the angle between V_{rel} and rotor plane, α (figure 2.17). Just as in the case of pitching towards stall, when $\alpha > \alpha_{crit}$ flow separation occurs reducing both lift and L/D ratio and slowing the rotor down. As a rule, the aerodynamic performance of wind turbines with this type of power control decreases above a wind speed of 15m/s [2]. As part of their aerodynamic design to induce flow separation by means of stalling, the rotor blades have a nonlinear twist distribution where the inboard region is highly twisted and the outer region remains flat with no twist. This type of twist distribution not only helps the blade's stall characteristics but also improves its starting behavior. Fixed type,

stall regulated rotor blades must be designed strongly to resist the thrust force from the high winds during power regulation. For this reason fixed pitch stall is common with small wind turbine rotors whose blades can be made strong without much economic implications and since the rotors operate at high rpm, centrifugal forces help to keep the blades stiff.

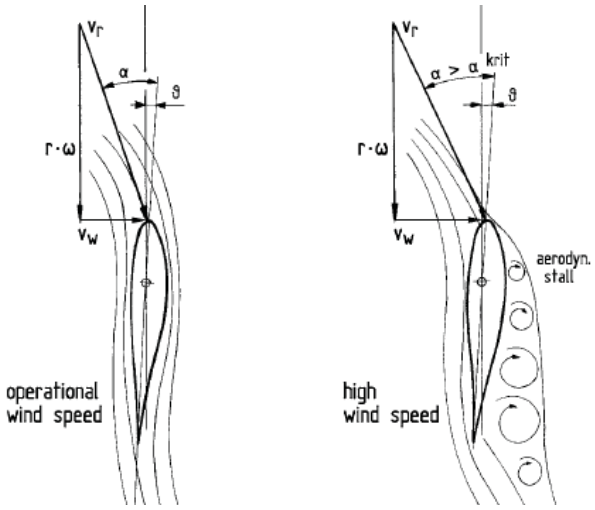

Fig. 2.17 Fixed pitch stall control with fixed rotor speed and increasing wind speed [2]

2.13 Aerodynamics of rotating and non-rotating rotor blades

Rotor design, calculation of thrust, normal force, torque and power for current horizontal axis wind turbines have been accomplished through the use of 2-D airfoil data combined with BEM theory. The Blade Element and Momentum theory does not take finite number of blades and 3-D effects of a rotating rotor such as dynamic stall, and circulation into account and only models approximations of them using a combination of 2-D data [34]. At present, BEM theory is the only analytical tool used to model and evaluate the aerodynamic parameters of a rotating blade. Although most of the aerodynamic flow phenomena are known, they are a challenge to predict and understand in detail and remains a critical research area [35,36]. Research into rotating and non-rotating blades has been carried out for more than a century but poorly understood. Himmelskamp [37] found that lift and stall delay both increased due to rotational effects. Banks and Gadd [38] concluded that stall delay occurred due to the stabilization of boundary layer during the cause of separation due to rotation. Tangler [39] found C_L values to be higher for a rotating airfoil compared to non-rotating airfoil towards the inboard section of the blade. He attributed this to stall delay due to 3-D effects caused by rotation. Kamada, Kawabuchi and others [34] have investigated the pressure distributions of 2-D airfoil wind tunnel data with rotating and stationary blade airfoil sections at 0.7R location. Good correlation was found

between the 2-D airfoil data and stationary blade within the pre-stall region. Compared with the rotating blade, wind tunnel data matched well in the pre-stall angle range just before the occurrence of stall at 16°. Beyond the post-stall angle the airfoil section at 0.7*R* showed an increase in normal force coefficient, C_n (normal to airfoil chordline) compared to the wind tunnel airfoil section of a stationary blade (figure 2.18). The pressure distribution also showed an increase in upper surface suction past stall from x/C = 0.05 – 0.7. Kamada explains that the increase is due to rotational effects and partly due to higher Reynolds number experienced at the *0.7R* section location of the rotating blade

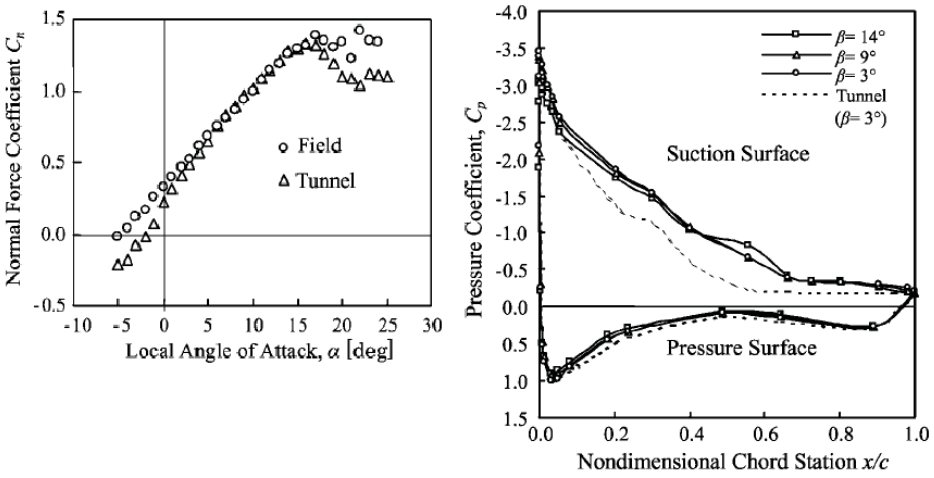

Fig. 2.18 Comparing normal force coefficient and pressure distribution of airfoil section of a stationary blade in wind tunnel to airfoil section on a rotating blade [34]

Sicot [35] investigated the effects of rotation and turbulence on the stall characteristic of an airfoil section located at the inboard section, middle and outboard of the blade at 0.26*R,* 0.51*R* and 0.75*R* respectively at different turbulence intensities. There was good correlation between the rotating and non rotating blade section pressure distribution for all locations except for 0.26*R* location as shown in figure 2.19 below. Pressure distribution is shown for post stall α values of 16°, 20° and 30°. The separation is clearly marked as S_t and S_r for stationary and rotating blades respectively. In all the cases, the airfoil section on the rotating blades show increased pressure on both the lower and upper surfaces. Flow separation for α =16° and 20° occurs further down towards the trailing edge compared to the stationary airfoil. The increase in suction on the upper surface for the rotating blade is an indication of lift augmentation.

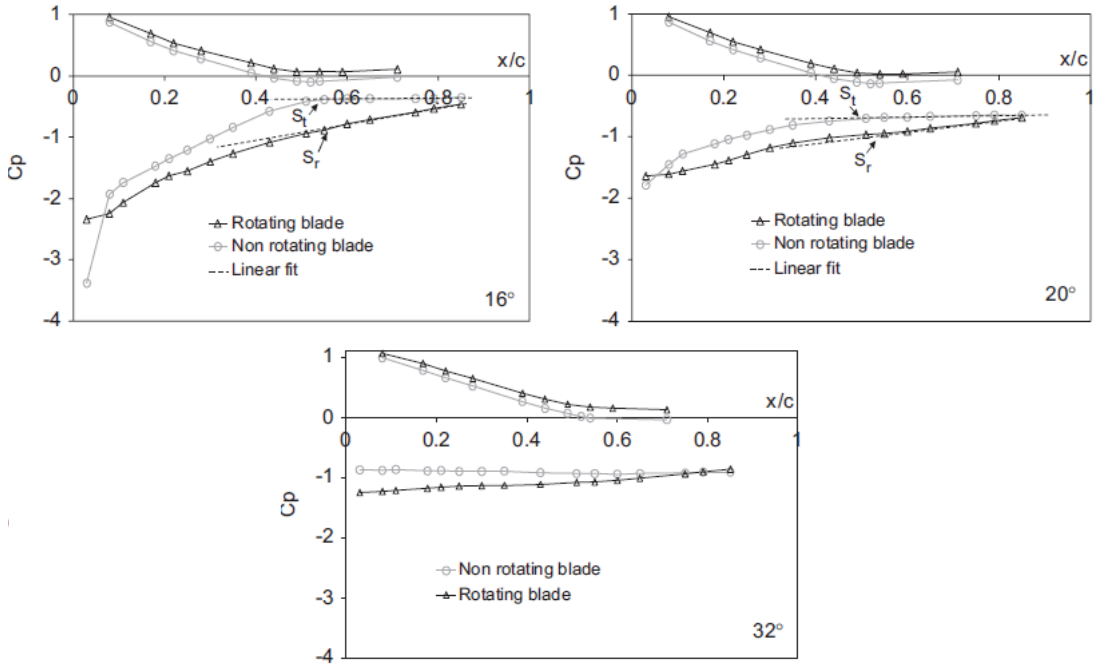

Fig. 2.19 Comparison of pressure distribution of rotating and stationary blades at stall and post-stall configurations at 0.27*R* location [35]

Similar results were presented by Ronsten [40] where a 2.375m rotating and stationary blades were compared. Airfoil stations on the rotating blade were chosen at 8 locations starting from 0.3*R* and going towards the tip and tested at λ = 4.32 and 7.37. The pressure distributions showed that from the middle of the rotor to the inboard section, there was noticeable difference in pressure between the rotating and non rotating blades for λ = 4.32 only (figure 2.20). At 0.3*R* there was a drastic increase in peak suction that extended all the way to the trailing edge. This increase in suction was also present at 0.55*R* but less pronounced. For both locations there was an increase in lower surface pressure as well when compared to the stationary blade airfoil locations. Figure 2.21 shows the variation of lift coefficients for airfoil sections at 0.3*R* and 0.55*R* locations for the rotating and stationary blades at λ = 4.32. Close correlation was maintained between the rotating and stationary sections just before stalling for both locations. In the post-stall region, lift decreased for the non rotating blade whereas for the rotating, it increased for both locations but increased dramatically at the 0.3*R* location. Ronsten concluded that at low values of tip speed ratios, the inner section of the rotor experiences more loading than is predicated by 2-D airfoil data and that during high angle of operation a triangular shaped pressure distribution is common close to the root.

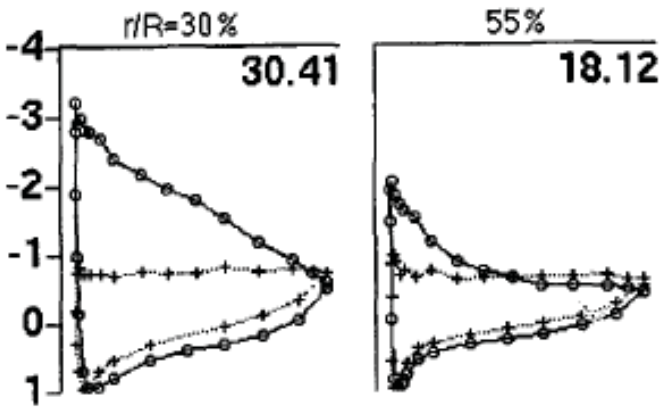

Fig. 2.20 Comparison of pressure distribution of rotating and stationary blades at locations of 0.3R and 0.55R at α = 30.41° and 18.12° respectively at λ = 4.32 [40]

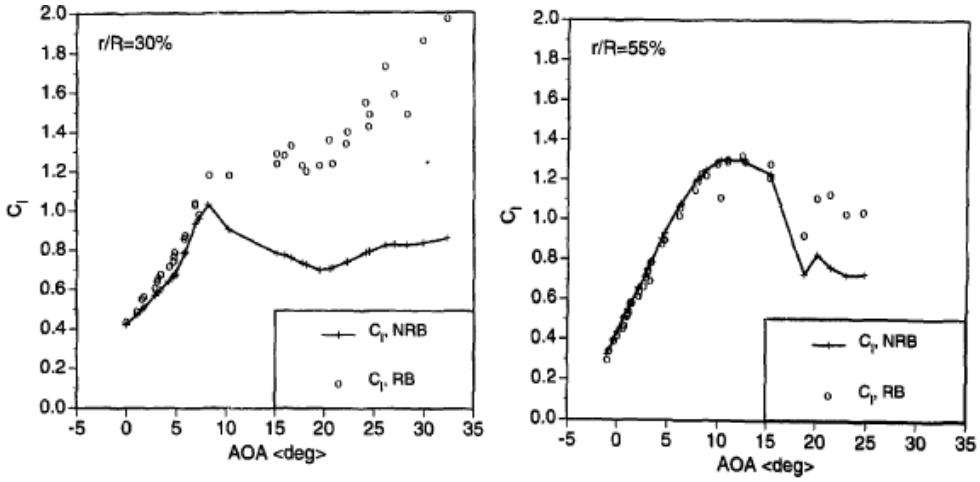

Fig. 2.21 Variation of lift coefficients of rotating and stationary blades at locations of 0.3R and 0.55R at λ = 7.37 [40]

Likewise Schreck and Robinson [36] also compared rotating and stationary blades by comparing the normal force coefficient, C_n. They shed some light on rotational argumentation and dynamic stall caused by yaw. As discussed by the previous authors, a substantial increase in C_n occurs near the inbound section of the rotor blade due to rotor argumentation compared to the outer sections of the rotor as shown in figure 2.22 on the right, at 0.34R location. Pitch angle for the rotating blade was fixed at 3° and freestream velocity, U_∞ increased from 5 – 25m/s at 1 m/s increments. Corresponding C_n values were thus plotted against local inflow angle, LFA (α). The LFA was calculated by considering the velocity triangle at 0.34R location with increasing U_∞ and constant rotor rpm of 71.6. Therefore with increasing U_∞, LFA increased as shown in figure 2.22 on the left. The stationary blade was compared to the rotating blade by relating U_∞ (20 and

30m/s) to V_{rel} (13.8 – 28.1m/s) of the rotating blade at 0.34R location to match Re for the last 11 points highlighted in black (figure 2.22, right). As for the LFA, the stationary blade was pitched from 90° to 35° in 5° increments to match it. The 90° to 35° in pitch angle for the stationary blade corresponds to 0° to 55° with U_∞. Basically Schreck matched the conditions that an airfoil section 'sees' on a rotating blade with that of a stationary airfoil by substituting V_{rel} on the rotating blade with U_∞ on the stationary blade.

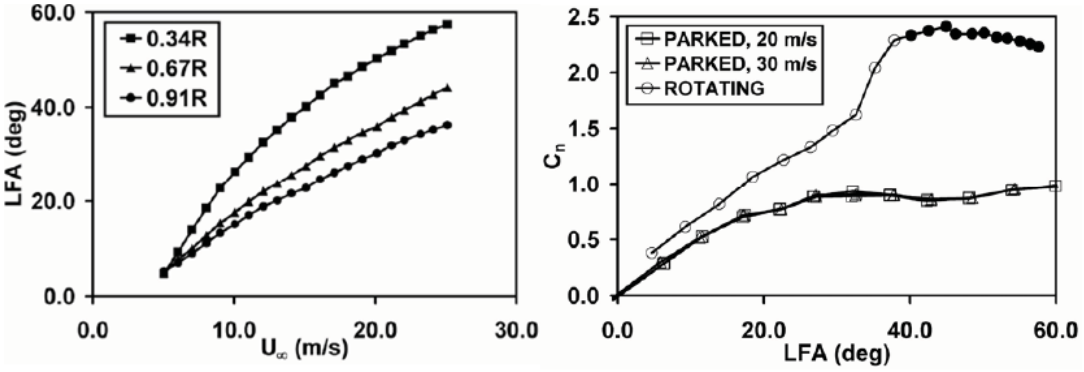

Fig. 2.22 Variation of local flow angle, LFA with freestream velocity for rotting blade (left). Normal force distribution, C_n with LEA for rotating and stationary blade at 0.3R location (right) [36]

2.14 The effect of freestream velocity on the rotation of the rotor blades

In order for lift to be generated across the upper surface of an airfoil section of a rotor blade, there must exist the presence of relative velocity, V_{rel}. The relative velocity is generated only in the vicinity of freestream velocity, V_∞ and tangential velocity, V_{tan} and cannot exist without either one. Rotor blades have very low pitch angles in the range of 5° – 20° at most and during operation, V_{tan} at the tip far exceeds V_∞ resulting in tip speed ratios of the order of 1 – 10. This shows that the fast rotating rotor produces a high magnitude of V_{rel} across most of the outer portion of the blade compared to V_∞ and thus generates high lift values. If one considers the variation of V_∞ across the span of a rotor from root to tip, its magnitude would be increasing and α that the each airfoil 'sees' would be decreasing, therefore the need for twist. As a result the outer portion of the rotor blades produces the majority of the power due to the high values of V_{rel}.

The generation of lift and drag and their resolution into resultant, normal, thrust and tangential forces have been presented in section 2.10.3 and based on V_{rel} alone. The question is how is torque (resolution of lift and drag forces in the tangential direction) generated for a stationary

rotor blade with just V_∞ present when V_{rel} is the basis for torque generation according to BEM theory. A stationary rotor presents a very high angle of attack with respect to V_∞. The high angle of attack falls within region 3 as shown in figure 2.23 where the airfoil is operating close to 90° in stall mode with C_L values close to zero with maximum C_D values.

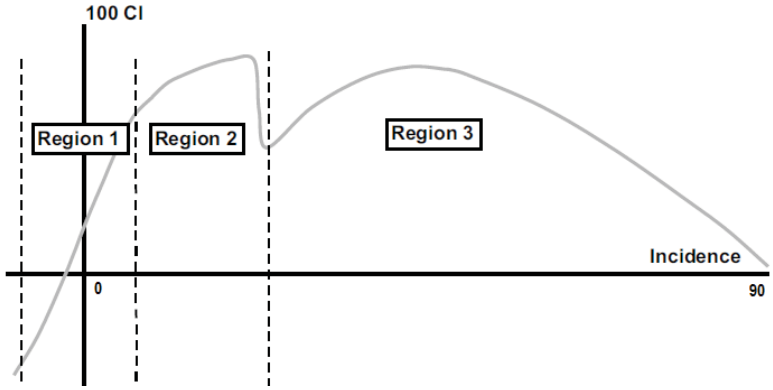

Fig. 2.23 General characteristics of C_L variation with respect to α for airfoils [41]

Therefore the starting torque on the stationary blades can be attributed to reaction effects by the freestream velocity acting on the lower surface of the blade. The free flowing mass of air 'sees' the rotor as an obstruction and instantly pushes against the rotors generating thrust on the rotor planeform area. The geometry and pitch angle setting are such that the flow is diverted laterally down and then backwards to presume its normal flow pattern. The lateral motion of the flow demands that the blades move opposite to the direction of the motion of flow, rotating the blades. The flow phenomenon follows Newtonian principle of aerodynamics lift and propulsion where the upward motion is a result of accelerating air mass downwards [42].

As the rotors start rotating due to reaction forces attributed to V_∞, V_{rel} is generated increasing the overall torque of the rotor. The V_{rel} eliminates all aspects of drag in the direction of the rotor plane of rotation when C_L and C_D are resolved in this plane to evaluate torque. As a result the rotating blade has no resistance within the plane of rotation since $C_L >> C_D$ thereby achieving high rotational speeds.

Chapter 3 Design improvement and selection of a high lift and low Reynolds number airfoil for small horizontal axis wind turbine application

3.1 Airfoil selection

Existing airfoil designs were chosen for analysis using xfoil code for small scale wind turbine application, suitable for power production at low wind velocities. Airfoils already tailored for small and micro wind turbines and with high lift, low Reynolds number characteristics were chosen. The choice of airfoil selections were made from university of Illinois website [43] an online database containing a number of different airfoils for different applications including low *Re* airfoils.

3.2 Xfoil code

Xfoil 6.94 code was used to carry out 2-D analysis and design of the chosen airfoils. Xfoil program code was written by Mark Drela in 1986 for analyzing subsonic airfoils [44] and since then it has been revised, improved and made more user-interactive for easy use. Xfoil relies on high-order panel methods and fully coupled viscous/inviscid interaction methods to carry out analysis on airfoils. Xfoil solves invisicd solutions using a linear-vorticity stream function panel method. Viscous solution (inclusion of boundary layer and wake) incorporates total velocity at each panel node on airfoil and wake influenced by the freestream velocity, surface vorticity and equivalent viscous source distribution. These, obtained from panel solution with the Karman-Tsien compressibility correction added, form viscous equations that are solved by a full Newton method [44]. Xfoil fails to accurately analyze airfoils at transonic and above velocities due the fact that the wake trajectory changes and lift decreases as viscous effects increase with speed. Some of the tasks performed by xfoil include [45]:

1. Viscous (or incviscid) analysis of an existing airfoil, allowing
   - Forced or free transition
   - Limited trailing edge separation
   - Accurate lift and drag predictions just before stalling
   - Karman-Tsien compressibility correction

2. Airfoil geometric design and redesign by the use of a mouse which include:

- Full-inverse, based on complex mapping formulation
- Mixed inverse, allowing relatively

3. Airfoil geometric redesign by use of geometric parameters that include
   - New max thickness or camber
   - New leading edge by altering LE radius
   - New trailing edge (Tgap)

Pressure distribution, coefficients of lift and drag, lift to drag ratio, skin friction drag, form drag and laminar to turbulent transition points are some of the possible data obtainable during the 2-D airfoil analysis. Together with the analysis, airfoil geometry alterations are also possible. Camber thickness, leading edge radius, trailing edge thickness, camber line location position, and new airfoil shape via loading of coordinate file can be achieved.

3.3 Selection of Reynolds numbers

The Reynolds numbers, under which analysis of airfoils were done in xfoil, were based on the relative velocity, V_{rel}. Reynolds number based on relative velocity was chosen to capture lift and drag on the airfoil section of a rotating blade. The relative velocity was calculated from the velocity triangle that is made from the vector components of tangential and freestream velocities. Freestream velocity was chosen based on the wind conditions common in Fiji in the range of 3 – 8m/s where average wind speed is around 5m/s [1]. The tangential velocity was calculated for a small wind turbine with rotor diameter of 1.5m with tip speed ratio, λ of 5.5 at which, for a 2-bladed system power coefficient, C_P is maximized [46,47]. Mid section location was chosen ($r = R/2$) for the calculation of relative velocity as the outer portion of the rotor blades produce the most power in relation to the inner section [2,27,48]. The results are presented in table 3.1.

Table 3.1 Relative velocities and corresponding Reynolds numbers calculated for airfoil section at $r = R/2$

V_∞ (m/s)	V_{tan} (m/s)	V_{rel} (m/s)	Reynolds no.
3	8.25	8.78	55234
4	11	11.70	73645
5	13.75	14.63	92056
6	16.5	17.56	110467
7	19.25	20.48	128878
8	22	23.41	147289

3.4 Choice of airfoils

As explained before, the airfoils chosen were based on their application and aerodynamic characteristics. Airfoils associated with micro and small scale wind turbines, gliders and radio control planes were chosen for analysis. These applications deal with low Reynolds number flow regimes. Apart from the applications, airfoils with stated high lift and low Reynolds number characteristics were chosen. Some of the airfoils and series of airfoils are provided below in table 3.2.

Table 3.2 Airfoil selection based on application and aerodynamic characteristics

Airfoil Type	Application	Aerodynamic characteristics
ah93w series	Wind turbines	
Aquilqsm	Sailplane	
David Fraser-DF series		Low Re
Eppler-E series	Sail planes	High lift, low Re
Goltingen-goe series	airplanes	
Martin Hepperle-mh series	Hang glider	
Selig-s, sd, sg series	Sail planes, wind turbines, RC airplanes etc	High lift, low Re
Wortmann-FX series	Wind turbines	

3.5 Parameters set in xfoil for airfoil analysis

Xfoil accepts airfoil geometries in the form of x and y coordinates from a txt file. The txt file is first loaded into xfoil, panel nodes are increased and set to 240 nodes for accurate results. Viscous parameter is selected to take boundary layer and effects of drag into account. The Reynolds number is entered. Next, the viscous parameter is set which includes the setting of turbulence intensity by entering the n critical number. Lastly angle of attack is entered and the xfoil program executed. Manual iterations would need to be done if the solution fails to converge. As the computations are being done at low Reynolds number chances of the convergence failure are common.

Test parameters considered during analysis of airfoils in xfoil are given below

- Rotor diameter = 1.5m
- Number of blades = 2
- Tip speed ratio, $\lambda = 5.5$ for high speed 2-bladed rotors.

- 2-D analysis carried out at mid section of rotor blade = $R/2$ = 0.375m.
- Freestream velocity range, V_∞ = 3 – 8m/s.
- Test flow stream velocity = relative velocity, V_{rel} at mid section of rotating rotor at V_∞ = 3 – 8m/s.
- Test Reynolds numbers corresponding to V_{rel} = 55,000 to 147,000 with an assumed average chord length at mid section of blade = 100mm.
- Angle of attack range = 0 - 20° in 2° increments with 1° increment from 10 - 16° to capture stall more accurately.
- Turbulence intensity set in xfoil = 0.1% (n_{crt} = 8).

3.6 Results and Discussion

Of the many airfoils tested, 10 best airfoils were chosen based on variations of lift coefficient and *L/D* ratio. These airfoils are designated as A1 – A10. The results of these are presented in the form of variations of lift and drag polar graphs within the approximate Reynolds number range of 55,000 – 150,000 in figures 1.1 – 1.30 which can be found in appendix 1.

3.6.1 Stalling angles of attack, α_{stall} and corresponding maximum lift coefficients, C_{Lmax}

Maximum lift coefficients at the angle of stall are presented in table 3.3 for A1 to A10 airfoils. The results are presented for the minimum and maximum Reynolds number = 55000 and 150000. Many of the airfoils showed signs of soft stall at minimum as well as maximum Reynolds numbers. These are A1, A3, A6, A7, A9 and A10. Airfoils A2, A5 and A6 did not do well at *Re* = 55000 as quite low C_{Lmax} values were recorded as compared to at *Re* = 150000. A3 and A4 airfoils performed the best out of the rest with A9 airfoil close behind. C_{Lmax} values of 1.83 and 1.92 at minimum and maximum *Re* were recorded for A3 airfoil with exceptionally high stalling angles of 14° and 16° respectively. The A4 airfoil has C_{Lmax} values of 1.66 and 2.21 at stalling angles of 6° and 13° respectively. A9 airfoil, although did not have quite as high C_{Lmax} as A3 and A4 airfoils, it did have the highest stalling angle of all the airfoils of 15° and 18° for minimum and maximum *Re*. Of the 3 (A3, A4 and A9), A3 airfoil proved to show good results in both C_{Lmax} and α_{stall} at both the minimum and maximum Reynolds numbers.

Table 3.3 Maximum lift at stalling angle of attack for Reynolds numbers = 55000 and 150000

Airfoil	Minimum *Re* = 55,000		Maximum *Re* = 150,000	
	C_{Lmax}	α_{stall}	C_{Lmax}	α_{stall}
A1	1.23 (soft stall)	16	1.43	10
A2	1.15	10	1.33	14
A3	1.83	14	1.93 (soft stall)	15
A4	1.66	6	2.21	13
A5	1.37	8	1.90	13
A6	1.24	10	1.53 (soft stall)	16
A7	1.33 (soft stall)	12	1.44	10
A8	1.31	12	1.34	12
A9	1.62	15	1.77 (soft stall)	18
A10	1.43	10	1.63 (soft stall)	14

3.6.2 Optimum lift coefficient and L/D ratio at minimum and maximum Reynolds numbers of 55,000 and 150,000 respectively

Optimum C_L and L/D ratio were read off from the graphs of C_L vs. C_D (drag polar plots) of each airfoil. For any airfoil, maximum C_L occurs at the stalling angle of attack, α_{stall} and maximum L/D ratio occurs at $\alpha < \alpha_{stall}$. Therefore optimum C_L and L/D ratio will fall in between α where L/D ratio is maximum and in between α_{stall} where C_L is maximum [33]. The lift coefficients were selected such that both C_L and L/D ratio are maximized in relation to each other. From the drag polar plot, optimum lift coefficient is chosen just before lift becomes constant and drag starts to increase rapidly. At this value of C_L the corresponding L/D ratio will be optimum. This point can be identified on the drag polar graphs by the sharp turning point on the curve (clear in appendix 1, figure A1.24). When the transition between lift and drag coefficients is a smooth one (appendix 1, figure A1.18), it is not clear at which point within the curve both C_L and L/D ratio are maximum. When this is the case compromises between C_L and L/D ratio has to be made and either C_L or L/D ratio is selected to be the optimum value. Table 3.4 below shows the optimum values of C_L and L/D ratio and corresponding angle of attack for the 10 airfoils. A3, A4 and A9 airfoils show good C_L and L/D ratios compared to the other airfoils at both the minimum and maximum Reynolds numbers.

In table 3.5 the omission of airfoils A2, A6, A8 and A10 were done because of their low C_L and L/D ratios. The other airfoils were sorted in accordance to the highest of C_L and L/D ratio

combination. The minimum and maximum of C_L and L/D ratio was both the subject of optimization. Out of all the other airfoils A3 airfoil displayed the maximum C_L and L/D ratio at Re = 55,000. In comparison to A3, A4 airfoil has 15.7% more C_L but 15.9% less L/D ratio at Re = 150,000. As a result A3 airfoil (s1210) was chosen as it had good combinations of C_L and L/D ratio at both the minimum and maximum values of Reynolds number chosen for the analysis.

Table 3.4 Optimum values of lift coefficients and lift to drag ratios and corresponding angle of attack for Reynolds numbers = 55000 and 150000

Airfoil	Optimum C_L range		L/D range		Angle of attack, α (°)	
	Re=55,000	Re=150,000	Re=55,000	Re=150,000	Re=55,000	Re=150,000
A1	1.20	1.42	16.39	65.27	13	10
A2	1.15	1.31	23.29	37.86	10	12
A3	1.78	1.91	33.86	59.41	10	10
A4	1.66	2.21	32.49	49.97	6	12
A5	1.37	1.88	24.65	60.24	8	12
A6	1.24	1.48	24.98	46.85	10	12
A7	1.34	1.44	25.79	64.39	12	10
A8	1.31	1.34	34.00	58.98	10	10
A9	1.55	1.67	32.01	54.80	10	10
A10	1.43	1.58	26.76	38.36	10	12

Table 3.5 Optimum values of lift coefficients and lift to drag ratios and corresponding angle of attack for Reynolds numbers = 55000 and 150000 for six airfoils arranged according to the highest of C_L and L/D ratio combination

Airfoil	Optimum C_L range		L/D range		Angle of attack, α (°)	
	Re=55,000	Re=150,000	Re=55,000	Re=150,000	Re=55,000	Re=150,000
A3 (s1210)	1.78	1.91	33.86	59.41	10	10
A4 (s1223)	1.66	2.21	32.49	49.97	6	12
A5 (s1221)	1.37	1.88	24.65	60.24	8	12
A9 (FX 63-137)	1.55	1.67	32.01	54.80	10	10
A7 (E210)	1.34	1.44	25.79	64.39	12	10
A1 (ah93w145)	1.20	1.42	16.39	65.27	13	10

3.6.3 Modification of A3, A4 and A5 airfoils geometry to improve their aerodynamic performance

Design alterations were made to A3, A4 and A5 airfoils shape to increase the aerodynamic performance of each airfoil in xfoil by changing the leading edge nose radius and increasing the trailing edge thickness.

3.6.3.1 Changing the leading edge radius

The leading edge radius was increased by 5% increments from 5% to 100%. This increase did not show any benefit towards increasing C_L or increasing L/D ratio and therefore their results are not presented. Next, the LE radius was decreased in increments of 5%. The decrease was done up to 60%, as C_L value had started to slowly degrade and C_D was gradually increasing.

3.6.3.2 Increasing the trailing edge thickness

Trailing edge thickness or gap was increased in increments of 1% of chord. The trailing edge gap in xfoil was increased symmetrically by adding thickness to either side of the camber line of the airfoil. Blending distance for the trailing edge was taken as $0.6c$ or 60% of chord for flawless mergence of the new trailing edge to the rest of the airfoil's body.

3.6.3.3 Modifying trailing edge thickness of A3 airfoil

The trailing edge thickness of A3 airfoil was increased from 1-5%. The figure below shows the modified shapes of A3 airfoil in comparison to original shape.

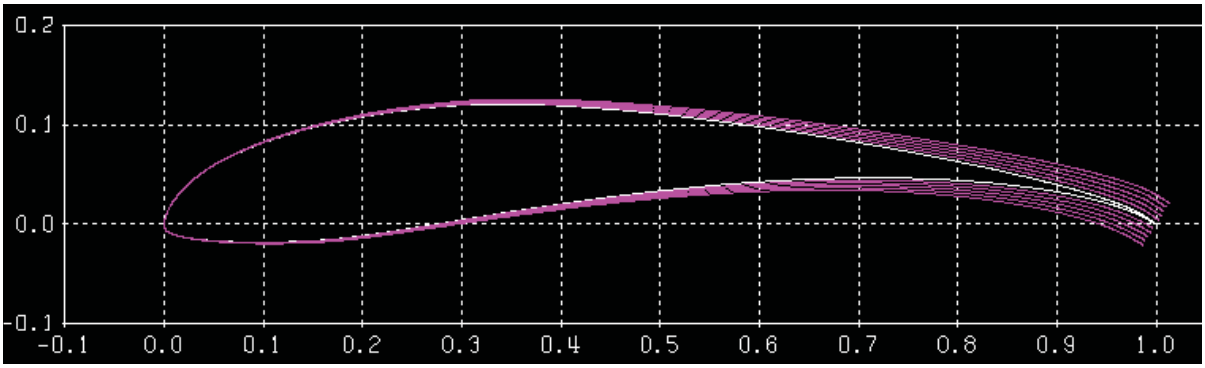

Fig. 3.1 s1210 Selig high lift low Reynolds number airfoil modified in xfoil with 1 to 5 percent trailing edge thickness variants

With increase in trailing edge thickness, there is increase in C_L for both minimum and maximum Reynolds numbers. At the minimum value of *Re* of 55000, *L/D* ratio stays fairly constant with little fluctuation in magnitude. At *Re* = 150000, *L/D* ratio tends to decrease. This is shown by the negative percentage change in *L/D* ratio. Percentage decrease of *L/D* ratio for *Re* = 150000 is more in comparison to percentage increase in C_L. With increase in thickness, C_L is increasing but overall, the percentage change is decreasing for C_L range at the minimum and maximum values of Reynolds number. The increase in trailing edge thickness, still outweigh C_L and *L/D* ratio for unmodified A3.

Table 3.6 A3 airfoil's variation in optimum C_L and *L/D* ratio with respect to the trailing edge thickness

Airfoil	Optimum C_L range				*L/D* range				α range	
	Re min	%Δ	Re max	%Δ	Re min	%Δ	Re max	%Δ	Re min	Re max
A3 (1%)	1.78		1.88		37.8		72		8	8
A3 (2%)	1.85	3.9	1.93	2.66	38.3	1.32	68.69	-4.59	8	8
A3 (3%)	1.91	3.24	1.97	2.07	39.5	3.13	65.24	-5.02	8	8
A3 (4%)	1.94	1.57	2	1.52	38.31	-3.01	61.85	-5.19	8	8
A3 (5%)	1.97	1.54	2.03	1.5	37.62	-1.8	58.63	-5.21	8	8

3.6.3.4 Modifying trailing edge thickness of A4 airfoil

Similar to A3 (s1210) airfoil's modification, A4 (s1223) airfoil's trailing edge thickness was increased. The increase was from 1 – 3%. Figure 3.2 shows the modified airfoil variants compared to the original which is white in color.

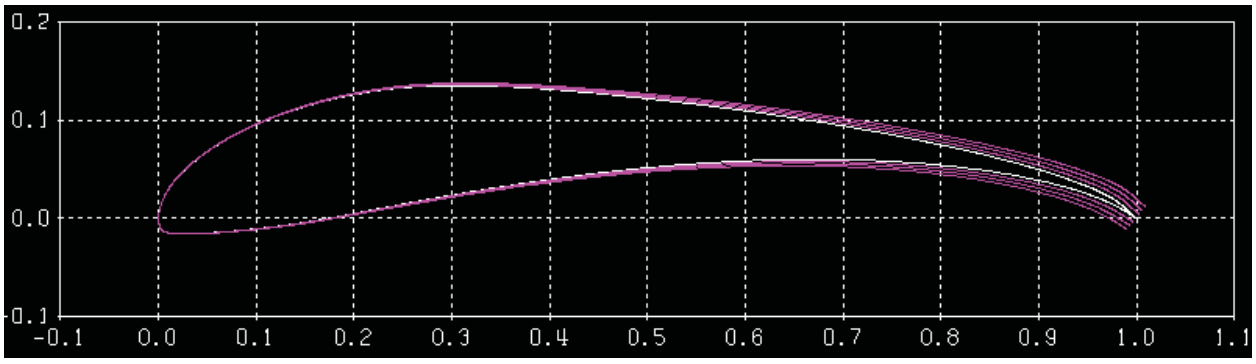

Fig. 3.2 A4 – s1233 Selig high lift low Reynolds number airfoil modified in xfoil with 1 – 3% trailing edge thickness variants

From the modification to the trailing edge thickness, the trend was that with increase in thickness, C_L increased while the corresponding *L/D* ratio decreased at both the minimum and maximum values of Reynolds number (table 3.7). The percentage change for *L/D* ratio showed an increase in the negative direction, that is a decrease in *L/D* ratio with increase in trailing edge thickness. The optimum values of C_L and *L/D* ratio occurred at different values of α of 4° and 10° at *Re* = 55000 and 150000 respectively. The increase in trailing edge thickness was increased to 3% and not further because in comparison to A3 airfoil's C_L and *L/D* ratio, A4 airfoil did not yield better results. Overall, compared with the original shape of A4, the modifications have yielded good results with both C_L and *L/D* ratio as being more.

Table 3.7 A4 airfoil's variation in optimum C_L and *L/D* ratio with respect to the trailing edge thickness

Airfoil	Optimum C_L range				*L/D* range				α range	
	Re min	%Δ	Re max	%Δ	Re min	%Δ	Re max	%Δ	Re min	Re max
A4 (1%)	1.65		2.19		41.08		55.95		4	10
A4 (2%)	1.72	4.2	2.22	1.37	40.87	-0.51	54.49	-2.61	4	10
A4 (3%)	1.77	2.91	2.27	2.25	40.12	-1.84	52.8	-3.1	4	10

3.6.3.5 Modifying trailing edge thickness of A5 airfoil

The trailing edge thickness of A5 (s1221) airfoil was increased by 1% (figure 3.3). The results showed a minute increase in C_L and *L/D* ratio from 0 - 8°. From 8° onwards, both the C_L and *L/D* ratio decreased in comparison to the original A5 airfoil. A comparison of C_L vs. angle of attack is shown, at *Re* = 55,234 and *Re* = 147289 in figure 3.4. The graph shows that C_L of A5 airfoil with 1% trailing edge thickness degrades after 8° angle of attack in comparison to the unmodified A5 airfoil at both minimum and maximum Reynolds numbers.

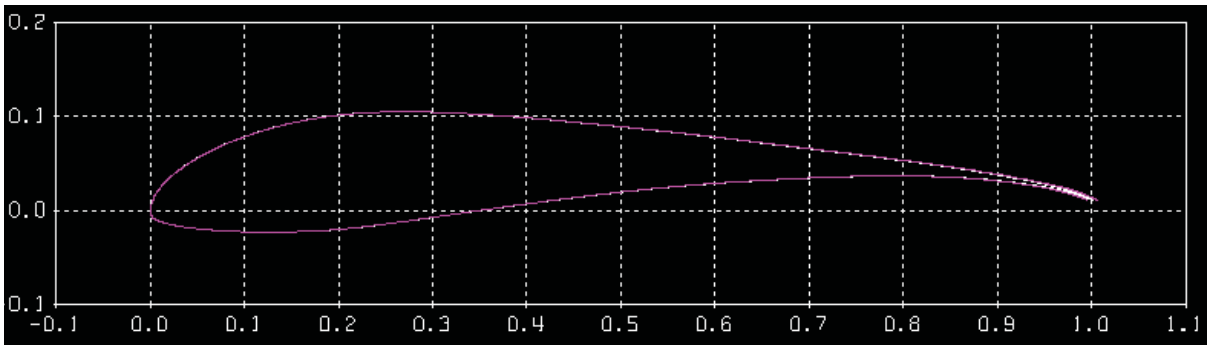

Fig. 3.3 A5 – s1221 Selig high lift low Reynolds number airfoil modified in xfoil with 1% trailing edge thickness variant

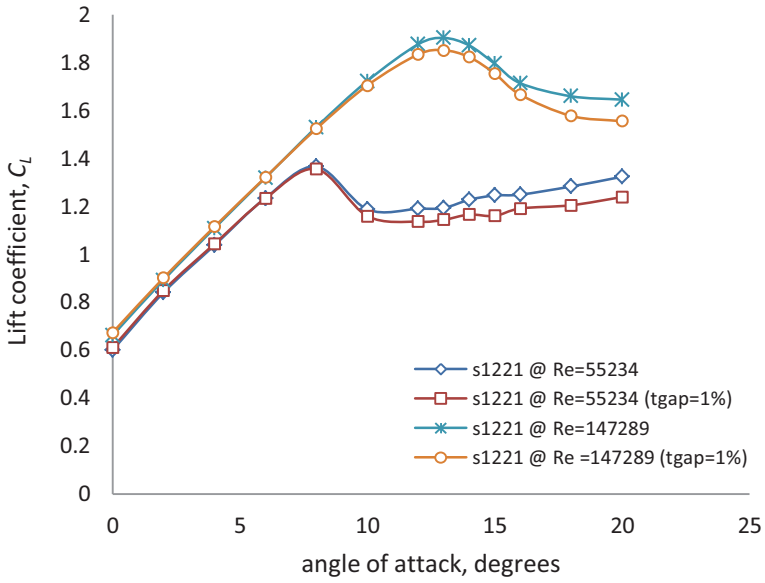

Fig. 3.4 Graph of lift vs. angle of attack at *Re* = 55000 and 150000 for A5 (s1221) airfoil with 0% and 1% trailing edge thickness

3.6.4 Choice of airfoil for low speed wind turbine

It is clear that none of the other airfoils come close to the aerodynamic characteristics of A3 and A4 airfoils in the chosen range of Reynolds numbers. As a result they were not considered for geometric modification except for A5 airfoil which was modified to see if better results of C_L and *L/D* ratio could be attained. Changing the leading edge radius of these 3 airfoils (A3, A4 and A5) produced no acceptable change to C_L. Compared to A3 and A4, A5 airfoil's aerodynamic performance degraded when its trailing edge thickness was increased from 0 to 1%. Increasing the trailing edge thickness of A3 and A4 airfoils yielded promising results in increasing C_L. While C_L increased, *L/D* ratio fell. This is due to the increase in form drag due to a *flatback* trailing edge created by increasing the trailing edge thickness. The flatback trailing edge gives rise to a low pressure flow in the near wake region [49] and thus the increase in form drag. On the other hand flatback trailing edge increases lift and lowers adverse pressure gradient reducing chances of flow separation by moving the separation point past the trailing edge into the wake region of the airfoil [49,50]. At the minimum *Re* value of 55000, A3 airfoil (comparing 1-3% increase in thickness) dominates A4 airfoil as it has higher values of C_L and similar values of *L/D* ratio. At *Re* = 150000, A4 airfoil has higher values of C_L (around 13% higher) but with lower

L/D ratio (around 26% lower). This shows that A3 has better aerodynamic performance than A4 at *Re* = 150000. A4 base airfoil and modified airfoil variants have the optimum values of C_L and *L/D* ratios occurring at different angles of attack with respect to minimum and maximum *Re* values. This means that the airfoil will be under performing at either one of the set Reynolds numbers (55000 or 150000) as the rotor blade would be expected to perform satisfactorily at different freestream velocities at a particular angle of attack only. A3 base airfoil and modified airfoil variants have a particular angle of attack that is common at both minimum and maximum Reynolds numbers, meaning it will perform well in the range of the set Reynolds numbers i.e. from 55000 to 150000. Table 3.8 shows base airfoils and modified airfoils arranged according to optimum C_L and *L/D* ratios with A3 (3%) airfoil displaying the best combinations of C_L and *L/D* ratio. A3 (3%) airfoil has a 6.11% increase in C_L at *Re* min, 3.41% increase in C_L at *Re* max and 16.53% & 9.83% increase in *L/D* ratio (at min & max *Re* respectively) compared to the base A3 airfoil. The new airfoil –A3 (3%) has been designated as *airfish* (AF300).

Table 3.8 Ranking of both the base as well as the modified airfoils according to optimum C_L and *L/D* ratio

Airfoil	Optimum C_L range		*L/D* range		α range	
	Re min	Re max	Re min	Re max	Re min	Re max
A3 (3%)	1.91	1.97	39.5	65.24	8	8
A3 (4%)	1.94	2	38.31	61.85	8	8
A3 (5%)	1.97	2.03	37.62	58.63	8	8
A3 (2%)	1.85	1.93	38.3	68.69	8	8
A3 (1%)	1.78	1.88	37.8	72	8	8
A4 (1%)	1.65	2.19	41.08	55.95	4	10
A3	1.78	1.86	33.9	59.4	10	10
A4	1.7	2.2	32.5	50	6	12
A4 (2%)	1.72	2.22	40.87	54.49	4	10
A4 (3%)	1.77	2.27	40.12	52.8	4	10
A5	1.4	1.9	24.7	60.2	8	12
A9	1.6	1.7	32	54.8	10	10
A7	1.3	1.4	25.8	64.4	12	10
A1	1.2	1.43	16.4	65.3	13	10

3.6.5 Comparing s1210 airfoil with AF300 airfoil at *Re* = 55000 and 150000

Figure 3.5 shows the lift characteristics of s1210 and AF300 airfoils at *Re* = 55000 and 150000. It is noticed that the flatback variant of s1210 has increased lift coefficient in comparison to s1210. At the minimum value *Re*, α_{stall} and C_{Lmax} for s1210 airfoil are 14° and 1.83. For AF300

airfoil α_{stall} and C_{Lmax} are 8° and 1.91. Soft stall is observed for both the airfoils at Re = 150000 with stalling occurring at 10° angle of attack. The corresponding C_{Lmax} at α_{stall} are 1.91 and 1.97 for s1210 and AF300 respectively. At α = 0°, both the airfoils have C_L values of 0.87 for s1210 and 1.08 for AF300 airfoil. Similar results were obtained by Selig [28] for the s1223 airfoil that produced $C_L \approx 1.1$ at Re = 200000.

The drag polar plots of the 2 airfoils in figure 3.6 show how lift and drag characteristics get affected as a result of thickening the trailing edge of s1210 airfoil. Due to the increase in thickness to 3%, the polar plot of AF300 has shifted up and towards right, increasing both lift and drag. At Re = 55000 optimum C_L and L/D ratios are 1.78 and 33.86 for s1210 airfoil and 1.91 and 39.49 for AF300 airfoil, likewise for Re = 150000, optimum C_L and L/D ratios are 1.86 and 59.41 for s1210 airfoil and 1.97 and 65.24 for AF300 airfoil. The AF300 airfoil performs well at both the Reynolds numbers with C_L values close to 2 with high L/D ratios of 40 and 65 at Re = 55000 and 150000 respectively.

Figure 3.7 shows the shape of AF300 airfoil compared to s1210 airfoil. The flatback trailing edge of the AF300 airfoil has increased both the aerodynamic characteristics and structural integrity to the design of the rotor blade. The thickening of the trailing edge has added strength to the overall design of the blade airfoil section and improved the aerodynamic characteristics. The flatback trailing edge has delayed flow separation by decreasing the APG towards the trailing edge of the airfoil upper surface. As a result there is increase in the overall lift coefficient values as compared with the base model (s1210 airfoil) (figure 3.5) but at the expense of an increased drag (figure 3.6). The increase of drag is due to the blunt trailing edge. According to the Kutta condition, for airfoils with sharp trailing edge, the flow from the top and bottom surface leave the trailing edge smoothly due to the right amount of circulation being present at the set angle of attack [22]. The top and bottom surface flows exit the trailing edge with the same velocity and at the same pressure satisfying the Kutta condition, with the sharp trailing edge serving as the second stagnation point. For a blunt or thick trailing edge, the flows on both sides of the trailing edge merge into vortices which shed aft of the trailing edge due to a low pressure region giving rise to increase in pressure drag.

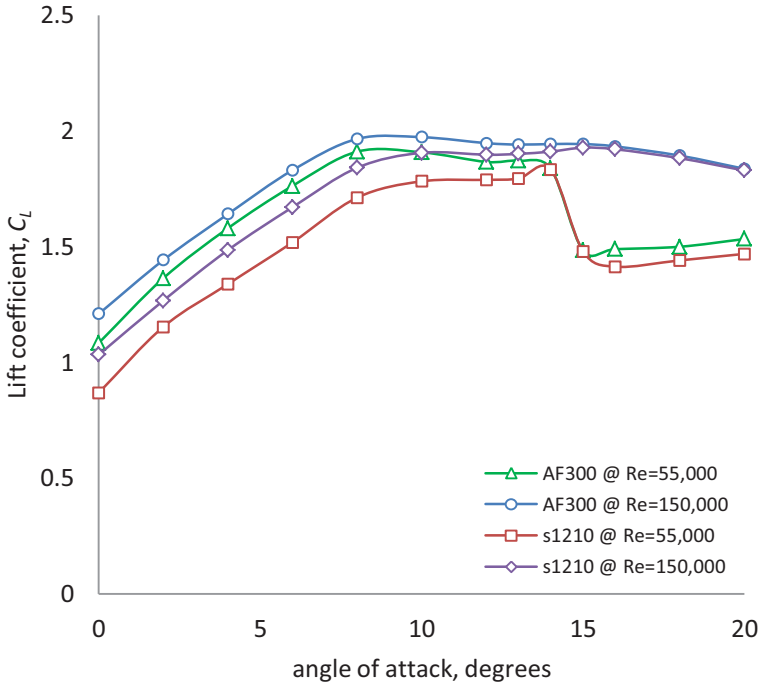

Fig. 3.5 Graph of lift vs. angle of attack at Reynolds number = 55000 and 150000

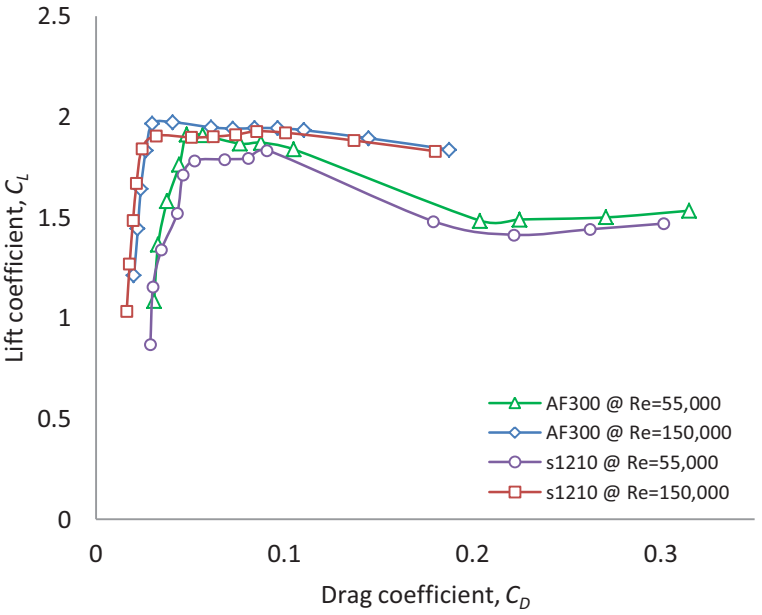

Fig. 3.6 Drag polar plot – lift vs. drag at Reynolds number = 55000 and 150000

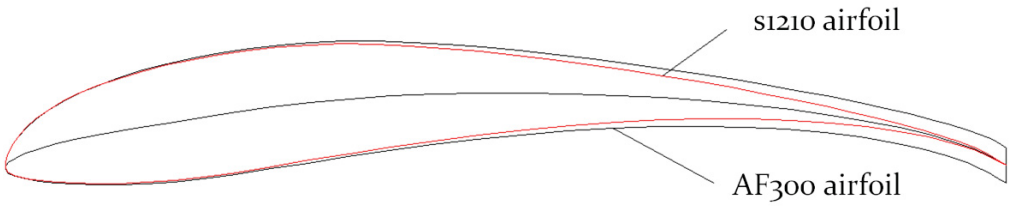

Fig. 3.7 Comparing geometry of s1210 airfoil and AF300 airfoil

Chapter 4 Testing of AF300 airfoil

4.1 Wind Tunnel testing of AF300 airfoil

Wind tunnel testing of the AF300 airfoil was conducted in an Engineering Laboratory Design (ELD) Inc. open circuit subsonic wind tunnel at different freestream velocities and angles of attack to evaluate the pressure distribution, lift and drag measurements for comparison of results with xfoil. The wind tunnel is located in the Thermo-fluids laboratory in the Engineering division of FSTE at the University of the South Pacific. The open circuit wind tunnel is a suction type, low – speed wind tunnel capable of producing airflows of 3 to 48.77 m/s having a turbulence intensity of about 0.8% at the highest velocity. A single stage centrifugal flow fan with a discharge rate of 4.53 m^3/s at a pressure head of 996.7 Pa and rotational speed of 2253 rpm generates the flow. The fan is powered by a 10 HP AC 3-phase thyristor controlled motor that is controlled via a remote operators control unit and achieves a freestream velocity resolution of 0.08 m/s in the test section. The settling chamber with honeycomb gauges and 3 high porosity screens provides for the correcting of the flow. The nozzle inlet is bell-mouthed and ensures smooth entry of air flow to the settling chamber. The chamber is square in cross-section and connects to the test section. The test section of the wind tunnel is made from Perspex clear glass and measures 305 mm x 305 mm x 1000 mm in dimensions. The flow velocity within the test section was measured with a traversing pitot-static tube connected to the test section. The pressure measurements from the pitot-static probe were read by a digital micromanometer, model FCO510. With the pitot-static probe connected to the micromanometer, the control knob on the operators' station was adjusted to match the calculated dynamic pressure to get the desired flow in the test section.

The digital micromanometer was used to measure the static pressure and surface pressure distribution on the airfoil. Two digital micromanometers were used to measure the pressure distribution, with one having a range of 196.2 – 1962Pa and the other having a range of 1962 – 19620Pa. A lift and drag dynamometer with 9.81 x 10^{-3} N resolution was used to take the lift and drag measurements of the AF300 airfoil. The dynamometer has a lift range of 0 – 8.64kg and drag range of 0 – 4.61kg.

4.2 AF300 airfoil test specimen specifications

The airfoil test specimen measures 300mm long with chord length of 100mm. Total number of pressure taps = 81 with 41 taps on the upper surface and 40 on the lower surface as shown in figure 4.1. As a result of the flatback trailing edge, it was possible to distribute pressure taps right up to the end of the trailing edge on both the top and bottom surfaces.

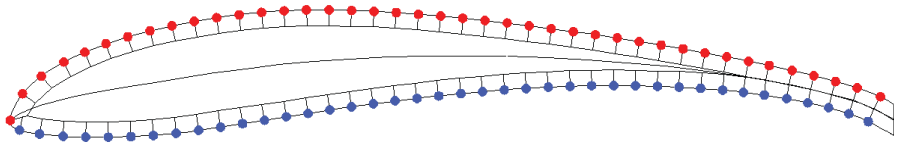

Fig. 4.1 AF300 airfoil geometry. Upper surface pressure taps (red) = 41 and lower surface pressure taps (blue) = 40

4.3 Fabrication of the AF300 airfoil specimens

The airfoil was fabricated from wood in the metal workshop at the Engineering division of FSTE. As a result of the small size of the airfoil specimen, 2 airfoils were fabricated to provide the upper and lower pressure tubes separately. Had there been just one airfoil, the pressure tubes would have coincided near the trailing edge. Three airfoil specimens were fabricated. The third airfoil was fabricated without any pressure taps to be used for lift and drag measurements.

The manufacturing of the airfoils were done on a milling machine with the aid of a gear cutting indexing head and tail stock. A template of the airfoil shape was screwed on the side of the blank wood as a guide for the end-mill bit to profile onto the 300mm length of wood. The work piece was clamped in between the indexing head's chuck and tail stock while the end mill cutter traversed along the span of the airfoil, mapping out the profile as on the template. The indexing head provided rotation along the x-axis of the milling machine so as to position the cutting surface of the cutter parallel with the curvature of the airfoil shape. Once the airfoil profile was cut, the specimen was cut to size, sanded and varnished for smoothness. Three identical airfoils were manufactured in this way through the use of the milling machine and gear cutting indexing head. The process is shown in figure 4.2.

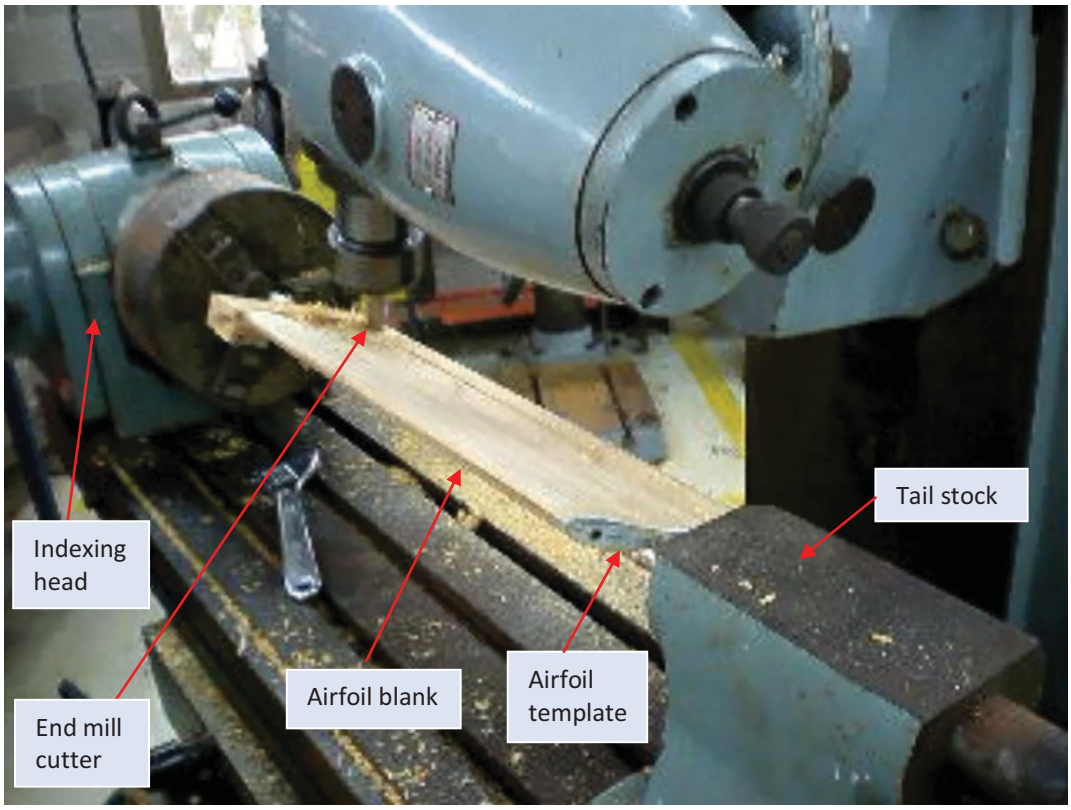

Fig. 4.2 Fabrication of the 3 airfoils that were shaped out of wood on the milling machine

Groves of width 1.58mm and depth of 2mm were cut into 2 of the airfoils to allow for the seeding of pressure tubes of 1.3mm outside diameter. The groves were cut out with a 1/16in end mill bit in the milling machine following the same process as the manufacture of the airfoils (figure 4.3). Forty one groves were cut on the upper surface of one airfoil while 40 on the lower surface of another airfoil.

Fig. 4.3 Details of groves cut into the upper surface of the airfoil for pressure tubes

Figure 4.4 shows the finished airfoil ready to be tested in the wind tunnel for upper surface pressure measurements with the pressure tubes clearly visible. The tubes are glued in place with araldite clear finish plastic epoxy glue. With the glue cured the surface is smoothed out to the airfoil profile. Pressure taps span the top surface of the airfoil along the chord in a diagonal line so as to prevent the flow, disturbed by one pressure tap being felt by the adjacent pressure taps. For this reason the pressure holes were made 0.5mm in diameter to minimize the airflow disturbances caused by the pressure tap holes. Likewise, groves were made on the lower surface of the second airfoil for lower surface pressure measurements.

.

Fig. 4.4 Finished airfoil ready for upper surface pressure measurements

4.4 Wind Tunnel Testing of AF300 airfoil - measuring pressure distribution across airfoil surface

4.4.1 Methodology

Pressure distribution measurements were taken on the lower and upper surface of the airfoil corresponding the different angles of attack and freestream velocities as shown in table 4.1. The freestream velocities relate to the relative velocities experienced on a rotating blade at mid section (0.5R) as explained in chapter 3. The relative velocities of 6m/s and 32m/s have been calculated separately at the root (0.1R) and near tip (0.95R) respectively corresponding to a freestream velocity = 5m/s, tip speed ratio and λ = 5.5 to observe the behavior of the airfoil at the 2 extreme points on the blade (near root and near tip region).

4.4.2 Test parameters

Table 4.1 Parameters for pressure distribution measurements

Angle of Attack, α (°)	Freestream Velocity, V_∞ (m/s) corresponding V_{rel} (m/s)	Relative Velocity V_{rel} (used as V_∞ in wind tunnel test section) (m/s)	Reynolds number (rounded off)
0	5	6 (@0.1R)	38,000
5	3	8.77 (@0.5R)	55,000
8	4	11.71 (@0.5R)	75,000
10	5	14.63 (@0.5R)	92,000
12	7	20 (@0.5R)	128,000
14	8	23.41 (@0.5R)	150,000
	5	32 (@0.95R)	205,000

The freestream velocity was corrected and set in the test section through the use of a pitot-static tube and remote operators' station. The pitot-static tube measured the dynamic pressure, P_d from which freestream velocity; V_∞ was calculated using equation 4.1. Likewise, the set freestream velocity was used to calculate the corresponding dynamic pressure. With the pitot-static probe connected to the micromanometer, the control knob on the operators' station was adjusted to match the calculated dynamic pressure that streams 'live' from the micromanometer. The matched dynamic pressure on the micromanomenter means that the set freestream velocity is flowing through the test section.

$$\frac{1}{2}\rho V_\infty^2 = P_d \qquad (4.1)$$

The ambient temperature was constantly monitored for any changes as it affects the air density. Any small changes in density have dramatic effects on the pressure measurements on the airfoil surface within the test section. A thermocouple was used to monitor the ambient temperature. The ambient temperature and air density are related in equation 4.2. Any changes to temperature meant a change to air density that relates to a change in the freestream velocity. Thus whenever the ambient temperature changed the flow in the test section was adjusted to maintain constant velocity.

$$P_{atm}v = mRT, \qquad P_{atm} = \rho RT \qquad (4.2)$$

Where P_{atm} is the atmospheric pressure (101.3kPa)

T is the ambient air temperature in Kelvin

ρ is the air density (kg/ m^3)

R is the gas constant for air (0.287kJ/kg.K)

Pressure measurements along the upper and lower surfaces were measured under 42 different combinations of V_∞ and α. The freestream velocity chosen for the wind tunnel is related to the relative velocity (V_{rel}) that the blade 'sees' while rotating with a tip speed ratio, λ = 5.5. A total of 81 pressure taps spanning the whole surface of the airfoil meant that a total of 81 pressure measurements could be taken via digital micromanometer, having an accuracy of 3 decimal places and value averaging function. In total 3402 pressure readings were taken with some of the sets being repeated at least 1-3 times to check the repeatability in the results.

The pressure distribution measured via manometer at each pressure tap on the airfoil at a specific value of V_∞ and α was taken in heads, more specifically in mm of H_2O. These were then changed to pressure readings (Pa) and later to coefficient of pressure, C_p (equation 4.3). The coefficients of pressure were plotted against *x/C* to observe the pressure distribution across the airfoil surface. The distance, *x* is measured from the leading edge of the airfoil to each of the pressure tap locations along the chord length, *C*. Both C_P and *x/C* are non dimensional thus making it possible for comparison of pressure distribution at different freestream velocities and angles of attack.

$$C_p = \frac{P_i - P_\infty}{\frac{1}{2}\rho V_\infty^2} \quad (4.3)$$

Where P_i is the surface pressure measured on the i^{th} location on the airfoil surface.

P_∞ is the freestream static pressure measured via pitot-static tube.

Figure 4.5 show the setup for pressure distribution measurements while figure 4.6 shows the schematics for the open circuit wind tunnel.

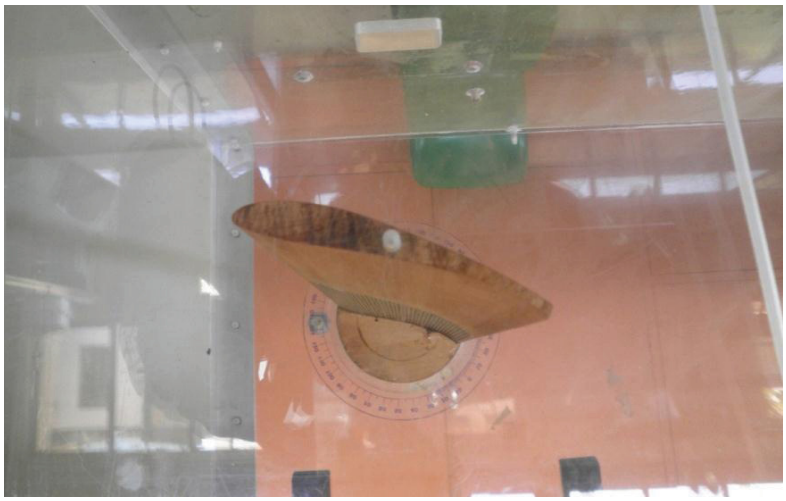

Fig. 4.5 Airfoil inserted in test section for measuring lower surface pressure distribution

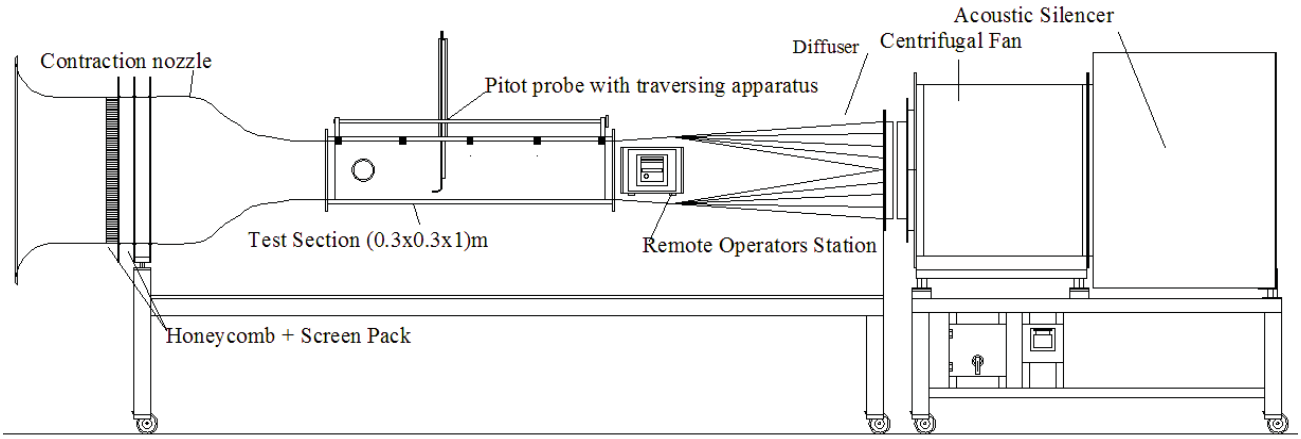

Fig. 4.6 Schematic view of the open circuit subsonic wind tunnel

4.4.3 Lift and drag measurements

Lift and drag measurements were done in the wind tunnel with a lift and drag dynamometer that attaches to the test section from the bottom (figure 4.7). A vertical beam extends half way up inside the test section to which the airfoil is pivoted to. The airfoil is free at both ends from the 2 vertical walls of the test section through the allowance of a minimum gap of 1mm at each end. This was to ensure minimal generation of tip vortices at the ends of the airfoil which would bring into picture the 3D component of a wing. The dynamometer has 2 force transducers that measure vertical (lift) and horizontal (drag) forces. The dynamometer is connected to a digital readout that displays the lift and drag measurements in kilograms with accuracy of 1gram (figure 4.8). Before proceeding with the experiment, the dynamometer was calibrated for lift and drag measurements. With the calibration complete, the dynamometer was setup for the airfoil lift and drag measurements. It must be noted that once the airfoil is attached to the beam of the dynamometer, the 2 force transducer must be zeroed again to take the weight of the airfoil into account. The experiment took place with the test parameters given in table 4.2 below.

Table 4.2 Test parameters for lift and drag measurements

Angle of Attack, α (°)	Freestream Velocity, V_∞ (m/s) corresponding V_{rel} (m/s)	Relative Velocity V_{rel} (used as V_∞ in wind tunnel test section) (m/s)	Reynolds number (rounded off)
0	5	6	38,000
5	3	8.77	55,000
8	4	11.71	75,000
10	5	14.63	92,000
12	7	23.41	128,000
14	8	20	150,000
16	5	32	205,000
18			

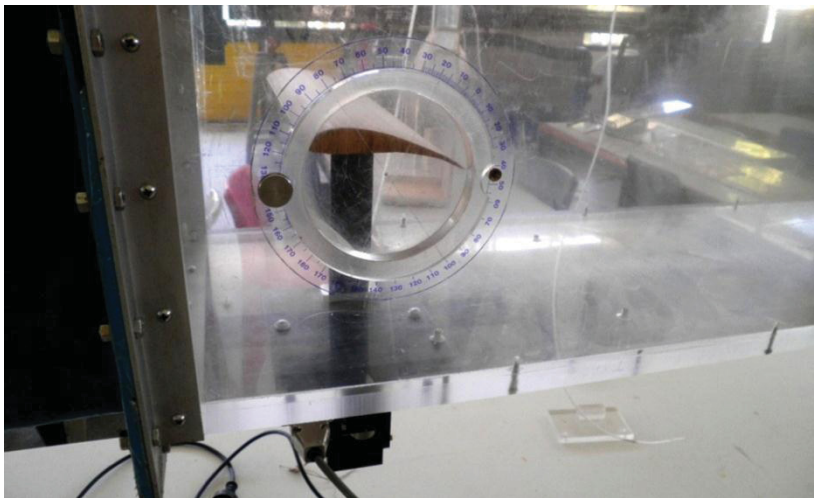

Fig. 4.7 Dynamometer fitted underneath wind tunnel test section for lift and drag measurements

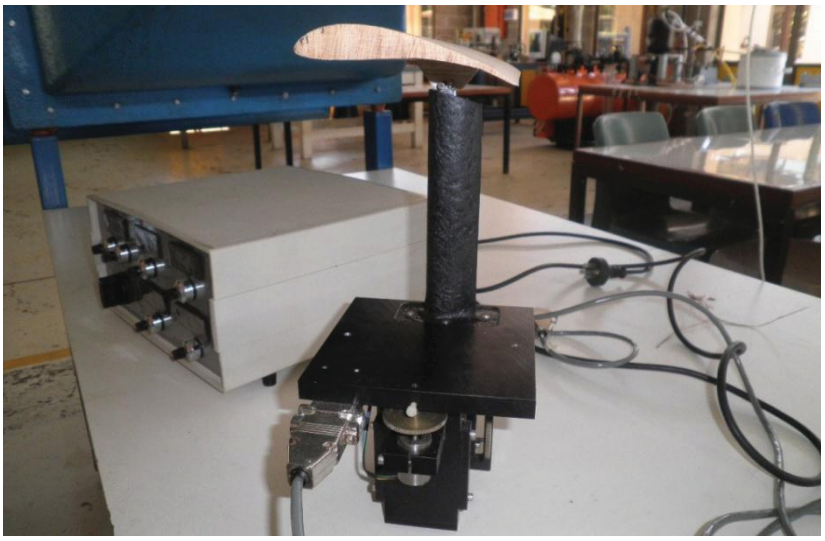

Fig. 4.8 Experimental equipment for lift and drag measurements with fabricated airfoil fitted to dynamometer and digital readout box

4.4.4 Calculation of lift and drag coefficients

Equations 4.4 and 4.5 were used to calculate the lift and drag coefficients of the airfoil from lift and drag forces measured in *kg* using the dynamometer.

$$L = \frac{1}{2}\rho A V_\infty^2 C_L\,,\;\; C_L = \frac{2L}{\rho b c V_\infty^2} \qquad (4.4)$$

$$D = \frac{1}{2}\rho A V_\infty^2 C_D\,,\;\; C_D = \frac{2D}{\rho b c V_\infty^2} \qquad (4.5)$$

Where L and D are the lift and drag forces in Newton.

c is the chord length of the airfoil (0.1m).

b is the span of the airfoil (0.3m).

4.4.5 Solid blockage correction

Solid blockage becomes an issue when the ratio of the frontal exposed area of the airfoil to the test section cross sectional area becomes more than 10%. This occurs as the angle of attack for the airfoil is increased. With increasing angle of attack, the solid blockage increases. The area between the airfoil and top and bottom walls of the test section decreases, giving rise to the acceleration of flow within this region (nozzle effect takes place as the flow sees a constrained area). This gives rise to inaccurate pressure, lift and drag measurements that are more than they should be due to the increase in flow velocity across the airfoil surface. Equations 4.6 and 4.7 provide the solid blockage correction [51] that must be made the freestream velocity. Table 4.3 shows the results of the corrected velocities based on equations 4.6 and 4.7.

$$V = V_u(1 + \varepsilon^{sb}) \qquad (4.6)$$

$$\varepsilon^{sb} = \frac{K_1(model\ volume)}{C^{\frac{3}{2}}} \qquad (4.7)$$

Where V_u is uncorrected freestream velocity (m/s).

ε^{sb} is the solid blockage correction factor.

K_1 is the wind-tunnel correction constant for solid blockage effects (0.74).

C is the test section cross sectional area (m^2).

Table 4.3 Solid blockage correction applied to correct test section freestream velocity

α (°)	ε^{sb}	uncorrected velocity, V_u (m/s)						
		6	8.77	11.71	14.63	20	23.41	32
		corrected velocity, V (m/s)						
0	0.0164	6.070	8.873	11.837	14.802	20.235	23.685	32.375
5	0.0193	6.098	8.914	11.892	14.870	20.327	23.793	32.524
8	0.0213	6.116	8.940	11.926	14.913	20.387	23.863	32.619
10	0.0233	6.128	8.957	11.950	14.942	20.427	23.910	32.683
12	0.0253	6.140	8.975	11.973	14.972	20.467	23.957	32.747
14	0.0263	6.152	8.992	11.997	15.001	20.507	24.003	32.811
16	0.0117	6.164	9.009	12.019	15.029	20.546	24.049	32.874
18	0.0273	6.175	9.026	12.042	15.057	20.584	24.094	32.934

4.5 Results and discussion

4.5.1 Pressure distribution at various Reynolds numbers and angles of attack

Pressure distribution at V_∞ = 6, 11.71, 20 and 32m/s are presented that correspond to Reynolds numbers of 38000, 75000, 128000 and 205000 respectively. Pressure distributions at the other velocities with reference to table A4.1 are given in appendix 2. The graphs in figures 4.9 - 4.12 shows that with increasing freestream velocity suction on the upper surface (curves in the negative region) are enhanced and increase considerably. This occurs because with increase in freestream velocity, the kinetic energy of the flow increases. The high energy flow possesses enough kinetic energy to overcome the adverse pressure gradient (APG) [20] and thus the flow does not separate from the airfoil surface. At lower velocities (6m/s) it is noticed that the pressure distribution, C_p becomes constant. This shows that the flow fails to recover as it is not able to overcome the APG. This may lead to flow separation which leads to a sudden loss in lift and increase in drag. Figure 4.10 shows pressure distribution at Re = 55000. As the velocity is increased, there is no sign of constant pressure indicating pressure recovery and flow is fully attached to the surface and flow separation does not occur across the airfoil up till 14° angle of attack as upper surface pressure is constant throughout the upper surface. At Re = 75000 (figure 4.11), there is no sign of flow separation as the upper surface pressure distribution recovers at all the angles of attack. At Re = 205000 (figure 4.12) the pressure fails to recover at 12° and 14° angle of attack as it becomes constant at around x/C = 0.45. At all other angles of attack the flow is attached to the airfoil surface.

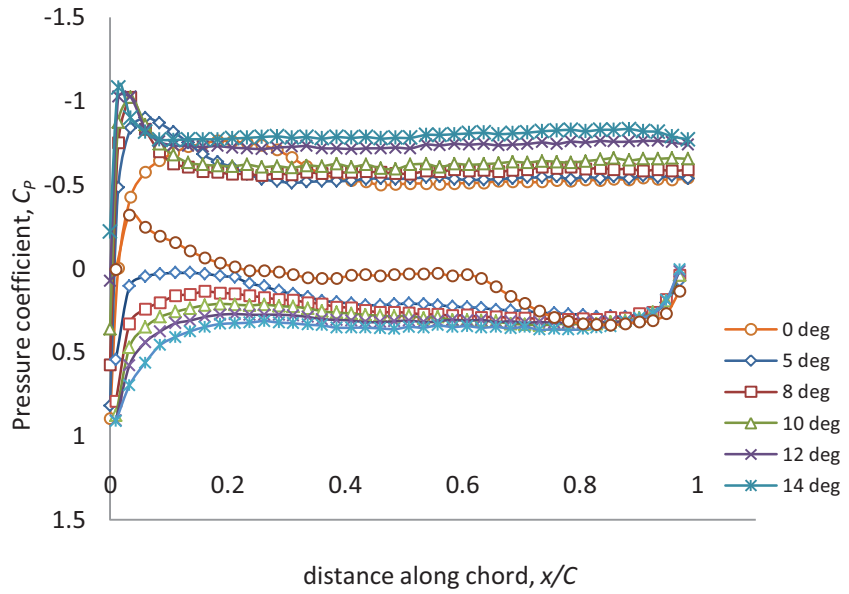

Fig. 4.9 Graph of pressure distribution vs. *x/C* at various angles of attack at Reynolds number = 38000 (V_∞ = 6m/s)

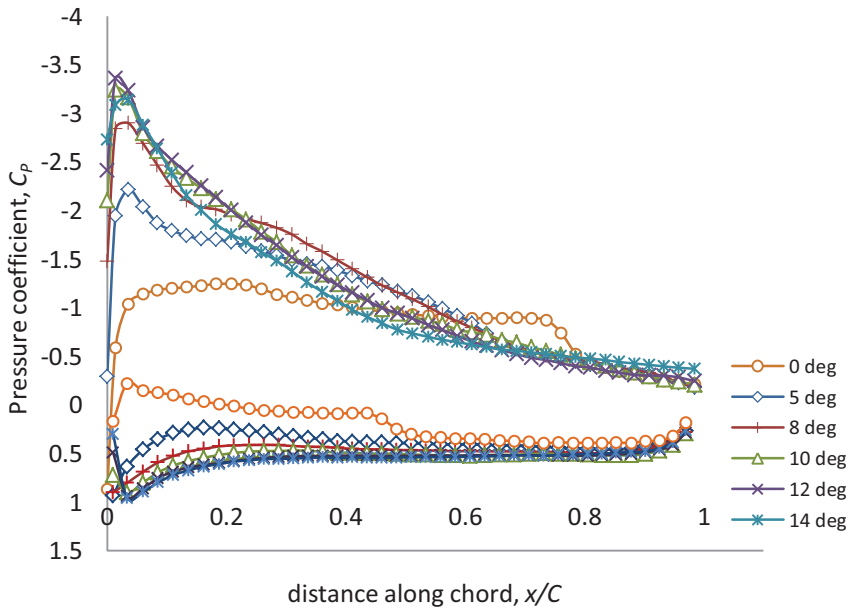

Fig. 4.10 Graph of lift pressure distribution vs. *x/C* at various angles of attack at Reynolds number = 55000 (V_∞ = 11.71m/s)

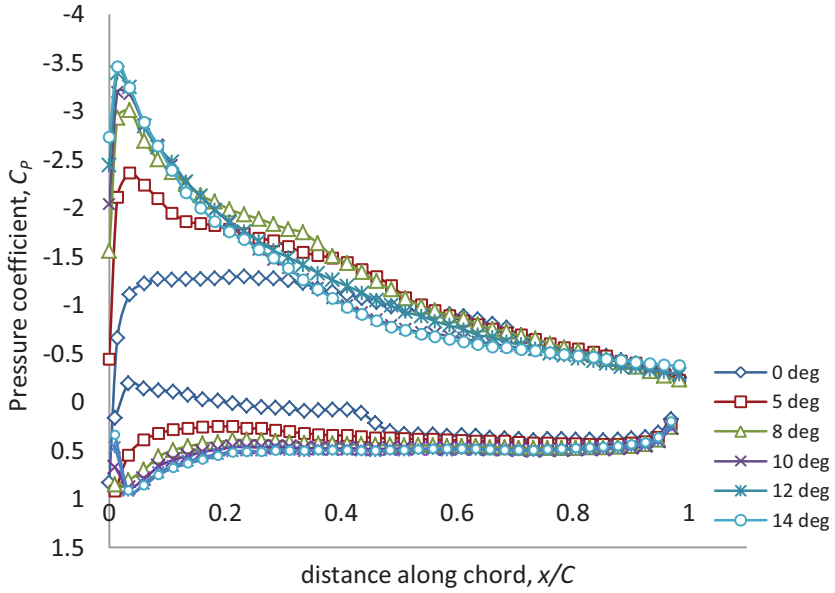

Fig. 4.11 Graph of pressure distribution vs. *x/C* at various angles of attack at Reynolds number = 75000 (V_∞ = 20m/s)

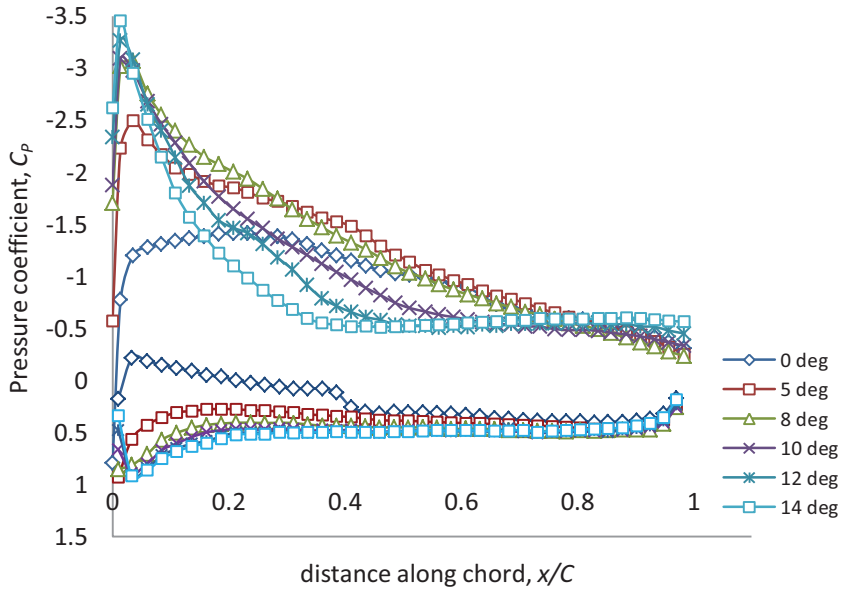

Fig. 4.12 Graph of pressure distribution vs. *x/C* at various angles of attack at Reynolds number = 205000 (V_∞ = 32m/s)

4.5.2 Variations of coefficients of lift and drag at various Reynolds numbers and angles of attack

Figure 4.13 shows the experimental variation of lift coefficients of AF300 airfoil at Reynolds numbers of 38000, 75000, 128000 and 205000. It is seen that with increase in Reynolds number, variation of lift coefficients also increases. At Re = 38000, C_L increases linearly with α. The C_L values range from 0.41 – 1.05 for α range of 0 - 18°. This is a common observation at low Re where the relationship between lift and α is linear with the flow being smooth and attached over most of the upper surface of the airfoil [22]. At low Re, the flow is highly viscous and the resulting thick boundary layer alters the shape of the airfoil. The viscous effects smoothens and increases the high pressure gradient present near the nose of the airfoil resulting in the reduction in height of leading edge suction peak as well as APG that combine to delay separation and stall. At low Re the boundary layer decreases the effective camber with increase in α which furthers the delay in separation extending the lift linear range of the airfoil further. Even after flow separation, due to the low Re, the drop in the lift curve is less distinct. The result is an overall increase in C_L with α. In the Reynolds number range of 75000 – 205000 the lift coefficients increases linearly up to α = 14°. Past 14° there is a dramatic decrease in C_L indicating that 14° is the stall angle, α_{stall} for the AF300 airfoil. Maximum lift coefficient, C_{Lmax} occurs at α_{stall}. For Re = 75000, 128000 and 205000, C_{Lmax} = 1.72, 1.81 and 1.86 respectively.

The experimental variation of drag coefficients of AF300 airfoil at Reynolds numbers of 38000, 75000, 128000 and 205000 are shown in figure 4.14. The drag coefficient, C_D at Re = 38000 increases linearly with increase in α. The variation of C_D at the lowest Reynolds number of 38000 is greater in magnitude in comparison to the variations of C_D at Re =128000 – 205000 indicating the presence of a greater magnitude of form drag that is associated with high flow viscosity and thicker boundary layer and flow separation. At Re = 75000, 128,000 and 205,000, C_D increases linearly with α up to α_{stall} = 14°. From 14° onwards there is a rapid increase in C_D values indicated by the change in gradient of the graphs. This sudden increase in C_D after α = 14° shows that the AF300 airfoil has stalled and flow has separated from the upper surface well before the trailing edge. Flow separation gives rise to increase in pressure or form drag which is more dominant than skin friction drag compared to when the flow is attached to the airfoil

surface. In the separated region, a large wake of 'dead air' is created where the flow re-circulates with the flow moving in the opposite direction of freestream, so called reversed flow [22].

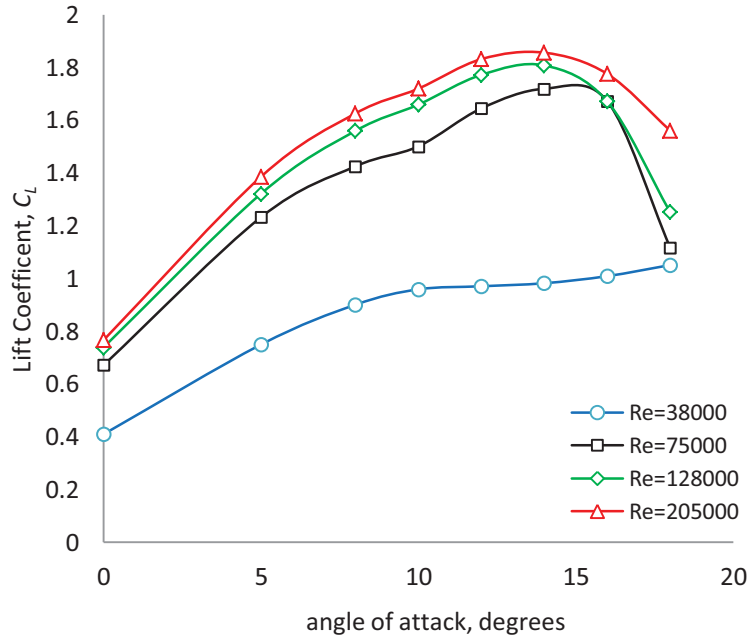

Fig. 4.13 Lift characteristics of AF300 airfoil at various Reynolds numbers

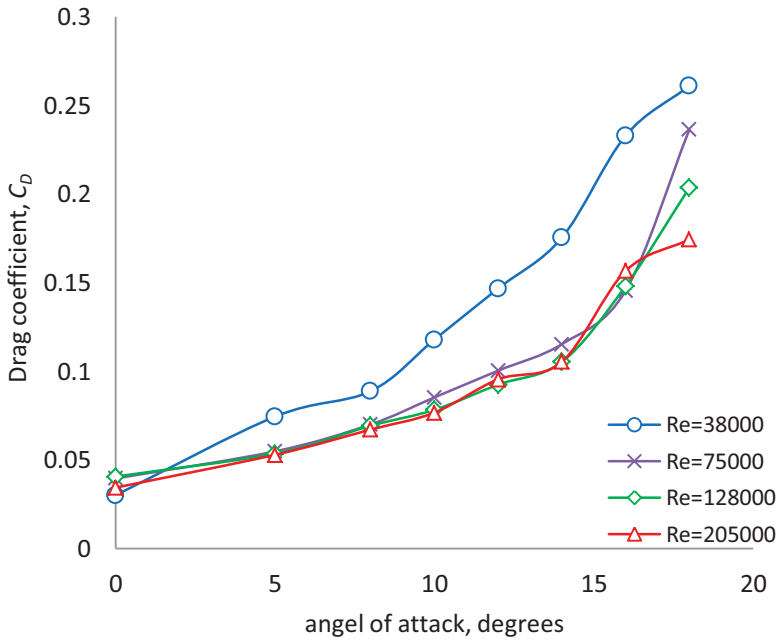

Fig. 4.14 Drag characteristics of AF300 airfoil at various Reynolds numbers

4.5.3 Drag polar plots

Figure 4.15 shows the drag polar plot at *Re* = 75000, 128000 and 205000 obtained from xfoil. The optimum values of C_L and *L/D* ratio are chosen at a point on the graph where lift becomes constant and drag increases rapidly. Table 4.4 shows the values of optimum C_L and *L/D* ratio and shows the corresponding angle of attack. At all Reynolds numbers, optimum C_L and *L/D* ratio occur at $\alpha = 8°$.

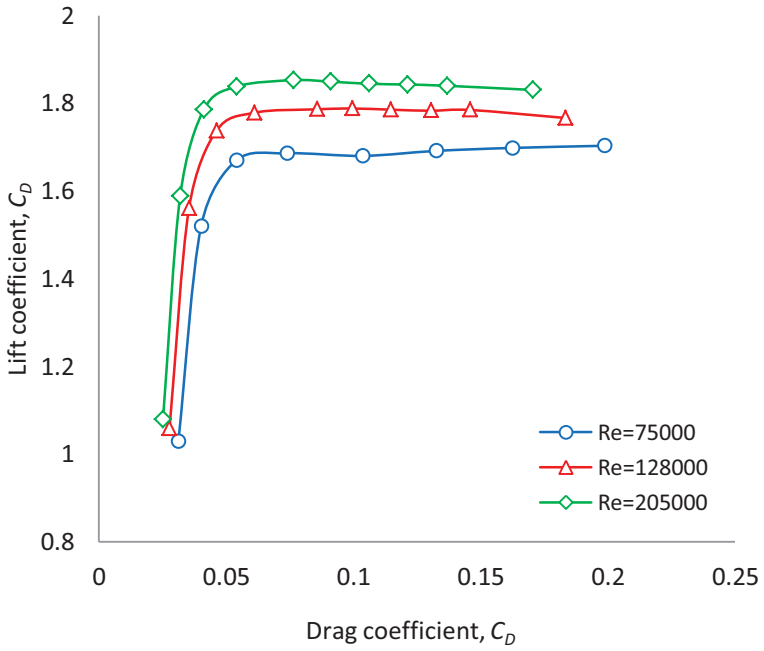

Fig. 4.15 Drag polar plot of lift coefficients vs. drag coefficients at Reynolds numbers = 75000, 128000 and 205000

Table 4.4 Optimum values of C_L and *L/D* ratio at various Reynolds numbers

Reynolds number	Optimum C_L	*L/D* ratio	α (°)
75000	1.67	30.33	8
128000	1.74	37.61	8
205000	1.78	43.27	8

4.6 Experimental and xfoil coefficient of lift characteristics at various Reynolds numbers

Figure 4.16 shows the coefficient of lift variation of AF300 at *Re* = 38000, 75000, 128000 and 205000. There is a gradual increase in C_L with α for both the experimental and *xfoil* variation of lift coefficients at *Re* = 38000. At this low reynolds number, correlation between the experimental and xfoil results diverge with increase in angle of attack.

The variation of lift coefficients at Re = 75000 for both the experimental and xfoil results show a gradual increase in lift with xfoil displaying a soft stall regime in which lift stays fairly constant from α =10° – 18°. The experimental results show a peak at the stall angle of attack followed by a rapid decrease in lift. Stalling occurs at 14° with C_L = 1.72 and 1.69 for experiment and xfoil respectivily.

The variation of lift coefficients of AF 300 at Re = 128000 shows that there is good correlation between variation of lift coefficients for experimental and *xfoil,* with stalling occurs at 14°. Xfoil shows a soft stall regime where after stall, C_L continues to remain fairly constant with increase α. At stall, C_L = 1.81 and 1.78 for experiment and xfoil respectivily.

Similar behiaviour in the variation of lift coefficients at Re = 205000 was observed at Re = 128000 with stalling occuring at 14° and C_L = 1.86 and 1.85 for experiment and *xfoil* respectivily at the stall angel of attack.

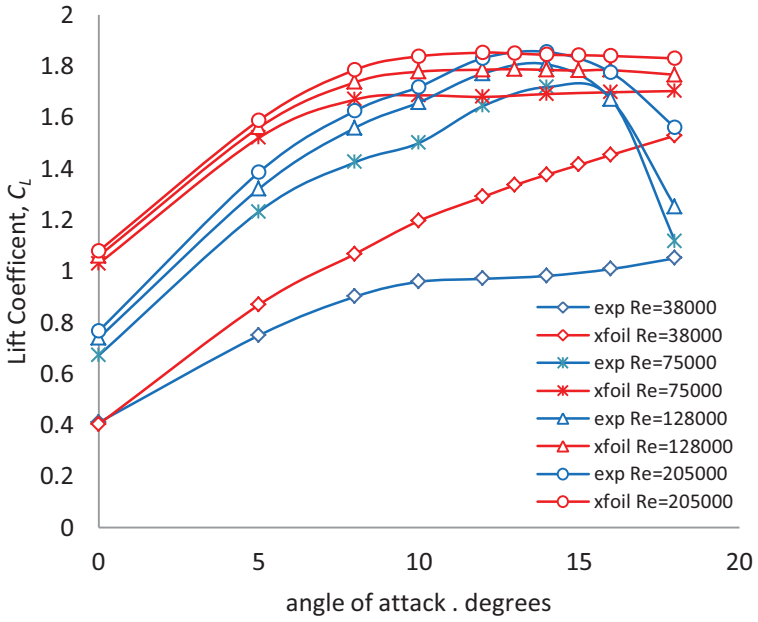

Fig. 4.16 Variation of lift coefficients of AF300 airfoil at various Reynolds numbers

4.6.1 Experimental and xfoil pressure distribution at various Reynolds numbers

Comparison between experimental and xfoil pressure distribution results are shown at $\alpha = \alpha_{stall}$ = 14° and Reynolds numbers = 75000, 128000 and 205000. Figures 4.17, 4.18 and 4.19 shows pressure distribution, C_p over the airfoil surface against cord length, x/C for α = 14° which is the

stalling angle for the airfoil. Figure 4.17 shows the graphs of pressure distribution at *Re* = 75000 for both experimental and xfoil results. There is good agreement between experiment and xfoil pressure distributions with the suction peak of -3.11 and -3.66 occurring near leading edge for experiment and xfoil respectively. Both the experiment and xfoil results show that pressure is recovering as pressure increases with increase in *x/C*.

Figure 4.18 shows pressure distribution at *Re* = 128000. Experimental and xfoil results are both presented, with good correlation between experimental and xfoil pressure distribution graphs. A suction peak of -3.46 and -4.42 was recorded near the leading edge from experiment and xfoil pressure distribution respectively. From the graph the increase in pressure across the upper airfoil surface with respect to increase in *x/C* shows signs of pressure recovery. The pressure recovery extends to the trailing edge indicating a fully attached flow regime.

Figure 4.19 shows pressure distribution at *Re* = 205000. Similar results were obtained in pressure coefficients between experimental and xfoil results as in figure 4.17 – 4.18. Peak suction for the upper surface is -3.65 and -4.87 for experiment and xfoil respectively. The graph shows the presence of pressure recovery which extends to the trailing edge indicating no sign of flow separation on the upper surface of the AF300 airfoil.

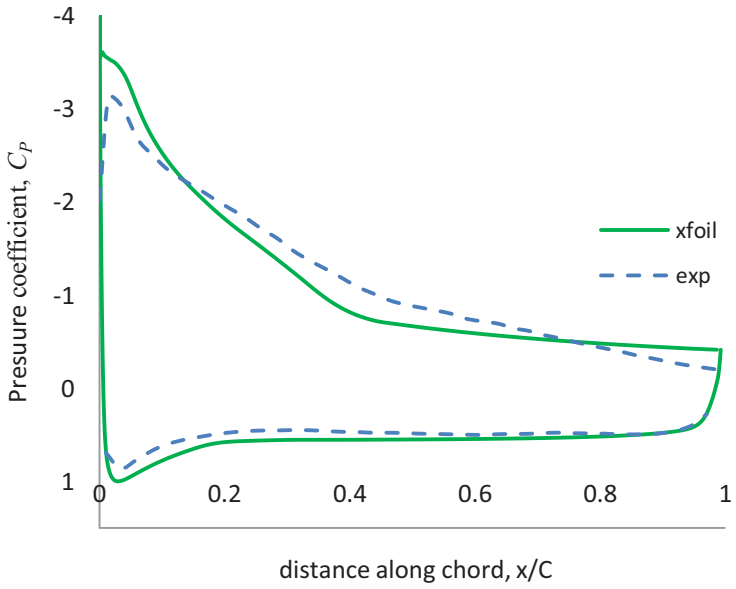

Fig. 4.17 Pressure distribution of AF300 airfoil at Reynolds number = 75000 and angle of attack = 14°

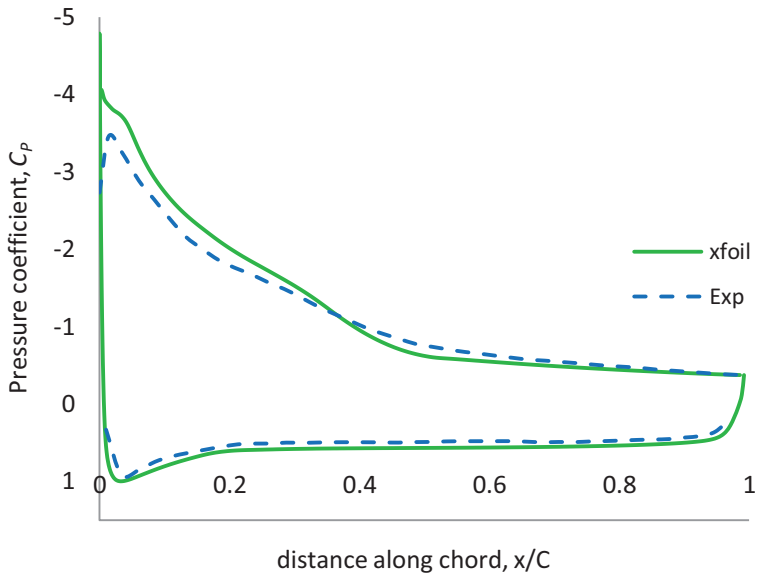

Fig. 4.18 Pressure distribution of AF300 airfoil at Reynolds number = 128000 and angle of attack = 14°

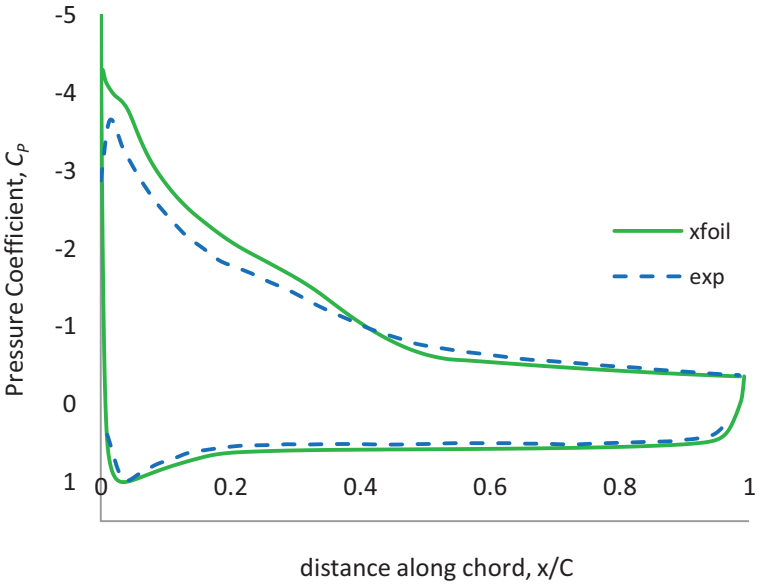

Fig. 4.19 Pressure distribution of AF300 airfoil at Reynolds number = 205000 and angle of attack = 14°

4.7 Analysis of AF300 airfoil with ansys CFX

CFD analysis of the AF300 airfoil was performed using *ansys ICEM*-CFD for meshing and *ansys* CFX- CFD for analysis. CFD analysis was performed at *Re* = 38000, 75000 and 205000 which corresponds to 6, 11.71 and 32m/s V_∞ respectively at $\alpha = 10°$ with a turbulence intensity of 1%. A hexahedral mesh was generated around the airfoil with a total of 500,000 nodes. The mesh was based on structured O-grid and C-grid topology where the size of the cells next to the walls is limited by $y+< 1$. Mesh density near the leading and trailing edges was increased to capture peak suction, stagnation point, possible transition and flow separation. A k-ω shear stress transport & transitional (SST) turbulence model was chosen. The transitional model was done with 'Gamma Theta Model'. The boundary conditions were kept similar to that of the experiments with air as the flow medium having a density that corresponds to a temperature of 25°C. The walls around the 2-D airfoil were assigned no slip condition and the inlet velocities were set so to achieve the Reynolds number set for the experiments. For the convergence criteria, the residual type of RMS and residual target value was set to 1×10^{-6}. It is seen that maximum lift for AF300 airfoil occurs at $\alpha_{stall} = 14°$. Operating at α_{stall} ensures maximum C_L at the cost of a lower value of *L/D* ratio and possible chance of stalling when α_{stall} is exceeded. A lower angle of attack is therefore chosen for the airfoil to operate at to safeguard it from stalling and to ensure that C_L and *L/D* ratio at that particular angle of attack is close to the optimum values of C_L and *L/D* ratio (C_{Lopt} and L/D_{opt}) which are obtained from the drag polar graphs.

4.7.1 Pressure distribution at 10° angle of attack at *Re* = 38000, 75000 and 205000

Figures 4.20 – 4.22 show pressure distribution of AF300 airfoil at $\alpha = 10°$. Figure 4.20 shows the pressure distribution at *Re* = 38000. Maximum peak suction = –2.13. Figures 4.21 – 4.22 shows pressure distribution plots of experiment, *xfoil* and *ansys* CFX results at *Re* = 75000 and 205000. There is good correlation between the experimental and numerical analysis. Peak suction = –2.8 and –3.18 respectively for *Re* = 75000 and 205000. All the 3 pressure distributions show that pressure recovers all the way to the trailing edge as the gradual increase in pressure is captured by the graph on the upper surface of the airfoil. The gradual increase in pressure across the upper surface of the airfoil indicates that flow stays fully attached to the airfoil surface.

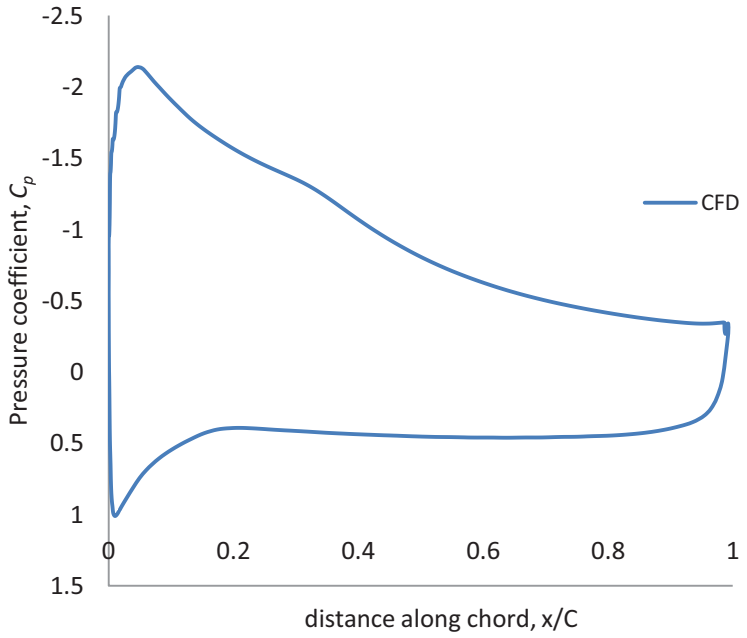

Fig. 4.20 Pressure distribution of AF300 airfoil at Reynolds number = 38000 and angle of attack = 10°

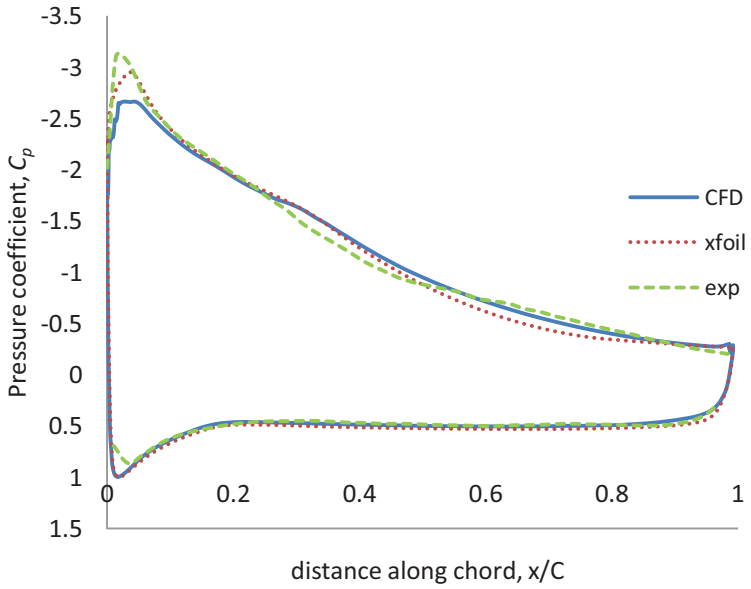

Fig. 4.21 Pressure distribution of AF300 airfoil at Reynolds number = 75000 and angle of attack = 10°

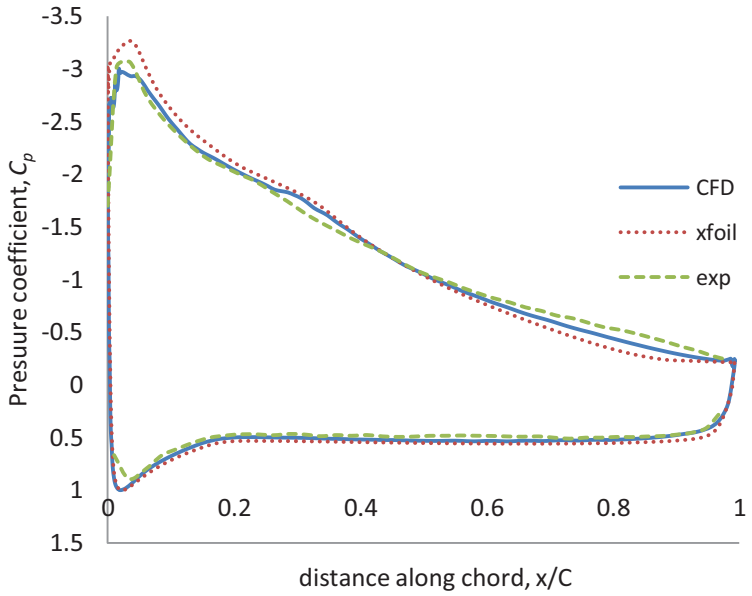

Fig. 4.22 Pressure distribution of AF300 airfoil at Reynolds number = 205000 and angle of attack = 10°

4.7.2 Transition point of AF300 airfoil

Transition from laminar to turbulent flow across the upper surface of the airfoil was determined from xfoil and can be clearly observed in the turbulence kinetic energy contour plots. Figures 4.23 – 4.25 show the turbulence kinetic energy contour plots at α =10° and *Re* = 38000, 75000 and 205000. As Reynolds number is increased, the turbulence kinetic energy increases across the upper surface of the airfoil. With increase in turbulence kinetic energy, the transition point moves further upstream towards the leading edge ensuring turbulent flow over majority of the upper surface. Although turbulent flow induces more skin friction drag than compared to laminar flow, it ensures that flow will not separate even at higher angles of attack. The turbulent flow has enough kinetic energy to overcome the adverse pressure gradient that increases as the flow travels towards the trailing edge.

Figures 4.26 – 4.29 show location of free transition point for AF300 airfoil obtained from xfoil. Figure 4.26 shows that the transition point shifts towards the leading edge with increase in α at *Re* = 205000. As the transition point shifts further upstream, laminar boundary layer gives way to turbulent boundary layer across upper surface of the airfoil. As a result, skin friction drag decreases and form drag increases. The skin friction drag decreases mainly due to the

acceleration of the flow on the upper surface and form drag increases due to thickening wake with an increase in the angle of attack for a given Reynolds number (figure 4.27).

Figure 4.28 shows location of transition point with increasing *Re* at α = 10°. As Reynolds number is increased, the transition point moves closer to the leading edge of the airfoil as a result of early transition from laminar to turbulent flow giving rise to a turbulent boundary layer. In the turbulent boundary layer, fast flowing air induces momentum to the slow flowing air particles close to the surface, energizing them. As a result there is more interaction between the air particles close to the surface and the surface giving rise to increase in skin friction. This is clearly shown in figure 4.29 where percentage skin friction drag in relation to total drag is increasing with increasing *Re*. Now as majority of the airfoil upper surface is dominated by turbulent boundary layer, the percentage form drag in relation to total drag decreases due to adverse pressure gradient (figure 4.29). Figure 4.29 also shows that at any Reynolds number the form drag is dominant compared to skin friction drag. For the AF300 airfoil at *Re* = 38000, 75000 and 205000 transition from laminar to turbulent flow occurred at 28.4%, 18.8 and 11.8% from the leading edge respectively at α = 10°.

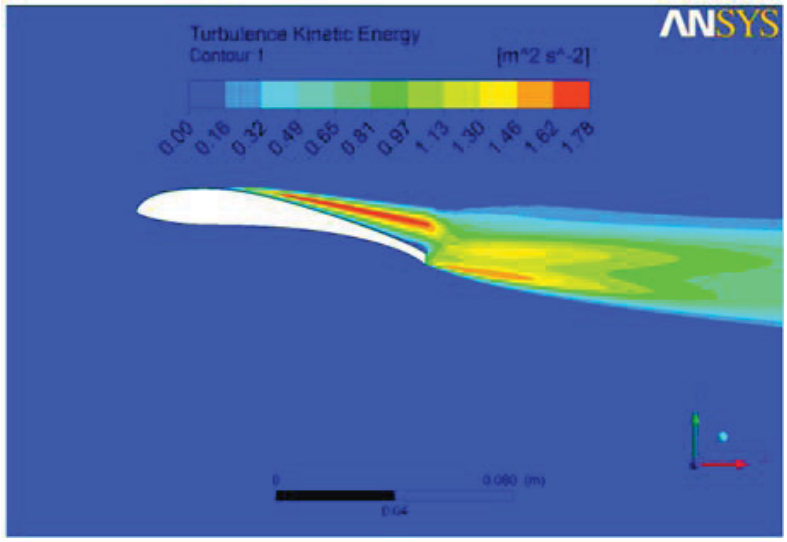

Fig. 4.23 *ansys* CFX results- turbulence kinetic energy contour plots at Reynolds number = 38000 and angle of attack = 10°

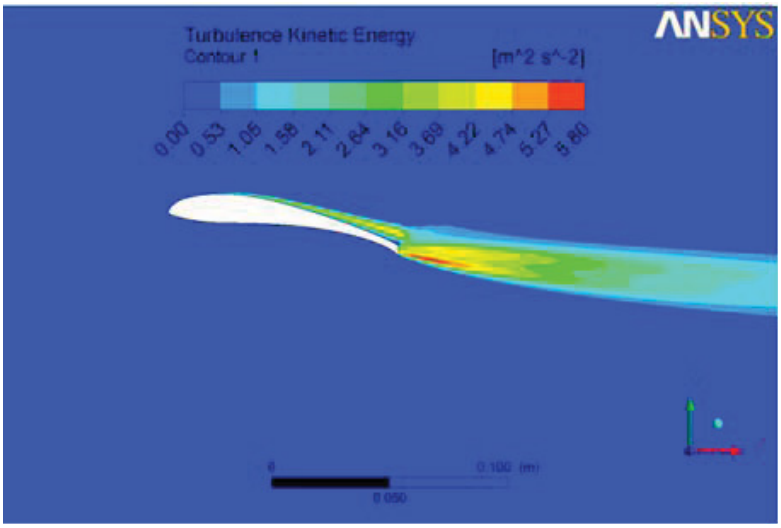

Fig. 4.24 *ansys* CFX results- turbulence kinetic energy contour plots at Reynolds number = 75000 and angle of attack = 10°

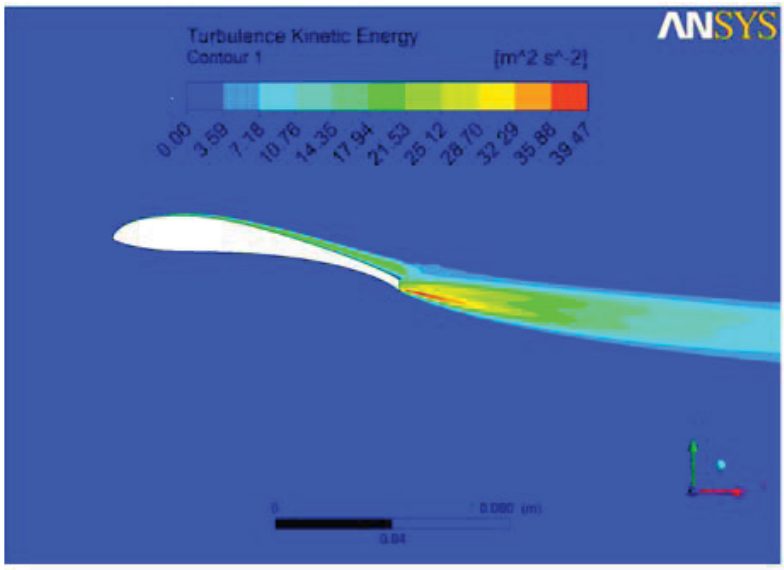

Fig. 4.25 *ansys* CFX results- turbulence kinetic energy contour plots at Reynolds number = 205000 and angle of attack = 10°

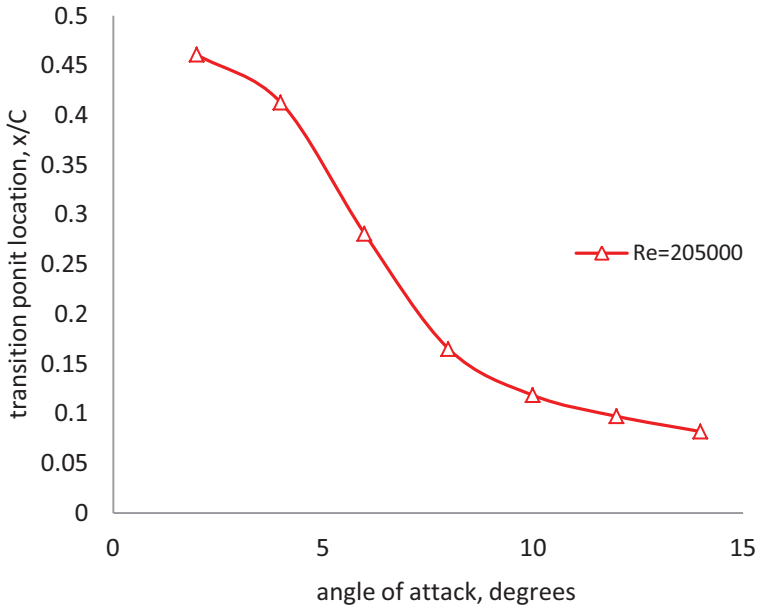

Fig. 4.26 Location of transition point with respect to different angles of attack at Reynolds number = 205000

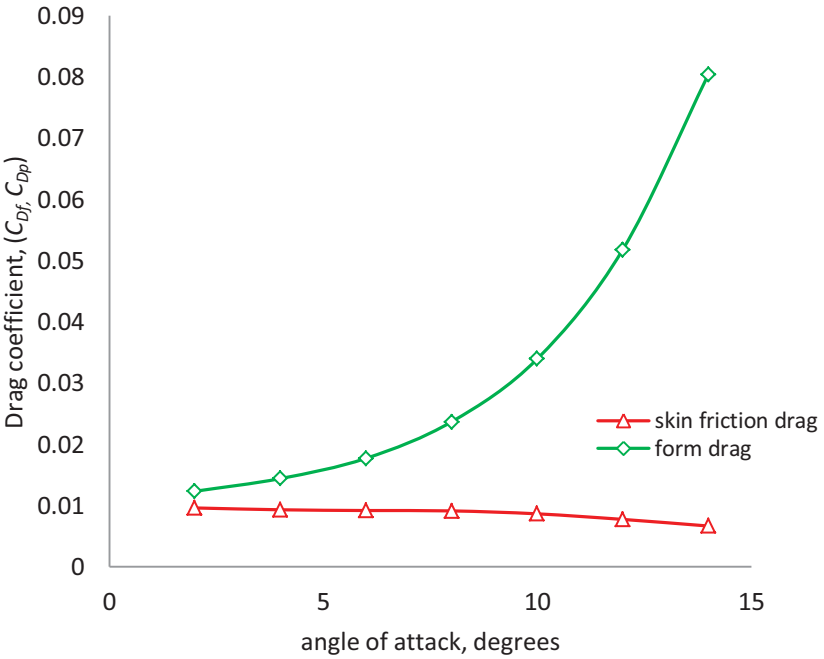

Fig. 4.27 Variation of skin friction and form drag with respect to different angles of attack at Reynolds number = 205000

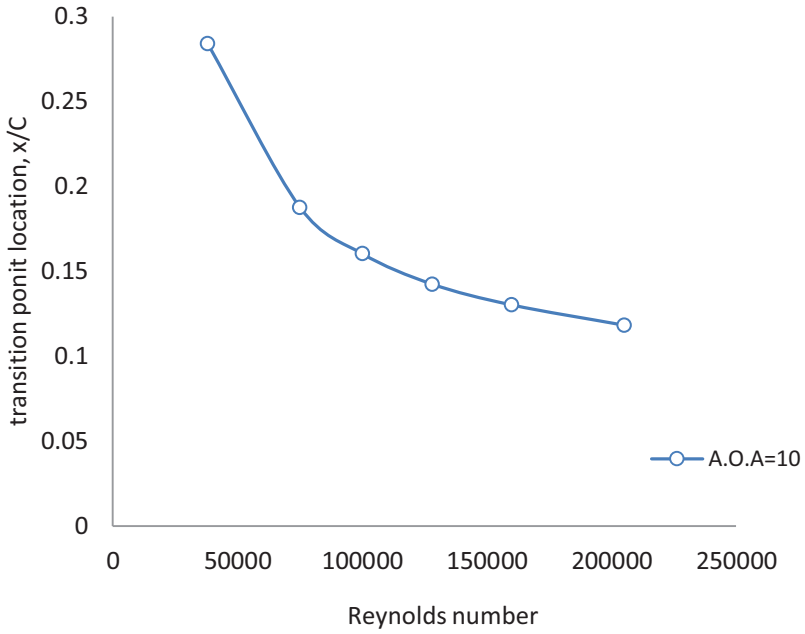

Fig. 4.28 Location of transition point with respect to various Reynolds numbers at angle attack = 10°

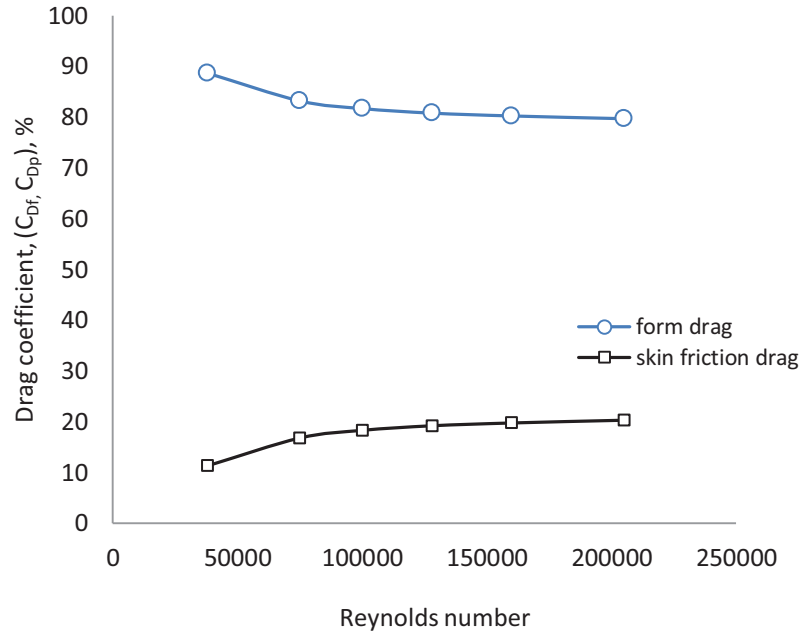

Fig. 4.29 Percentage variation of form and skin friction drag with respect to total drag at various Reynolds numbers at angles of attack = 10°

4.7.3 Velocity contour near airfoil trailing edge

The AF300 airfoil has a flatback trailing edge (figure 4.30). The flatback trailing edge ensures that separation is delayed and stalling occurs at much higher angles of attack. For the case of AF300 airfoil α_{stall} =14°. Due to the blunt trailing edge of AF300, generation of vortices is seen just behind the trailing edge. The vortices give rise to a second stagnation point known as the trailing edge stagnation point at the trailing edge, a common phenomenon associated with blunt trailing edges [52]. The outer top and bottom flow streams near the trailing edge merge smoothly without cancelling each other [52].

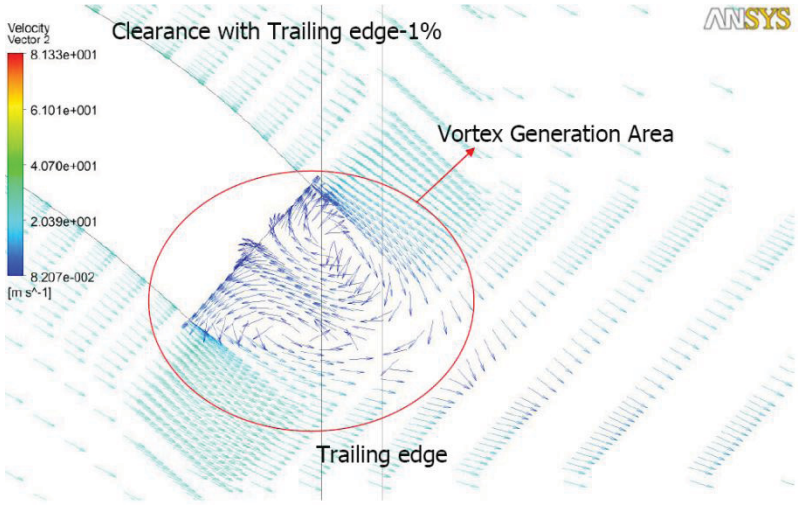

Fig. 4.30 *ansys* CFX results: Velocity contour of AF300 airfoil near trailing edge for Reynolds number = 205000 and angle of attack = 12°

4.8 Smoke flow visualization

Figures 4.31 – 4.34 show smoke flow visualization for the AF300 airfoil at Reynolds numbers of 38000, 55000 at α = 4° and 8° respectively and 75000 and 205000 at the stalling angle of attack, α_{stall} = 14°. Smoke was generated in front of the wind tunnel inlet and the flow pattern over the airfoil was captured with a CCD camera with 600 fps rate with a 4W laser as a source of illumination.

In figure 4.31 at *Re* = 38000, flow separates from the airfoil at an angle of attack as low as 4°. Separation occurs at 36% of the chord length from the leading edge. Generation of vortices is observed in the wake region just behind the trailing edge. This scenario will be experienced near the root of the airfoil when V_{rel} = 6m/s.

At *Re* = 55000 in figure 4.32, flow has separated at *x/C* = 0.304 or 30.4% from the leading edge. At Reynolds numbers of 75000 and 205000 the flow stays fully attached to the airfoil upper surface as shown by the smoke streak lines at the stalling angle of attack (figures 4.33 – 4.34).

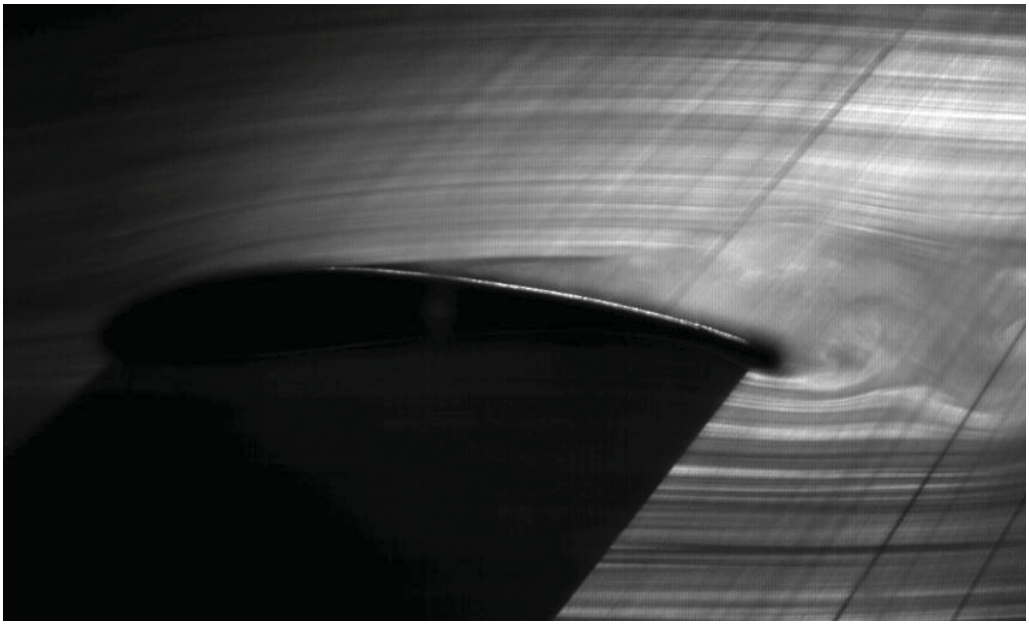

Fig. 4.31 Smoke flow visualization of AF300 airfoil at Reynolds number = 38000 and angle of attack = 4°. Signs of flow separation occurring at *x/C* = 0.36 (36%)

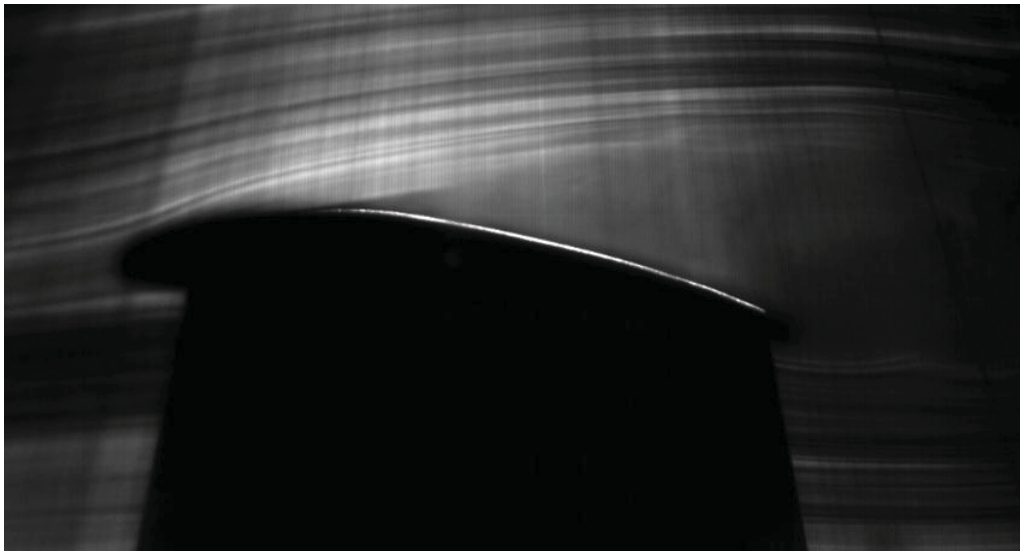

Fig. 4.32 Smoke flow visualization of AF300 airfoil at Reynolds number = 55000 and angle of attack = 8°. Signs of flow separation occurring at *x/C* = 0.304 (30.4%)

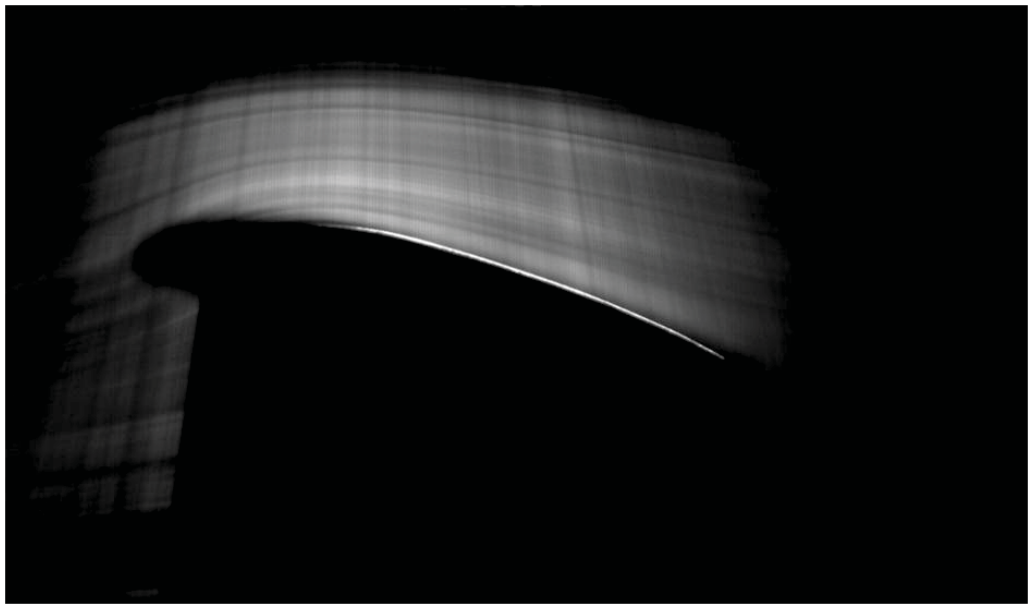

Fig. 4.33 Smoke flow visualization of AF300 airfoil at Reynolds number = 75000 and angle of attack = 14°

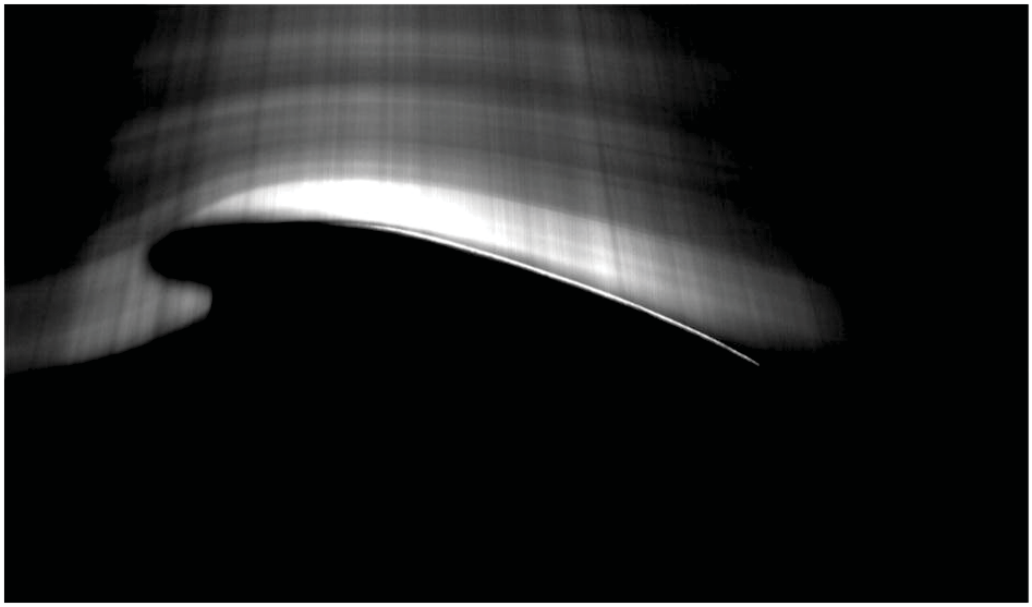

Fig. 4.34 Smoke flow visualization of AF300 airfoil at Reynolds number = 205000 and angle of attack = 14°

Chapter 5 Blade design and fabrication

5.1 Wind Turbine Rotor Blade Design

Rotor Blade Parameters

Parameters considered during the design of the wind turbine rotor blade were:

1. freestream velocity, V_∞ at which the rotor would be optimized
2. choice of airfoil section
3. number of rotor blades
4. rotor radius
5. design tip speed ratio, λ
6. chord distribution
7. twist distribution
8. rotor soilditiy, σ

5.1.1 Freestream Velocity (V_∞)

The freestream wind velocity chosen was 5m/s. It is the average wind speed that is common to the Fiji Islands.

5.1.2 The Airfoil

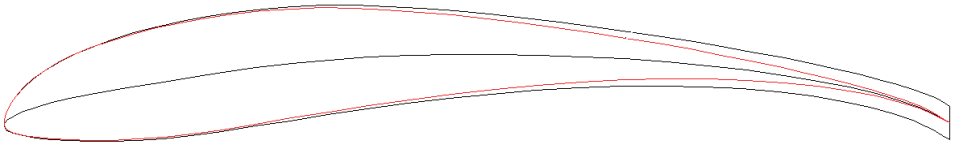

Fig. 5.1 Airfish AF300

The airfoil selected is a low Reynolds number, high lift airfoil. It displayed good C_L and L/D ratios at low Reynolds numbers. It maintained an attached flow regime at a Reynolds number of 75000 uptill 14° angle of attack. The thick trailing edge or flatback trailing edge improved both the airfoil's lift, L/D ratio and added strength to it. The optimum C_L and L/D ratios on average, coinside at a common angle of attack = 8°.

5.1.3 Number of Blades

A 2-bladed wind turbine is chosen to aid in the fast manufacture of the blades and eliminates the complexity of balancing the blades on the rotor shaft. A 2-bladed rotor has higher rotational speed as compared with a 3-bladed system at the expense of a lower value in torque. The Air X

wind turbine chosen has a direct coupling between the rotor and generator, therefore a 2-bladed system is viable in producing good rpm at low startup wind velocities and eliminate the need for a gearbox, keeping the whole design of the turbine simple.

5.1.4 Rotor radius

The radius of the rotor is a crucial part to be cosidered in the design process. The radius of the rotor is related to power extracted from wind as given below

$$P = C_P \frac{1}{2} \rho A V_\infty^3 = C_P \frac{1}{2} \rho \pi r^2 V_\infty^3 \qquad (5.1)$$

where C_P is the power coefficient of the wind turbine.

According to the equation, the available power in the wind, will increase 4 times as much when the radius is doubled. Sizing of the rotor blade has a big impact on the power output of the wind turbine. If one is to blindly increase the blade radius on a wind turbine with a particular rated power, than the rotor will damage the generator of the turbine system by overpowering it. Also the performance of the turbine will decrease and the related cost of increasing the rotor size will increase. It is therefore crucial that rotor size be optimimum for a specific rated power at a specific wind speed. The 2-bladed rotor blade designed for the *Air X* wind turbine had a 10% increase in rotor radius as compared to the stock 3-bladed rotor to yeild more performance as presented by Giguère and Selig [53] where an increase in radius of a 2-bladed system compared to a 3-bladed turbine matched its performance at the same pitch angle and wind speed, with a lower thrust value. The figure below shows the new 2-bladed rotor compared to the stock, 3-bladed rotor. The 2-bladed rotor has a span of 0.63m compared to the stock rotor's span of 0.575m.

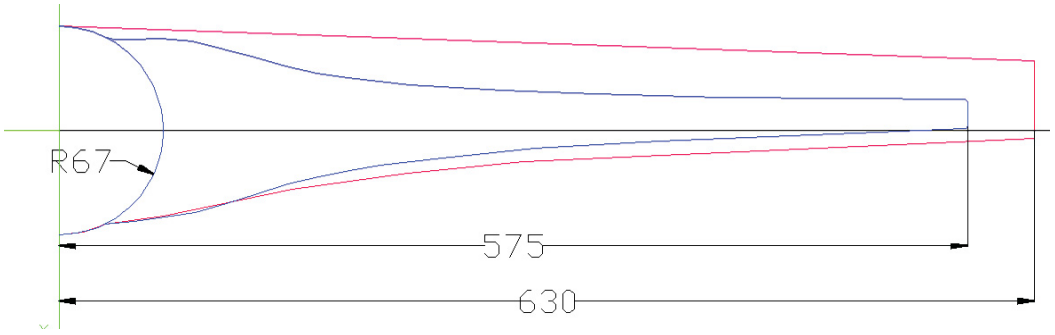

Fig. 5.2 Comparison between the stock blade and the new blade designed for low wind speed. Radius of new blade = 0.63m and for the stock blade = 0.575m. Hub radius is 0.67m. The dimensions given in the schematic are in mm

5.1.5 Design Tip Speed Ratio (λ)

A 2-bladed turbine is optimized with λ values ranging from 7 – 10 [2,54] depending on individual design parameters of 2-bladed wind turbine like rotor size and rpm. If deviatation is made from the design tip speed ratio, by either decreasing or increasing λ, then the turbine's power coefficien, C_P will decrease. The design tip speed ratio chosen for the rotor was 6.5 in relation to the design freestream velocity, V_∞ of 5m/s and rotor rpm of 500. The 500rpm is the minimum rpm at which the *Air X* generator starts generating power [2]. This is a design feature of the Air X. At the specificed rpm (500rpm), the turbine has gained sufficient inertia to start providing enough power to charge batteries. Also since the generator is never initially 'loaded', the rotor, hub and generator have minimal start-up time since the intial inertia is less. The turbine is thus able to start-up at lower wind speeds in comparison to it producing electrial power at the first rotation of the rotors.

5.1.6 Chord Distribution (Blade Taper)

Chord distribution is along the radial distance of the blade length (r/R). Chord length is measured perpendicular in relation to the radial distance whereby it is greatest near the root and decreases towards the tip. This is done to ensure that the blade is rigid and therefore structually sound [55]. The greatest magnitude of stress is felt at the root so it is the thickest. The chord distribution determines the slenderness of a blade and thus the rotor solidity, σ. The simpliest type of chord distribution is linear, making material distribution and manufacturing processes economical [55]. Theorotical chord distribution according to BEM theory is given by:

$$c(r) = \frac{16}{9} \text{x} \frac{\pi}{4} \text{x} \frac{D^2}{r} \cos^2\left[\arctan\left(\frac{d}{3\lambda r}\right)\right] \text{x} \left[\frac{1}{\lambda^2 N_b C_L}\right] \quad (5.2)$$

Where D is the overall blade diameter.

r and d are the incremental radius and diameter respectively.

N_b is the number of blades = 2.

λ = 6.5 and C_L =1 [2,56].

Figure 5.3 shows the modified chord distribution and another based on equation 5.2. The chord distribution was modified from the theoretical curve as it proved impratical to manufacture the blade due to the slender nature of the design. Figure 5.3 shows that at the root (r = 0), the chord

length (c) = 0, at r = 1.5mm, c = 370mm and close to the tip, c = 1mm. The modified chord distribution yields a more broader blade geometry. A broader outboard section towards the tip as opposed to a pointed tapering leads to an increased starting torque and better rotor power coeifficent in the partial-load range [2]. The modification brought the rotor solidity to 8.27%. At 8.27% solidity, the blade is broad enough to generate starting up torque in low wind condtions easily.

Figures 5.4 and 5.5 shows the flapwise and edgewise taper of the blade as a result of the modified chord distribution. Flapwise taper is simply the chord distribution across the span of the blade. The edgewise taper is the thickness distribution of each airfoil section along the span of the blade and is the result of the chord distrbution. In figure 5.4, the plot of both flapwise and edgewise taper is shown with respect to rotor radius. The edgewise taper is 0.1426 x flapwise taper. The ratio 0.1426 is a geometric property of the airfoil = maximum thickness of airfoil/chord length. Just like the stock blade, the new blade design incorparates a broad shape near the root to minimize efficiency losses and have efficiency as close to the theorotical optimum blade shape as possible (figure 5.6). With the curved shape near the root, the blade would have around 0.2% loss in efficiency [55].

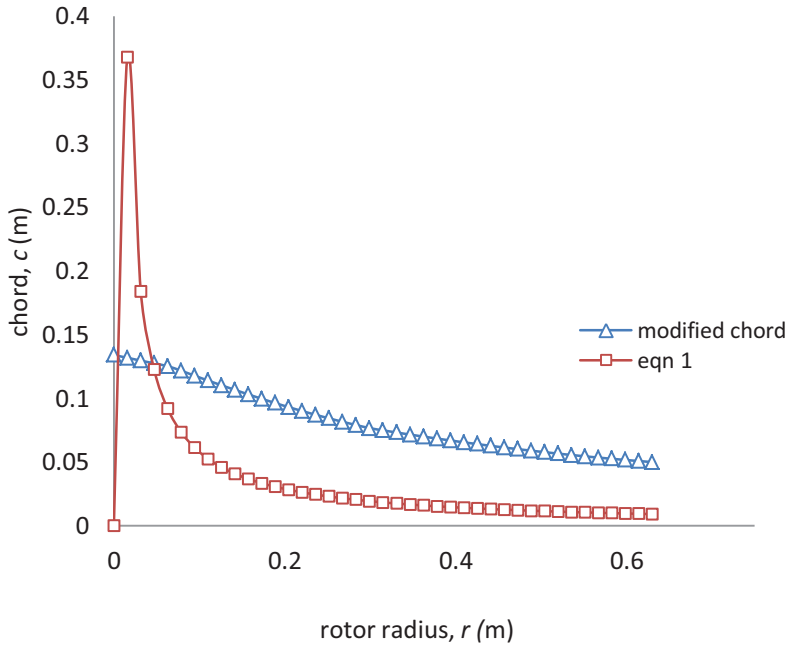

Fig. 5.3 Graph of chord distribution vs. rotor radius modified and based on equation 5.2

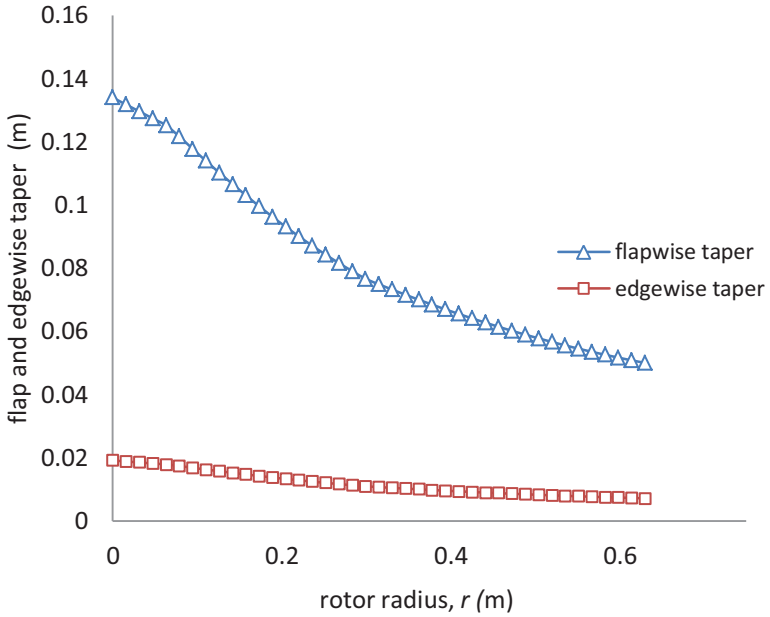

Fig. 5.4 Graph of flapwise and edgewise taper vs. rotor radius.

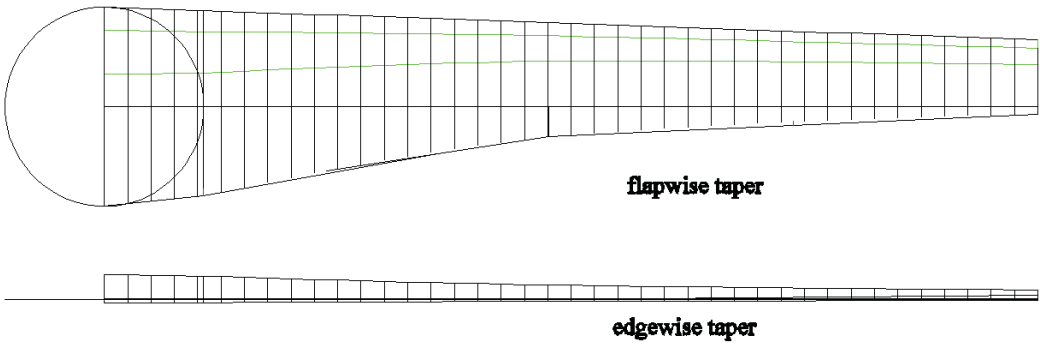

Fig. 5.5 Flapwise and edgewise taper as a result of chord distribution. Both flapwise and edgewise taper are shown with respect to zero twist distribution on the blade for clarity

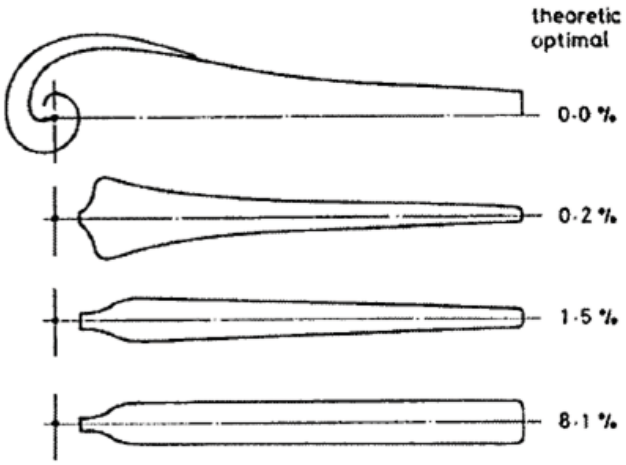

Fig. 5.6 Efficieny losses associated with different rotor shape in relation to the ideal rotor [55]

5.1.7 Twist Distribution

Apart from adding taper (chord distribution) to make the blades more rigid, a twist distribution along the blade radius must also be provided to increase rotor's aerodynamic performance. Twist consists of setting pitch angles, β (angle between the chordline and plane of rotation) at diffiernt radial distances according to the local flow conditions [55] to increase lift and L/D ratio at each radial station. Twist angle is largest at the root and gradually decreases along the radial distance towards the tip of the blade where it is the smallest. Twist distribution is governed by the relative velocity, V_{rel} and the angle between it and plane of rotation, Φ. The angle, Φ is dependent on tangential, V_{tan} and freestream, V_∞ velocities as shown in figure 5.7. From the root to tip, V_{rel} increases due to the increase in V_{tan}.. Near the root V_{rel} is small and as V_∞ is constant, Φ is large. Near the tip, the opposite happens. To achieve maximum C_L, α (angle between chord and V_{rel}) must remain constant, thus creating the need for twist.

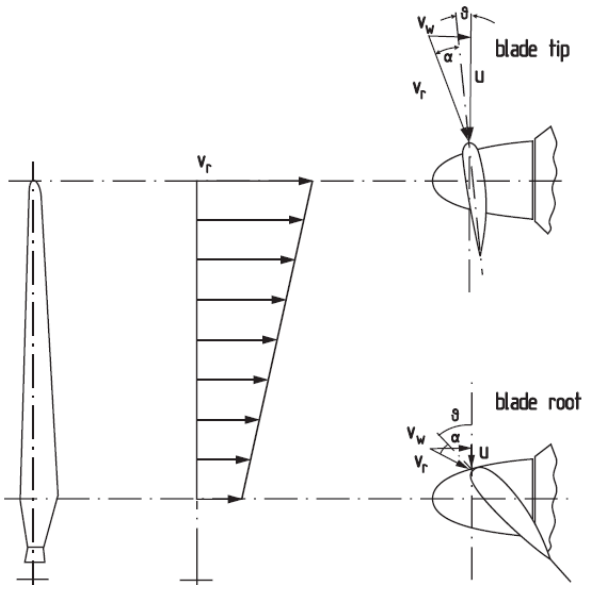

Fig. 5.7 Rotor blade twist variation along the blade radius [2]

Figure 5.8 shows twist distribution based on the relative velocity calculated from the velocity triangle:

$$\phi = tan^{-1}\left[\frac{V_\infty}{V_{tan}}\right] \quad (5.3) \qquad\qquad \beta = \phi - \alpha \quad (5.4)$$

The blade near the root is pitched at 50° and near the tip ≈ 0°.

Together with twist, the angle of attack formed between the freestream velocity and airfoil chordline is shown. The distribution is such that as we travel from the root to tip, the airfoil section is almost at 90° to the freestream velocity.

A twist distribution based on the *twist of the zero lift line* [55] is shown below:

$$\beta = \left((R\alpha_t/r) - \alpha_t\right) - k(1 - r/R) \quad (5.5)$$

where α_t is the angle of attack at the tip of the blade:

$$\alpha_t = (\phi - \beta_t) + \alpha_0 \quad (5.6)$$

α_o is the angle of attack at zero lift and β_t is the pitch angle at the tip ($\beta_t \approx 0°$.)

k is the acceleration factor ($k > 0$)

Figure 5.9 shows the twist distribution based on equation 5.5 for different values of *k*. The twist distribution with $k = 0.5$ was chosen and modified as shown in figure 5.10. The twist distribution with $k = 0.5$ produces twist distrubtion that is more consistently spread across the span of the blade from root to tip, especially in the mid range section of the blade as compared to graphs with values of $k > 0.5$.

Figure 5.10 shows the modified twist distribution in comparison to twist based on equation 5.4. The modified twist distribution has the pitch angle distributed more evenly along the whole length of the blade than compared with the theoretical twist distribution. Pitch at root = 20° and at the tip = 3°. In the case of starting up, the blades will have a pitch setting of 17° (Pitch at root = 17° and at the tip = 0°). Lower pitch setting helps in the start-up and produces more rotor power in low wind speeds [2].

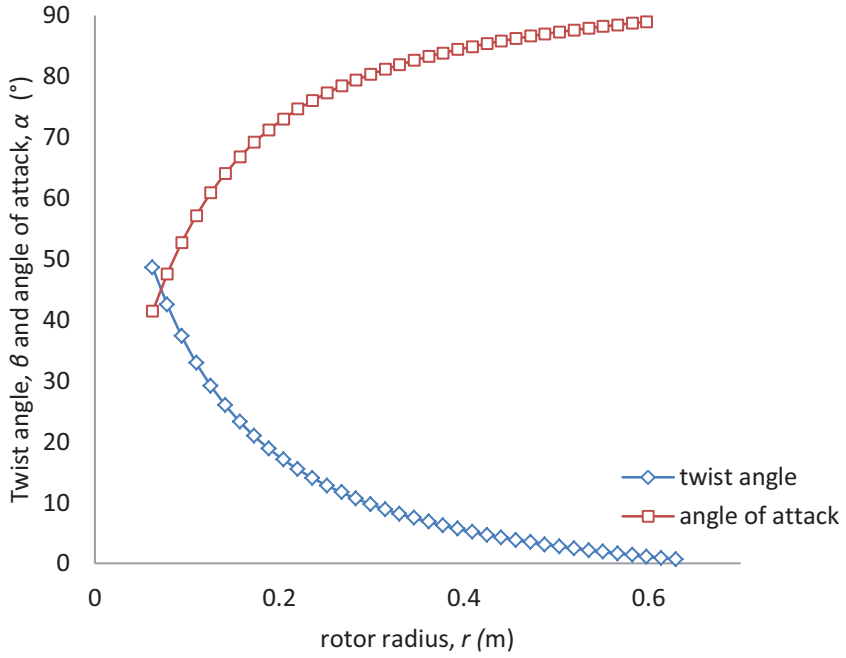

Fig. 5.8 Blade twist distribution based on the velocity triangle

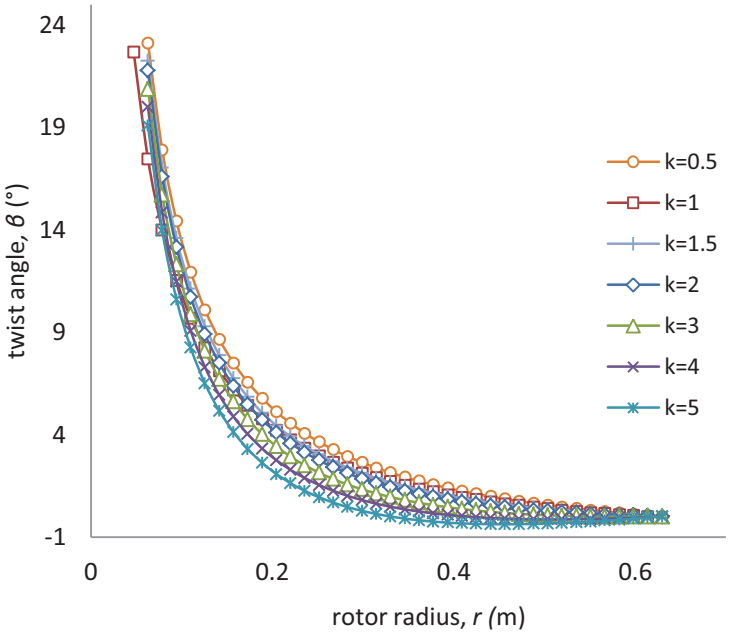

Fig. 5.9 Blade twist distribution based on the twist of zero lift line equation

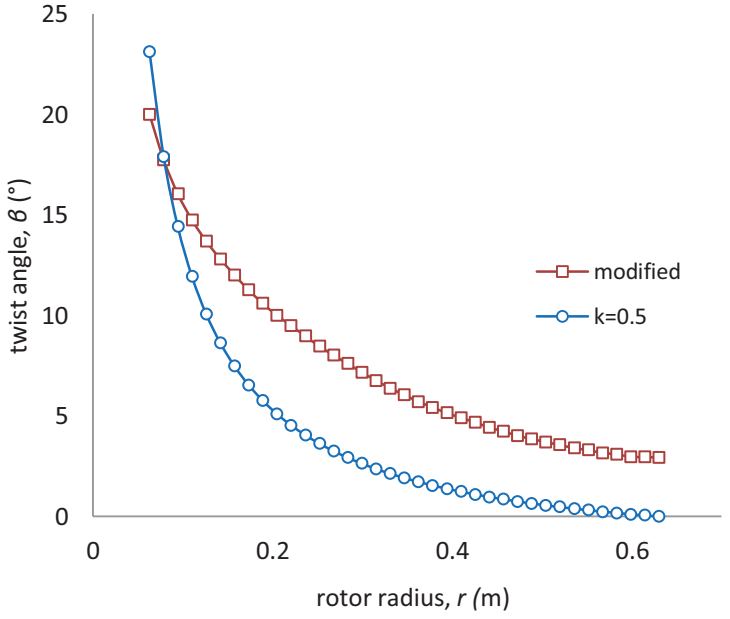

Fig. 5.10 Modified blade twist distribution compared with twist of zero lift line equation with $k = 0.5$

5.1.8 Rotor Solidity (σ)

Rotor solidity is given by:

$$\sigma = \text{ rotor area /rotor swept area } = (N_b \times \text{ area of a single blade})/(\pi R^2) \quad (5.7)$$

Based on the chord and twist distribution, the designed rotor's solidity, σ = 8.27% compared to the stock rotor's solidity of 8.42%. Rotor solidity is inversly proportional to tip speed ratio, λ [2]. The more slender the blade (lower σ), the higher the tip speed ratio. Slender rotors allow for the air to flow through without severely slowing it down like in the case of broader blades (higher σ). Blades with higher solidity form an obstruction to the airflow that causes the rotor speed to decrease [57]. With high rotor solidity, the flow diveges from its normal path and does not go through the rotor swept area decreasing the performance of the turbine. Higher tip speed increases rotor performance but at the cost of noise and complex and expensive blade design [2, 55]. The relationship between solidity and tip speed ratio is shown in equation 5.8 which is the simplified form of Betz theory focusing on wind turbine aerodynamics [58]. Rotor soility, σ and tip speed ratio, λ are inversily propotional showing an expontential relationship when the 2 are ploted against each other (figure 5.11).

$$\sigma = \frac{1}{C_L}\frac{16}{9}\left(\frac{1}{\lambda}\right)^2 \quad (5.8)$$

Rotor soildity is dependent on and influanced by:

1. number of blades – rotor solidity increases with increase in the number of blades and vis-vesa.
2. diameter of rotor – increasing the diameter decreases soildity as the blades become slender and vis-vesa.
3. chord distribution – determines the shape of the blade, whether it is slender or broad. A slender blade will have low soldity and a broad blade, higher soildity.
4. twist distribution – compared to a non twisted blade, a twisted blade will have lower solidity as less planform area is exposed to the wind provided both have same chord distribution and pitch angle (figure 5.12).

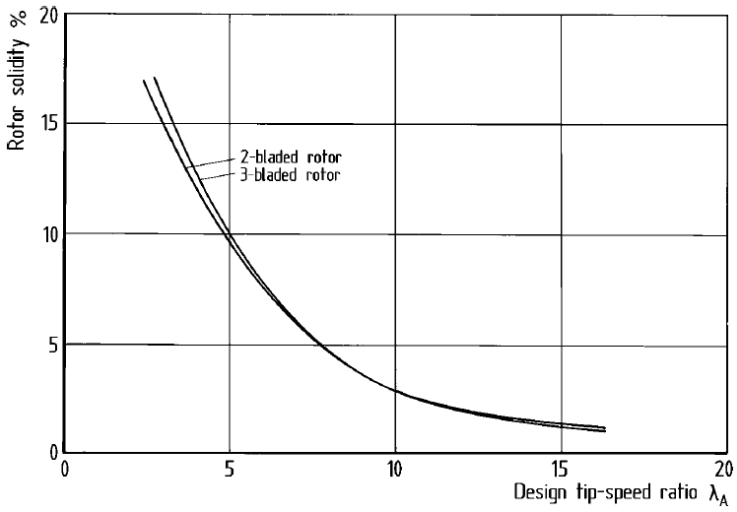

Fig. 5.11 Relationship between solidity and tip speed ratio is shown in the graph of rotor solidity vs. tip speed ratio for NACA 4415 airfoil with deign C_L=1.0 [2]

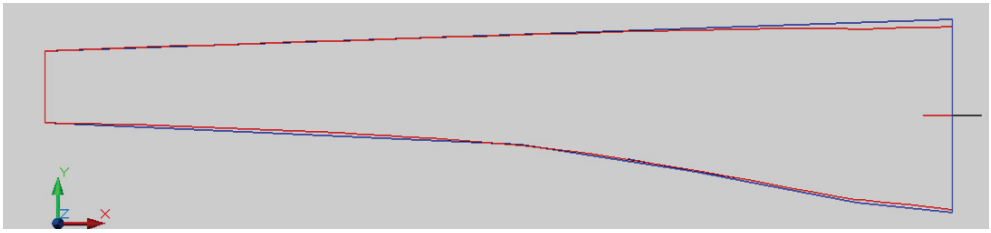

Fig. 5.12 Rotor solidity is less for a twisted blade (red) as compared to a non twisted blade (blue) having same chord distribution

In figure 5.13, comparison of rotor swept area and rotor area exposed to wind between the designed, 2-bladed rotor and stock, 3-bladed rotor is shown. Although apearing to be slender than the 2-bladed rotor, the 3-bladed stock rotor has 2% more soldity. The 2-bladed rotor has greater swept area as compared to the stock rotor and thus will extract more power from the wind.

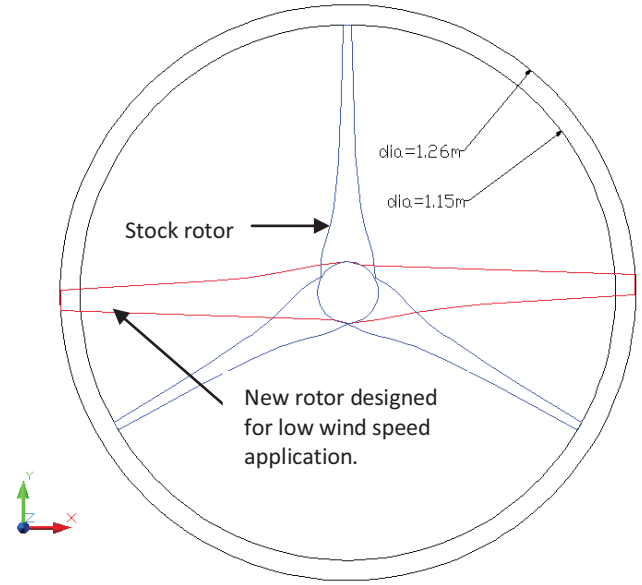

Fig. 5.13 Rotor swept area shown for the stock 3-bladed rotor compared to the designed 2-bladed rotor. Notice the difference between the slenderness of the blades

5.1.9 Rotor Specifications

The rotor specifications for the 2-bladed rotor are as follows:

Diameter = 1.26m

Rotor radius = 0.63m

Effective rotor radius = 0.565m

Hub diameter = 0.13m

Twist angle = 20° – 3° = 17°

Root pitch angle = 20°

Tip pitch angle = 3°

Rotor solidity = 8.27%

Airfoil section = AF300

Design freestream velocity = 5m/s

Design rpm = 500rpm

Tip speed ratio = 6.6

Figures 5.14 – 5.18 show the AutoCad schemetics of the designed 2-bladed rotor. With Auto CAD the 3-D visualization of the blade shape with the twist distribution was made possible with changes to the blade geometry a mouse click away. AutoCad also helped in the manufacturing

process of the blades which will be discussed later in the section. Figure 5.14 shows the twist distribution of the blade with 20° pitch angle at the root and 3° pitch angle at the tip. There are in total 40 airfoil sections that are evenly distributed along the span of the blade. Each airfoil section from root to tip is pitched accordingly to the twist distribution. The pitching ponit of rotation is not limited to a specific point along the chord line, but can be taken anywhere along it. Location of rotation of pitch for each airfoil was chosen at the leading edge but later shifted 30% back from the leading edge to the trailing edge for a even more structually sound blade as the pitching ponit will be more or less closer to the center of mass of each section of the blade.

Figure 5.15 shows the chord distribution and basic dimensions of the blades. The blade is twisted compared to the untwisted blade in figure 5.5. With twist, more frontal area is exposed near the root (front elevation in figure 5.15) as compare to figure 5.5 (edgewise view).

Figure 5.16 shows the full rotor blades plan and elevation. The light blue lines going along the span of the blade traces out the peak point on the top and bottom surface of the blades parallel to the rotor plane of rotation. The inner light blue line (in the middle) traces the peack ponits of each airfoil section on the upper surface of the blade while the light blue lines near the leading edge trace out the peak ponits for the lower surface. These traces are very important as they show the outter extremes of the blades as viewed from the front (side elevation). This will aid in the manufacture of the blades.

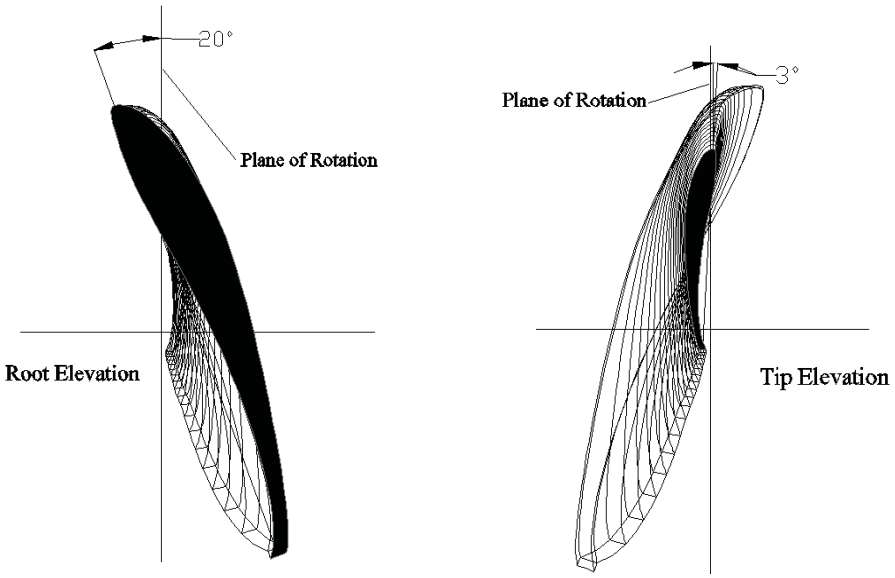

Fig. 5.14 Twisted blade showing the root and tip profile and the pitch angle between the chord and plane of rotation

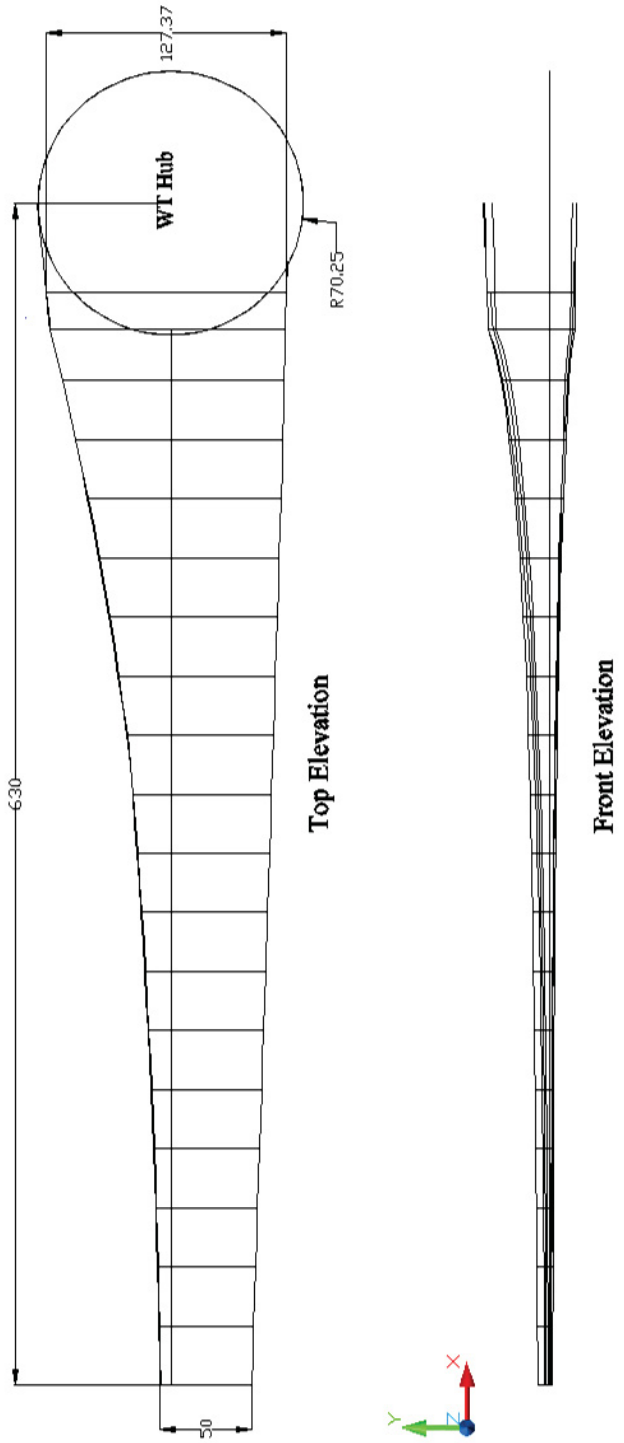

Fig. 5.15 Top and front elevation of rotor blade showing the chord and twist distribution (dimensions in mm)

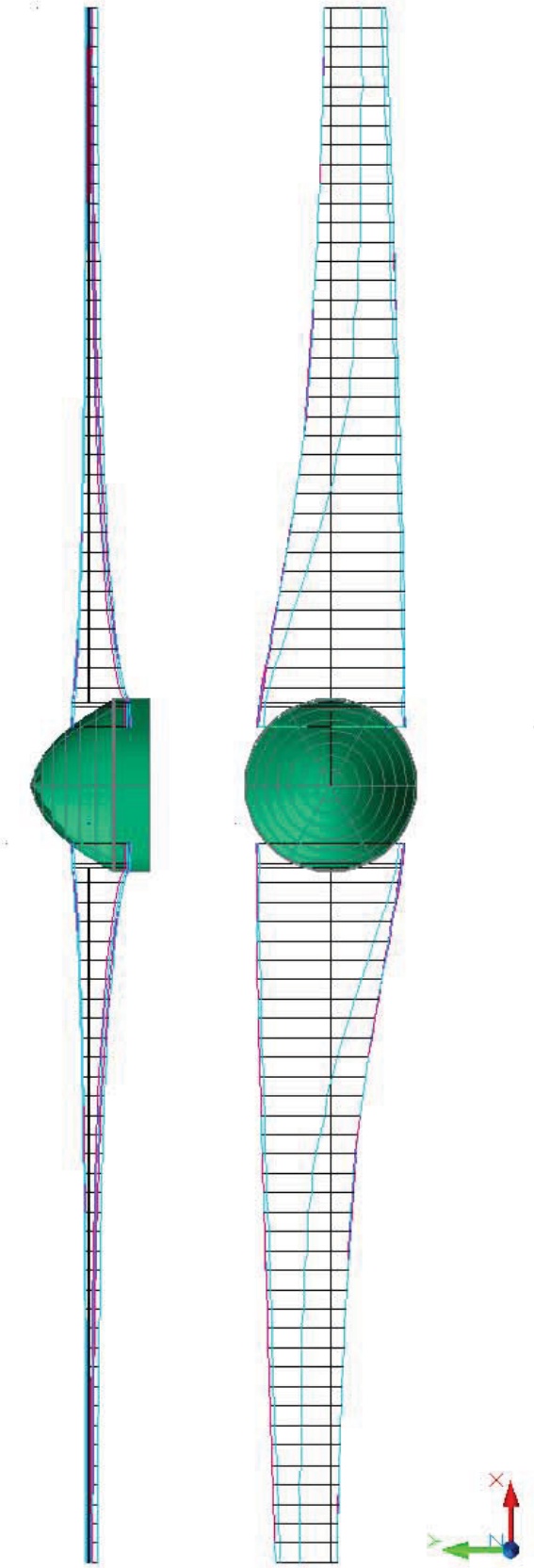

Fig. 5.16 Side and top elevation of rotor blades

5.2 Fabrication of rotor blades with centrifugal pitch control

5.2.1 Fabrication phase

The blades were fabricated from Dakua Salusalu wood as it is lightweight and has good workability property compared to other locally available woods. Table 5.1 shows a selection of local wood suitable for consideration for the blade material together with their mechanical strength properties and density.

Table 5.1 Physical and mechanical properties of local woods of Fiji [59]

Wood type	Air dry density (kg/m^3)	Mechanical strength (S1 – S7 order of decreasing strength)
Dakua Salusalu	440	S7 green, SD7 (seasoned)
Dukua Makadre (Fiji Kauri)	540	S5 green, SD5 (seasoned)
Damanu	610	S4 green, SD4 (seasoned)
Kauvula (fibrous)	480	S5 green, SD6 (seasoned)
Mahogany (fibrous)	570	S6 green, SD7 (seasoned)

The blade taper, twist and airfoil profile were all carved out from a single block of wood with the aid of airfoil tampletes spread across the radial distance of each blade. Dimensions of the solid block of wood was obtained from the top and front elevations of the blade provided in AutoCad as shown in figure 5.17, outlined in red. The block thus measured (583 x 127.4 x 47)mm. The elevations provided in figure 5.17 were printed on transparacy paper with a 1:1scale and pasted on the block. From the 2-D elevations, curving of a 3-D blade was made possible. The extra wood was sawed off outside of the dimensions of the blade shape. The shape formed had the resemblance of a tapered blade only. To add twist to the blades, templates of airfoil sections along the span of the blade had to made and used as guide during the curving of the airfoil profile and twist onto the preformed wooden block (figure 5.18). Twenty four templates spanned the length of the blade for accurate curving of the blade. The second blade was shaped following the same procedure. Figure 5.18 shows the roughly completed blade through the aid of the templates. At this point in the manufacturing process, taper and twist distribution have been carved into the workpiece.

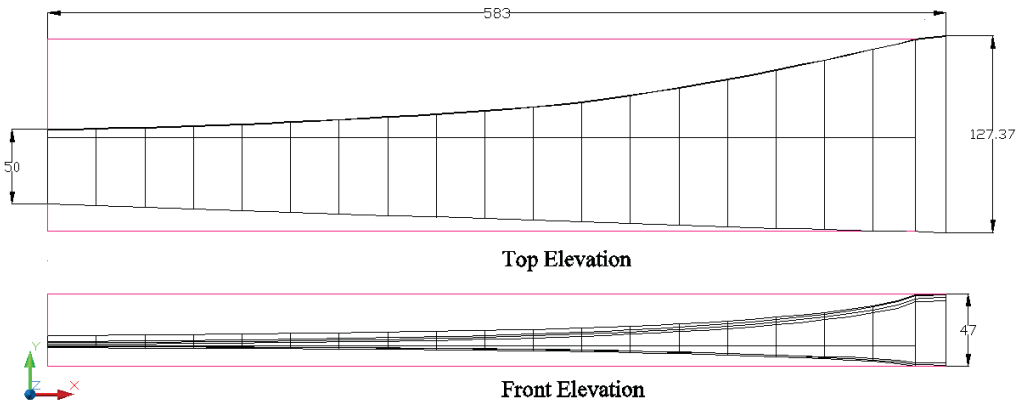

Fig. 5.17 Outline of dimensions on wooden block for blade manufacture

The finished blades were smoothed and balanced on a pivot (figure 5.20) so as to have the center of gravity of each blade at an equal distance from the pivot point (center of blade rotation). Once balanced the blades were fibre coated for extra strength. The blades were balanced for a second time after the fibreglass was smoothed out.

The finished rotor blades are shown fitted to the Air X marine wind turbine in figure 5.21. As part of safeguarding the rotor blades in strong wind conditions passive pitch control was introduced to the turbine with the aid of centrifugal pitch control.

Fig. 5.18 Templates being used to carve the airfoil profile together with the twist distribution onto the bottom side of the blade

Fig. 5.19 Roughly completed blade with the twist clearly visible on the trailing edge of the blade

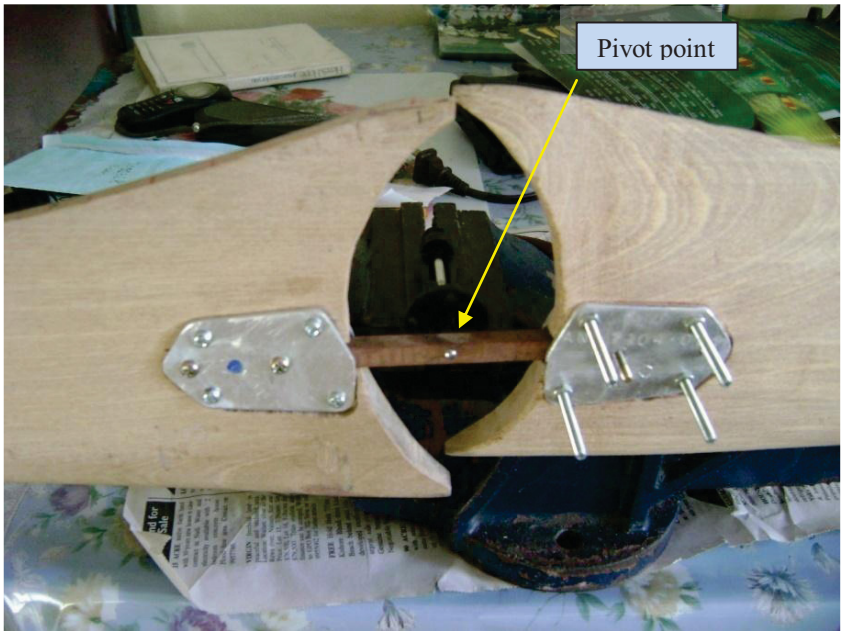

Fig. 5.20 Balancing of the blades

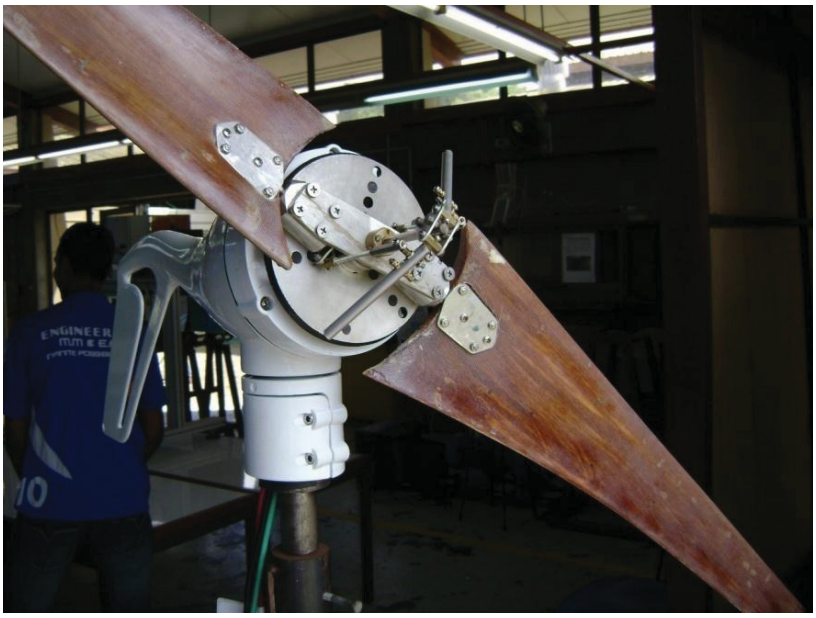

Fig. 5.21 Fabricated fiber coated wooden 2-bladed rotor fitted on an *Air X Marine* 400Watts wind turbine

5.2.2 Centrifugal pitch control of rotor blades

A centrifugal pitching mechanism was incorporated as a means of governing the rpm and thus power output from the rotor, but most importantly to safely brake the blades during strong wind conditions. Pitching is accomplished by feathering the rotors, that is, increasing the pitch angle of the blades. This action decreases the blade planeform area that slows down the rotor and decreases the thrust forces on the blades at the same time. The mechanism consists of a spinning governer that actuates outwards and inwards depending on the rpm of the turbine rotor. The govner masses connect to links that are connected to the blade roots via hinges. During actuation of the governor masses, the links pull and push on the blade root hinges, pitching the blades. The pitch control mechanism is shown below in figures 5.22 – 5.25. The mechanism works in the range of 600 – 1000rpm to regulate rpm of the rotor blades. During full 'throw' of the governor arms at 1000rpm+, blade pitch increases by 50° (max). If the set pitch angle is 20° then during instantanous braking the blade pitch = 20° + 50° = 70° which is more than enough to completely stop the blades from rotating. Figure 5.26 shows the graph of pitch angle against governor rpm. It shows an exponenital increase in β whereby it increases abruptly from 881 rpm and is fully braked at 1020 rpm which takes a fraction of a section to do due to the ripid dispalcement of the governor masses from the middle to the outermost poistions on the governor arms to increase the centrifugal force to instantly brake the rotors.

During rpm regulation, rpm of rotor will cycle to the set rpm at which the system should be operating. The cycle is sinusoidal beacause of the balancing effect of the masses and governor arm retainer springs which pull on the governor arms to a closed position after the rotor has slowed down through pitch regulation.

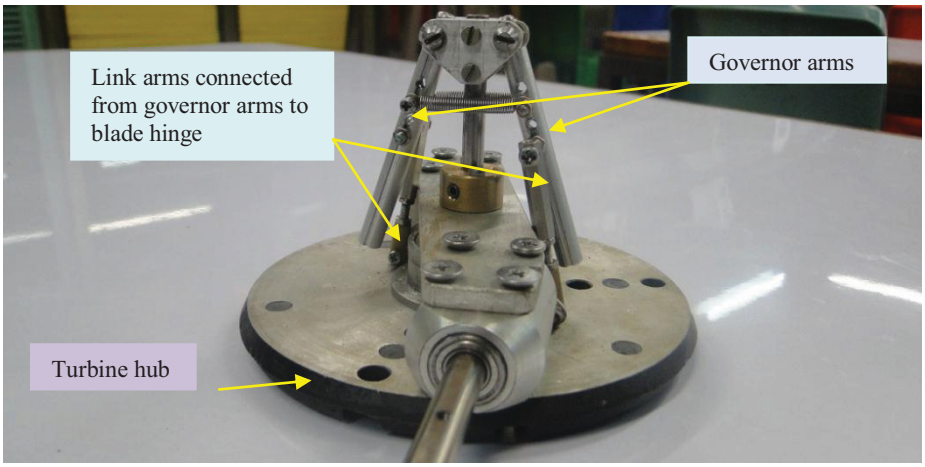

Fig. 5.22 Pitch control mechanism fitted onto the hub with details of the governor arms and linkage shown

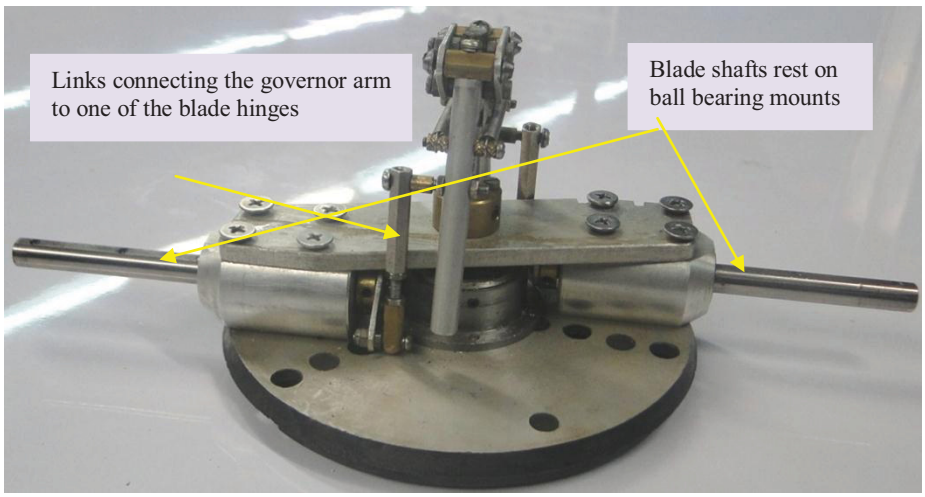

Fig. 5.23 Details of the linkage and blade mounting

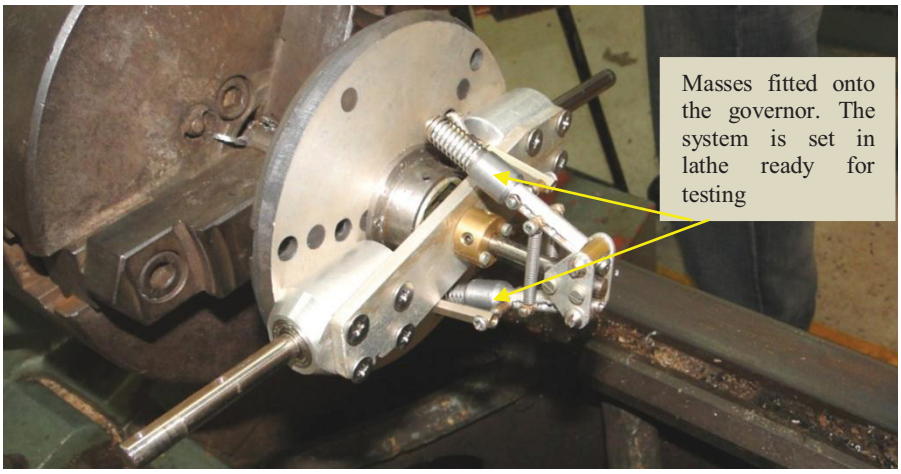

Fig. 5.24 Pitch control mechanism setup for testing in lathe machine with variable speed control

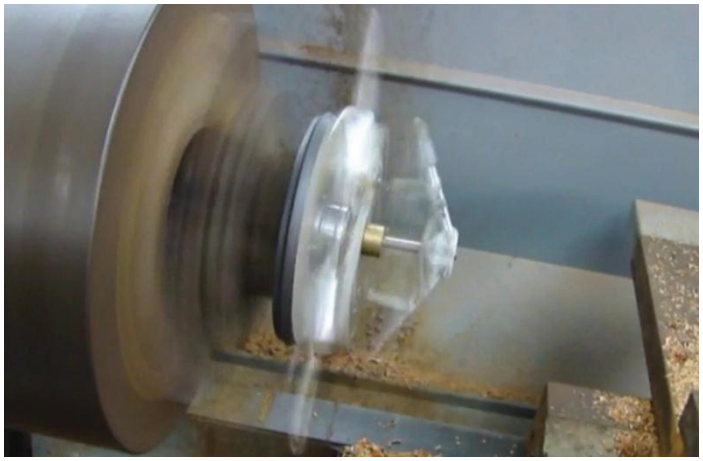

Fig. 5.25 Governor arms actuated at 883rpm. Partial engagement occurs at 635rpm, whereas full engagement occurs at 1000+rpm

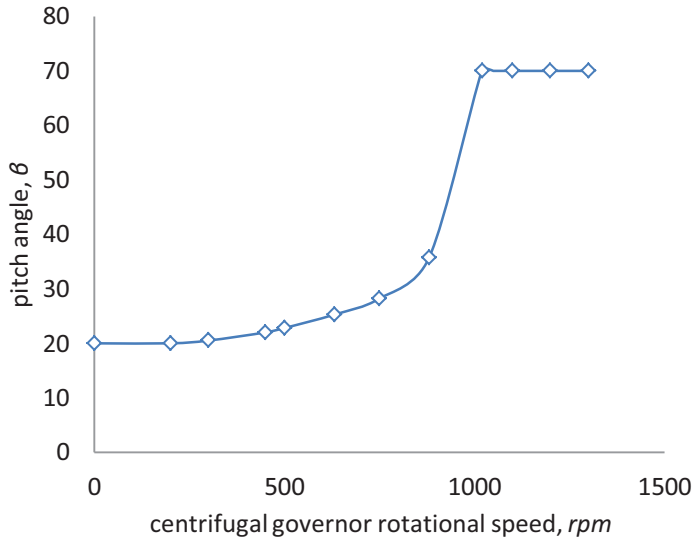

Fig. 5.26 Graph of pitch angle, β vs. centrifugal governor rotational speed with $\beta = 20°$

Chapter 6 Performance testing of Air X marine wind turbine with installed 2-bladed rotor blades designed for low wind speed application

6.1 Test equipments associated with the field testing of the Air X marine wind turbine

6.1.1 The Air X marine wind turbine

The Air X marine wind turbine was chosen for the research project in the evaluation of performance of the rotor blades. The Air X is a 3-bladed, 400 Watts micro wind turbine system that develops maximum power at 12.5m/s wind speed. The turbine has been desiged to operate in the harsh marine environment and survive wind speeds up to 49m/s (177km/h). The turbine employs no gearbox in between the rotors and generator but is directily coupled to the generator via 2 ball bearings and enclosed in a one piece alumunium molded body making it robust and simple in design.

The Air X has been designed to charge lead-acid based battery cell banks and only charge 12V, 25 – 25000 Ah systems. The inbuilt microprocessor based electronic circuit of the Air X has a charge controller that supplies AC power already rectified to D.C to the battery with active sensing of the battery voltage. To safegaurd against damaging wind speeds, the turbine brakes the rotors to a stop by shorting the syncrohnous permanent magnet generator. The PM generator is unique in the sense that it comes bundled with 2 gagues of coil windings that supply power at both low and high wind speeds efficiently. The turbine's microprocessor also tracks the peak power of the system enusring optimum power output from the turbine. The turbine 'trickle' charges the battery banks so as to not over charge it and monitors the battery voltage momentarily during charging within a fraction of second. Figure 6.1 below shows the basic components of the Air X marine wind turbine in an exploded view.

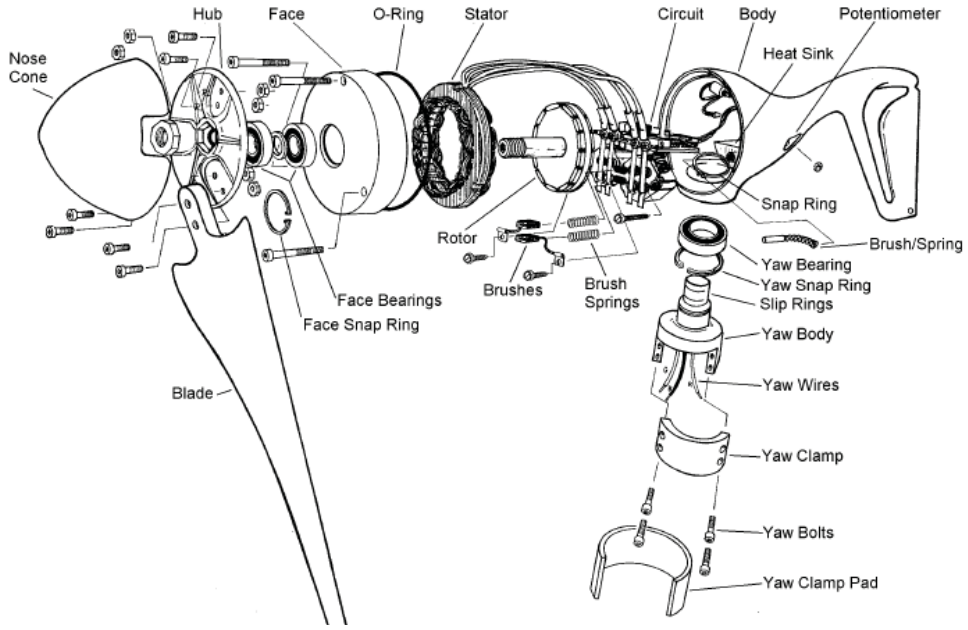

Fig. 6.1 Exploded view of the Air X marine wind turbine [60]

6.1.2 Air X marine technical specification [61]

Rotor Diameter	1.17 m
Weight	5.85 kg
Start-Up Wind Speed	3.58 m/s
Voltage	12 VDC
Current rating	33.3Amps
Rated Power	400 watts at 12.5 m/s
Turbine Controller	Microprocessor-based smart internal regulator with peak power tracking
Body	Cast aluminum (Marine is powder coated for corrosion protection)
Blades	3-Carbon fiber composite (stock rotor)
Over speed Protection	Electronic torque control
Kilowatt Hours per Month	38 kWh/mo at 5.4 m/s
Stall mode	15.6m/s
Shutdown wind speed	22m/s
Survival Wind Speed	49.2 m/s

6.1.3 Battery charging by Air X marine wind turbine

A 12V Air X wind turbine system was purchased for the project. The Air X wind turbine is specifically restricted to battery charging only by its electronic controller. Charging of a 12V deep cycle commences when the battery voltage falls below 12.75V and stops at 14.1V. A load was necessary to keep draining power from the battery thus ensuring that the turbine keeps charging the batteries and does not go into shutdown mode. If battery voltage drops below 8V, the turbine's controller will not be able to sense the batterys voltage and will not charge the battery. In this case a charge controller is connected in between the battery bank and load. The charge controller will cut off the load from the battery bank when the voltage of the battery bank falls below the critical voltage value as specified on the charge controller. The charge controllers used in the project cut the load at 11.80 volts.

6.1.4 Active braking of Air X marine wind turbine

The onboard electronic circuit of the Air X wind turbine uses 20mA from the batteries and monitors the charging of the battery voltage through a feedback system. When the turbine senses a battery potential of 14.1V, the turbine stops charging and goes into regulation mode. In regulation mode the turbine generator is disconnected from the positve and negative leads connected to the battery bank and braked through short circuiting it. If the turbine has an open circuit, that is it is not connected to any load, the turbine will go into regulation mode once it senses an open circuit voltage of 20V on its positive and negative wire leads to safeguard the bearings and generator.

The Air X wind turbine will go into stall mode when the turbine senses a wind speed of 15.6m/s and above. When this occurs, the turbine will slow down to 500 – 700rpm and trickle charge the battery bank. Normal charging will resume when the wind speed falls to 14m/s. During strong wind conditions the turbine enters regulation mode and completely shut down for 5 minutes if wind speeds exceed 22 m/s before charging commences again. At this time the rotors will stop to a stand still by using the batteries power to create back emf to brake the generator.

6.2 Wind tubine performance evaluation setup

The wind turbine was stationed at USP's marine campus on an empty piece of land facing the ocean. The particular place was chosen based on good strong turbulence free wind conditions from the sea breeze and due to an aveage radius clearance of 40m of any topologies. The site is shown in figure 6.2 below. The wind turbine was situated 8.22 meters above sea level on a guyed tubular pole. An A101M anemometer was situated 1m below the turbine hub height and extended 1m outwards so as to not pose as an obstruction to the wind turbine.

Fig. 6.2 Location of wind turbine for field test for turbine performance evaluation [**62**]

Figures 6.3 – 6.6 show the field setup for the turbine performance assessment. In figure 6.3 an overview of the whole set is shown with the 8.22m pole guyed in with 4 cable wires to support the final position of the Air X wind turbine and anemometer. Figure 6.4 shows the close-up view of the Air X wind turbine and the A101M 3-cup anemometer fitted to the pole. The anemometer is fitted at a height of 7m (1m below turbine hub center) and extended 1m away from the pole to eliminate any disturbances to the flow to the rotor. In figure 6.5 a closeup view of the monitoring station with the setup for data collection is shown together with battery bank and charge controlled load discharge to ensure continual charging by the wind turbine. The battery bank

consists of 2 dry cell deep cycle 12V, 100Ah batteries connected in parallel to increase the load to 200Ah. The discharge load (figure 6.6) consists of 8 halogen car head lamps rated at 90W each. In total, the lamps would drain 720W from the battery bank untill the battery potential of the bank falls below 11.3V. Four charge controllers of 15A (180W) each were coupled with 2 lamps at a time to complete the load circuit. The charge controllers ensured that the battery bank would be loaded successivily with respect to the amount of charging by the wind turbine. In the case of strong wind, and thus fast charging, 4 to 6 lamps would lightup depending on the potential created on the battery terminals. The data logging consisted of a CR1000 data logger, 12V isolated battery supply and circuit to log turbine voltage and current. The data logger setup was enclosed in a weather sealed container to protect the logger from moisture and rain.

Fig. 6.3 Setup for testing of the Air X wind turbine at the Marine campus

Fig. 6.4 Close-up view of the Air X turbine with the new 2-bladed rotor and anemometer setup

Fig. 6.5 Monitoring station consisting of battery bank, electrical loading and data logging equipment

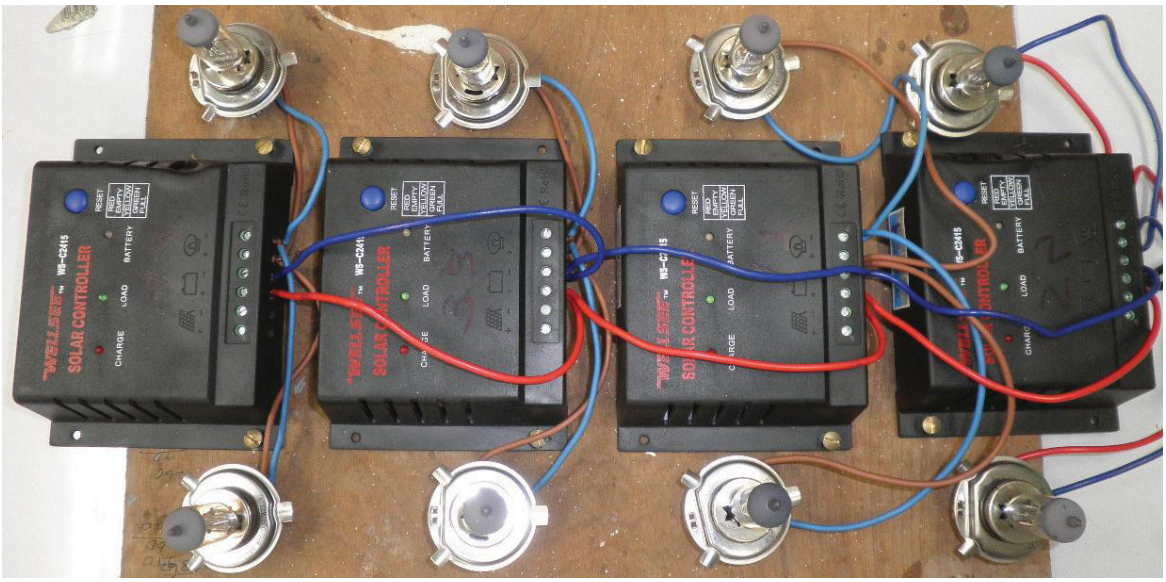

Fig. 6.6 Electrical load consists of eight 90W halogen lamps connected to battery bank via charge controllers

6.3 Testing of equipment

6.3.1 Testing of wind turbine

Testing of the wind turbine to ensure its functionality was done in accordance with the Air X user's manual [61]. The turbine leads were connected to a 12 V DC battery. Blinking of the red L.E.D beneath the turbine indicates that feedback from the battery has been received. The turbine rotor shaft was spun with a power handdrill. As the speed of the drill was increased, the L.E.D lighted up and torque was being felt on the drill indicating that the turbine is charging the battery. A techometer was used to measure the rpm at which power is first produced. This occurred around 500 rpm.

6.3.2 Testing of A101M 3-cup anemometer

The A101M 3-cup anemometer was calibrated in reference to a pitot-static tube. An open type blower wind tunnel generated a constant freestream velocity of 7m/s in the test section. The anemometer was positioned near the open test section and then far away from it. The pitot-static tube was positioned in the same locations and the results of the anemometer and pitot-static tube were compared. The graph below shows the comparison between readings obtained by the pitot-static tube and anemometer at the 2 different postions from the test section. It is seen that correlation between the 2 at both freestream velocities is quite good and no calibration was

needed for the anemometer. The small discrepancies in readings were due to fluctuating readouts from the instruments as shown in table 6.1.

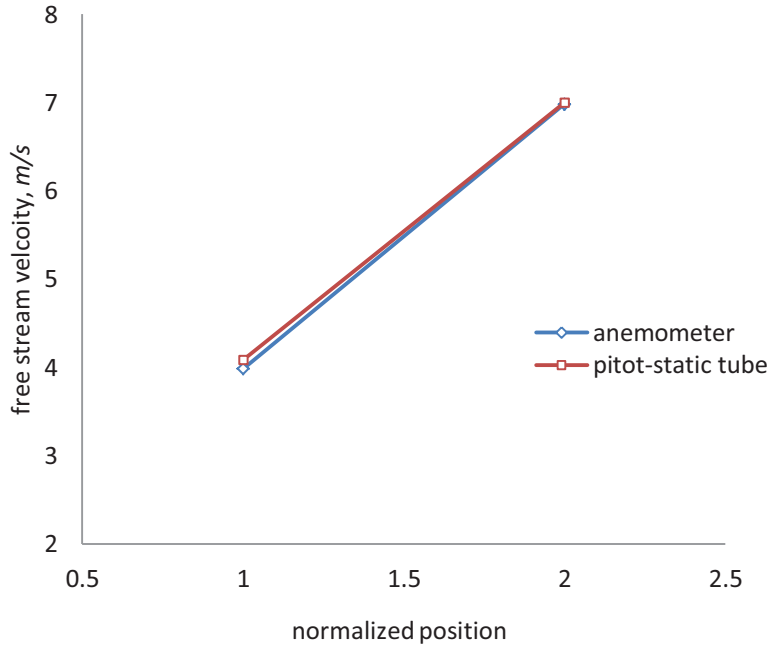

Fig. 6.7 Graph of freestream velocity, V_∞ vs. position

Table 6.1 Trial readings of freestream velocities from anemometer and pitot-static tube at 2 different positions

Temperature = 29°C	Anemometer readings (m/s)	Pitot-static readings (m/s)	Anemometer readings (m/s)	Pitot-static readings (m/s)
	0.5m away from the test section		2m away from the test section	
	7.05	7.06	4.21	4.20
	6.75	7.01	3.91	4.06
	6.68	6.86	3.81	4.01
	6.95	6.94	4.21	4.12
	7.15	6.73	3.62	4.08
	6.95	7.31	4.11	4.03
	7.35	7.11	4.01	4.10
Average	**6.98**	**7.00**	**3.98**	**4.08**

Figures 6.8 – 6.9 show the setup of the A101M 3-cup anemometer and pitot-static tube positioned 0.5 meters from the test section. A digital micromanometer was used to measure dynamic pressure from the pitot from which the freestream velocity was calculated. For the anemometer, a digital readout provided the velocity that was connected to the data logger.

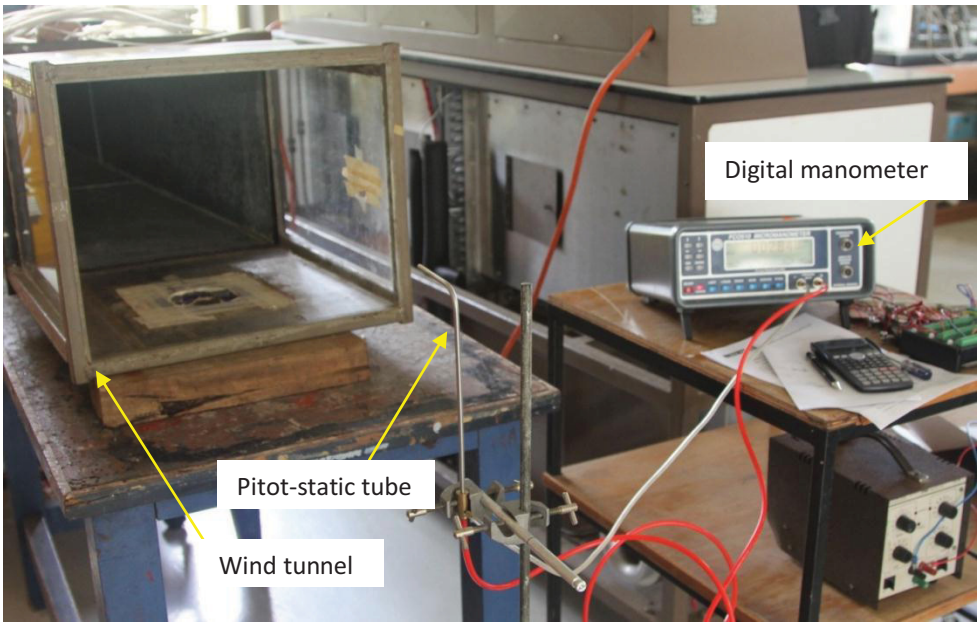

Fig. 6.8 Setup for pressure measurements from pitot-static tube

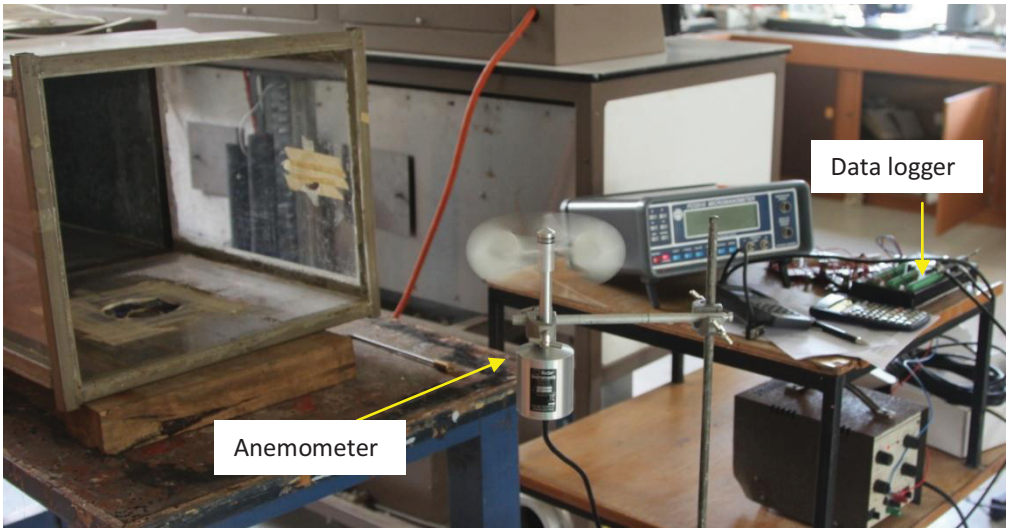

Fig. 6.9 Setup for anemometer for direct velocity measurement

6.3.3 Bench testing of data logger equipment

The data logger was setup to record the current and voltage of a standard load generated from a DC electric motor. The digital readout display unit of the data logger provided the current and voltage values which were being updated every second. These were compared with multimeter readings connected to the electric motor as shown in figure 6.10. Figure 6.11 shows the bench test of the actual turbine setup. The turbine was spun by an electric drill to generate the power to charge the battery bank. Current and voltage values were recorded by the data logger and the

multimeters. In both cases there was good agreement between the multimeter readings and data logger readings.

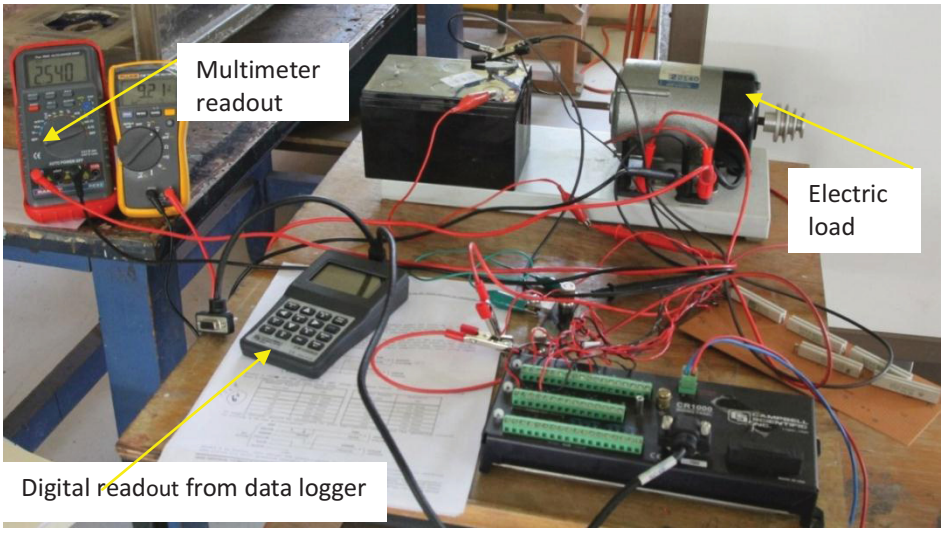

Fig. 6.10 Bench testing a small electric load

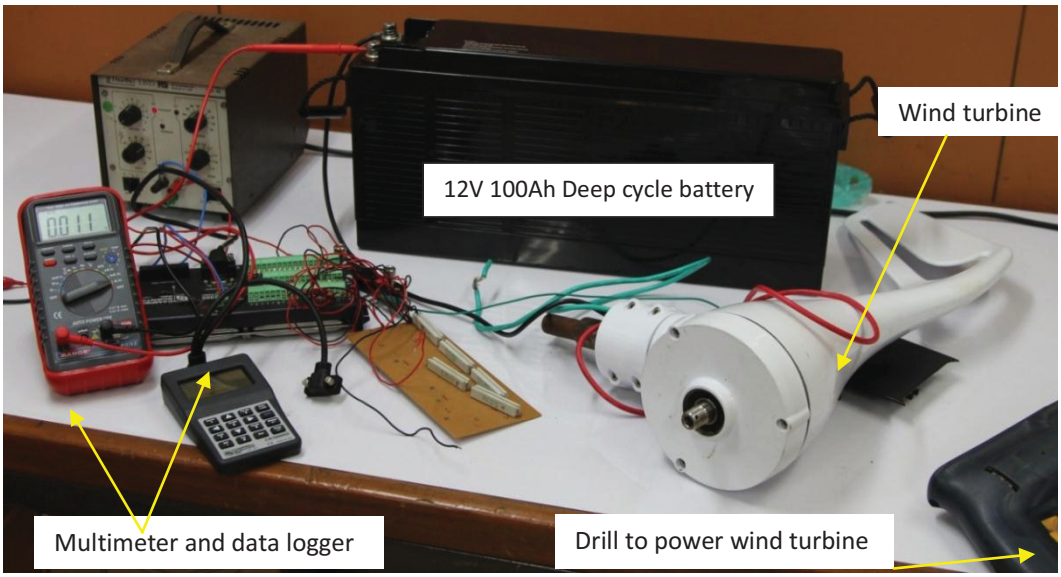

Fig. 6.11 Bench testing the actual turbine setup

6.3.4 Setting the intial pitch angle of rotor blades

Pitch angle of each rotor blade was set to 20° at the hub. A vernier protector was used to accuratily set the angle of each blade by setting the blade shaft to the particular pitch angle (figure 6.12). At 20° pitch angle, the root portion of the blade is at 20° and the tip portion is at 3°. Pitch was varied during the testing of Air X wind turbine. With the different pitch settings, the turbine's performance and startup speed and cut-in wind speed was monitored.

Fig. 6.12 A vernier protector being used to set the pitch angle, β at the root on each blade shaft

6.3.5 Electric circuit of Air X wind turbine

The figure below shows 6V, 100Ah batteries connected in series to double the total voltage to 12 volts and than connected in parallel to increase loading on the turbine to 200Ah which will be data logged in the form of voltage and current. To make sure the battery bank poses as a consistant load on the turbine, the battery bank must be loaded to constantly drain power from the battery bank. The load on the battery bank must be enough to equal the charging rate of the generator such that charging rate of the generator does not fluctuate too much during periods of constant wind speed. When there is no wind, the turbine will not be charging the battery banks, in this case the load on the battery will drain all power from it if charging does not comence before the discharge period. Due to the turbine's design of internal electronic circuit, it will not charge when the battery potential falls below 8V. Therefore a charge controller needs to be placed between the load and battery bank to limit the amount of power being drained from the battery at all times by cutting off the load when the battery voltage falls down to a certain value greater than 8V.

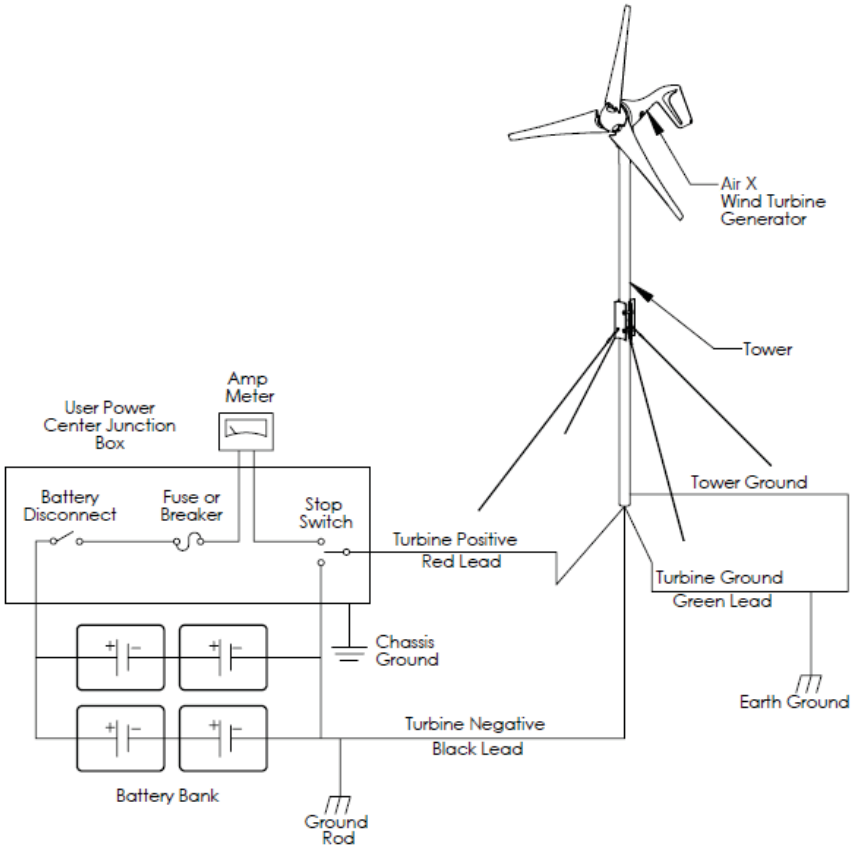

Fig. 6.13 Typical setup for load connection to the wind turbine [61]

6.3.6 Battery bank

Two 12V, 100Ah battery were employed to act as load to the wind turbine. The battery bank consisted of these batteries connected in parallel to increase load to 200Ah.

6.3.7 D.C load on the battery bank

As mentained above a load needs to be connected to the battery bank to constantly drain power out of the bank ensuring the turbine is continuously generating power from the wind that is being data logged. Car head lamp halogen, high wattage bulbs were chosen as DC loads. Eight filiment lamps were used for the load. Four sets of 2 lamps connected in parallel were connected to battery bank via 4 charge controllers of 15A each. Each lamp is rated at 90W, therefore a total of 720W of power is drawn from the battery bank. The four 15A charge controllers ensures that the load (lamps) are cut from the battery bank when the battery voltage falls to 11.3V.

6.3.8 Setup for datalogging

Turbine voltage, current and wind speed were logged to evaluate the wind turbine's peformance. Wind speed was measured with a A101M 3-cup anemometer. From wind speed, wind power was calculated via:

$$P_{wind} = \frac{1}{2}\rho A V_{\infty}^{3} \quad (6.1)$$

Power extracted from wind turbine = VI (voltage x current). Where $I = I_{out}$ (figure 6.14) which was measured by measuring voltage across a low value resistor. Voltage = V_{out} which was the summation of voltages measured across R_1 to R_5. Resistors, R_1 to R_5 were placed to lower the value of votlage being logged as the data logger can measure maximum of 5 volts. These formulae were preprogramed in the data logger so that the generated values of voltage and currernt are logged. The C++ coding is provided in appendix 3 The data logger logged the 3 variables in a single line every 10 second, sampling the data every 1 second and averaging the 1 second data readings after 10sec interval.

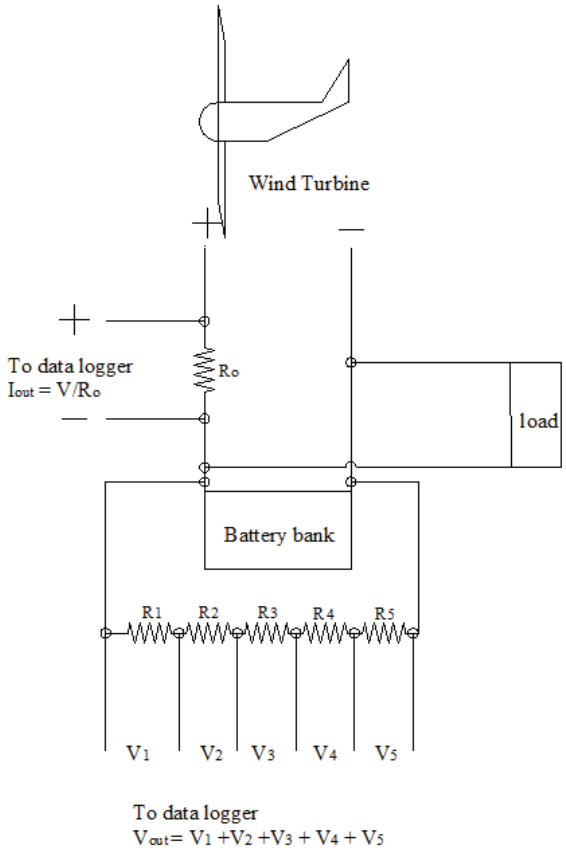

Fig. 6.14 Circuit for obtaining current and voltage of the generator

6.4 Results and discussion

Data logging of wind speed and turbine's voltage and current output was done at 3 different settings of the wind turbine's pitch angle of 15°, 18° and 20° to yield the turbine's optimum performance in the low wind speed conditions.

6.4.1 Wind monitoring statistics

Twenty four hour wind speed distribution data vs. time graphs were plotted from the duration of testing of the wind turbine at the different 3 blade pitch angle settings. Figures 3.1 – 3.4 provided in appendix 3 show the wind speed distribution for a 24 hour period. Results such as the mean and maximum wind speed and mean power density were calculated and are given in tables A3.1 – A3.4 in appendix 3 corresponding to graphs in figures A3.1 – A3.4 respectively.

6.4.2 Performance of Air X wind turbine with 2-bladed rotor designed for low wind speed application

During data logging, each entry or line of data recorded was a 10 second average of 10 data points taken at 1Hz sample rate (1 reading every second). The data logger simultaneously recorded wind speed, current and voltage at 1Hz sample rate and recorded the 10 second average of the 3 entries. From the plots of wind turbine power vs. wind speed, it was noticed that every particular wind speed produced a range of power values and not just one. This was primarily due to the difference in inertia of the rotor blades and the 3 cups of the anemometer and yaw response of the wind turbine during changes in wind direction. Secondarily it was due to the number of samples that were averaged.

6.4.3 Difference in rotational inertia of turbine rotor and anemometer cups

The anemometer cups are light weight and spin almost frictionless on ball bearings giving the cups a very low inertia producing very fast response to variation in wind speed. For the wind turbine, initial start up is slow due to the high inertia of the blades compared to the cups the anemometer and due to friction in the rotor bearings. The high inertia of the turbine rotor blades slows down the acceleration and deceleration response rates with respect to change in wind speed. Therefore when the wind speed falls, say for example from 8m/s to 6m/s, the anemometer would show a decrease in wind speed almost instantly while the turbine continues to produce near optimum power that it was producing at 8m/s due to the high inertia. The opposite scenario

occurs during start up. Rapidly fluctuating wind conditions will produce a lot of dispersal in power output at the given wind velocities.

6.4.4 Turbine yaw

The response time for the turbine rotor plane to constantly maintain a perpendicular alignment with the wind direction is crucial in capturing maximum energy from the wind. During times when wind direction is changing, the power output from the wind turbine suffers due to time lag as it constantly tries to face into wind. During these times, the turbine's power quality will decrease together with its performance. The effects of yaw is noticed when data which are captured in periods where wind maintains a constant direction and when the direction is fluctuating are compared.

6.4.5 Sample rate and averaged data entry

The true nature of the behavior of the wind and turbine, i.e. wind speed and power respectively must be measured by the data logger and the necessary instruments. In order to capture the wind speed and power from the wind turbine, the sample rate must be high enough compared to the rate of change of the variables being measured. The data being measured and stored must be equal to the sample rate for 'live' capture of data, rather than the sample data being averaged over a period of time. Data stored that has been averaged will always produce lower values of the variables that are being measured and will show a lesser magnitude of variables than there really is. Using average data values to evaluate the performance of the wind turbine produces a marginal decrease in performance than what it really is in reality.

6.4.6 Wind turbine power

Figures 6.15 – 6.17 shows Air X's power variation vs. wind speed for 15°, 18° and 20° respectively. The power variation graphs show scatter plots of power where in reference to individual wind speeds, it has a range of values. This was due to the effects of rotational inertial differences between the turbine rotor and cups of the anemometer and yaw response of turbine to the change of wind direction. The power variation graphs show that Air X started producing power at a cut-in wind speed of 2.98, 2.34 and 2.38m/s for β = 15°, 18° and 20° respectively based on instantaneous 10sec averaged wind speed data. The results of cut-in wind speed are presented in table 6.2 where the cut-in wind speed, based on average wind speeds corrosponding

to the minimum power produced, was calculated (averaged cut-in wind speed). The averaged value of cut-in wind speed gives a true indication of turbine's minimum wind speed at which it will start producing electrical power. The turbine will only be seen to operate at the instantaneous cut-in wind speed only when it has first started off at the averaged cut-in wind speed and provided that it has gained enough rotational inertia, at which point even if the wind falls below the rated cut-in wind speed, the turbine will still be producing electrical power. Minimum instantaneous and averaged cut-in wind speeds were produced by the rotors at $\beta = 18°$ of 2.34 and 3.24m/s respectivily.

Table 6.2 Cut-in wind speed for Air X with 2-bladed rotor designed for low wind speed application

Pitch angle setting (°)	Instantaneous cut-in wind speed (m/s)	Averaged cut-in wind speed based on minimum power output (m/s)
15	2.98	3.46
18	2.34	3.24
20	2.38	3.33

Air X wind turbine has the lowest cut-in wind speed at 18° pitch angle of 3.24m/s. The cut-in wind speed is analogous to the start up wind speed. The startup wind speed is the speed at which the rotor starts rotating and not produce any power while the cut-in wind speed is the minimum speed at which it starts producing power. Air X has intelligence built into its control circuit that switches 'on' the generator only when the rotor reaches 500rpm and above. Below 500rpm, the rotor is free to rotate and is able to start up easily at lower start up wind speeds without requiring much torque during start up even though it is subject to resistive loading and rotational inertia of the rotor.

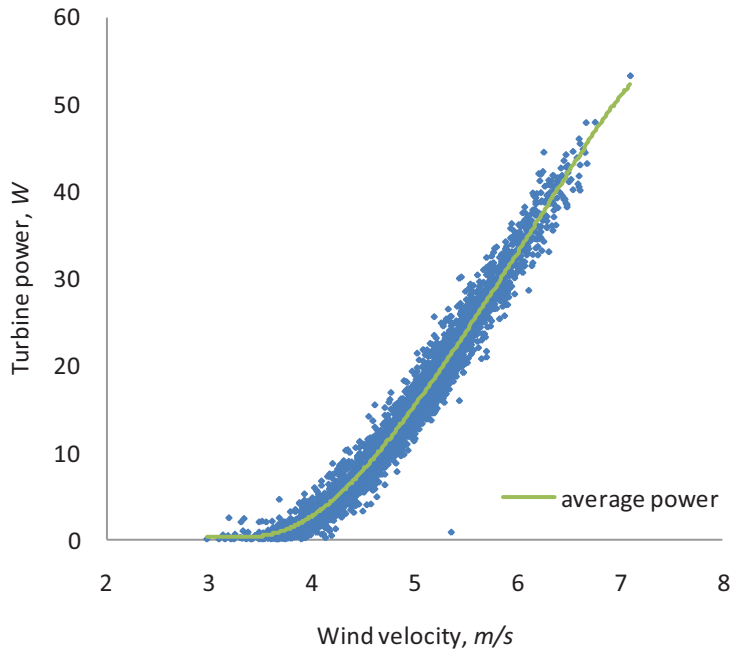

Fig. 6.15 Wind turbine power variation vs. wind speed for 15° pitch angle

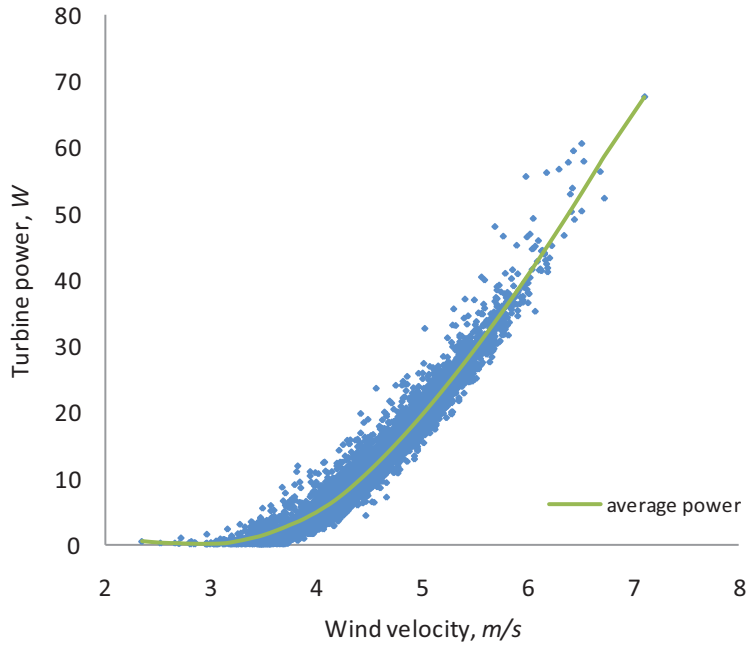

Fig. 6.16 Wind turbine power variation vs. wind speed for 18° pitch angle

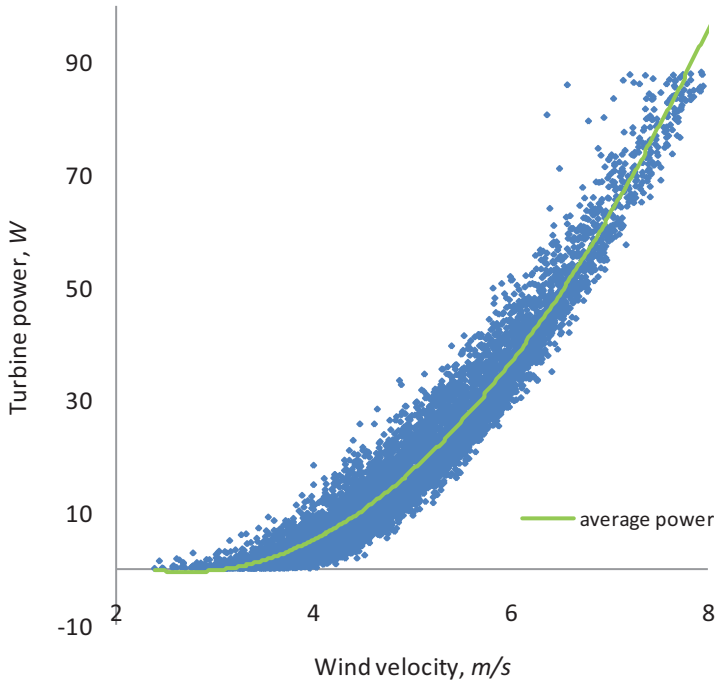

Fig. 6.17 Wind turbine power variation vs. wind speed for 20° pitch angle

6.4.7 Average power variation at different pitch angles

Average power variation was obtained from the scatter plots of power variation at different pitch angle setting and collectively plotted together against wind speed to see the effect of pitch angle, β on the power quality of Air X wind turbine. Average power variation of Air X with stock 3-bladed rotor was also compared with the average power variation of the 2-bladed rotor (figure 6.18). The graph shows that maximum power was produced by the 2-bladed configuration at β = 18° followed by 20° and then 15° pitch angles. The Air X wind turbine produced similar power at β = 18° and 20° in the wind speed range of 3-4.4 m/s. As wind speed increased beyond 4.4m/s, the rotor set to β = 18° produced the most power in comparisn to pitch settings of 15° and 20° within the whole wind speed range set for the turbine (3-7m/s).

A sound conclusion depends on the turbine's performance, C_P to evaluate which rotor configuration is better. With 8.62% longer blades, the 2-bladed rotor produced more power at all the 3 pitch angles compared with the stock rotor. At the optimum pitch, β = 18°, the 2-bladed rotor produced more than double the power than the stock rotor (table 6.3). The power output of the stock rotor coincided with only 15° pitch setting of the 2-bladed rotor upto 4m/s wind speed.

Table 6.3 below shows the power generated at incremental wind speeds of 0.5m/s in the 3 – 6m/s range for 2-bladed and stock 3-bladed rotors. It was noticed that at every given wind speed, the 2-bladed rotor produced maximum power at β = 18°, followed by 20°, 15° and lastly the stock rotor.

Table 6.3 Comparison between turbine power output of 2-bladed rotor at the different pitch settings and stock 3-bladed rotor

Wind speed (m/s)	Turbine power at different pitch angles (W)			Turbine power with stock 3-blades (W)
	15°	18°	20°	
3	0.08	0.08	0.08	0.00
3.5	0.28	0.72	0.62	0.14
4	2.60	4.73	4.50	2.19
4.5	7.94	11.19	10.69	5.18
5	15.33	19.98	19.38	9.17
5.5	23.79	29.57	27.81	14.35
6	33.18	40.67	38.28	21.19

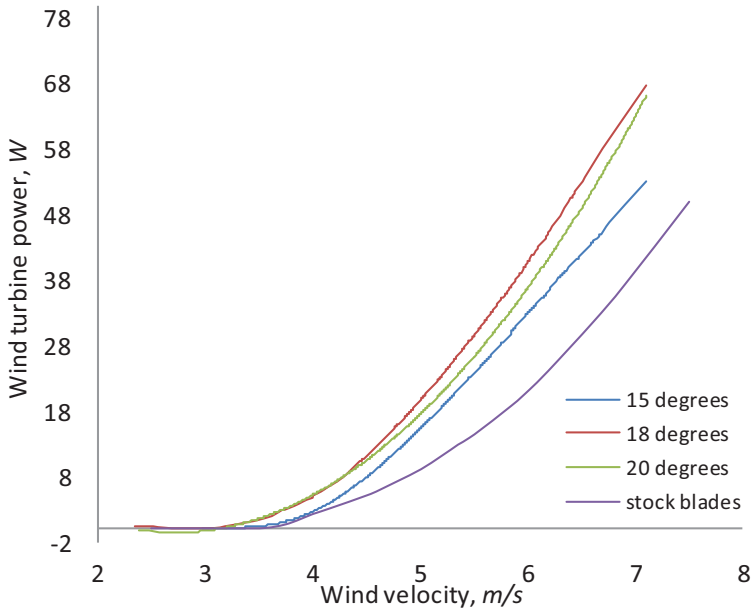

Fig. 6.18 Average power variation vs. wind speed at different pitch angles

6.4.8 Performance measurements of Air X wind turbine with 2-bladed rotor

Performance of the wind turbine with the 2-bladed rotor was evaluated from equation:

$$C_P = \frac{P_T}{P_W} = \frac{VI}{\frac{1}{2}\rho A V_\infty{}^3} \qquad (6.2)$$

Where

P_T is the wind turbine power (W)

P_W is the wind power (W)

V_∞ is the freestream velocity of the wind (m/s)

ρ is the density of air (kg/m^3)

A is the rotor swept area (m^2)

The turbine performance was calculated by considering wind speed; turbine voltage and current that were measured directly during testing and logged. The air density is quite sensitive and frequently changes with weather. It is dependent on atmospheric pressure and ambient air temperature. The relation is shown below (in chapter 4, eqn. 4.2)

$$P_{atm} = \rho RT$$

For the calculation of performance of turbine, the atmospheric pressure was considered constant having a value of 101.3kPa. The ambient temperature was measured on location with a portable Cussons TA2 hot wire temperature probe with a resolution of 1°C. An average temperature value of 25°C was chosen to evaluate the air density. The air density calculated from eqn. 4.2 was 1.184kg/m^3.

The variation of wind turbine performance, C_P vs. wind speed was plotted for 15°, 18° and 20° pitch angles and is given in appendix 3 in figures A3.5 – A3.7. From the performance scatter points, maximum, average and minimum graph have been plotted. They are plotted together for comparison in figures 6.19 – 6.21. From the maximum, average and minimum variations of C_P plots, C_P values corresponding to 3 – 6m/s wind speed in increments of 0.5m/s have been tabulated in tables 6.4 – 6.6.

In figure 6.19, maximum variations of C_P are plotted for the 3 pitch angles. It is seen that C_P at 20° pitch setting dominates C_P at the other 2 pitch settings. The turbine performance at β = 18°

was marginally less than at $\beta = 20°$. At 5m/s and above wind speeds, the C_P of turbine at $\beta = 18°$ started dominating the C_P at $\beta = 20°$. In the wind speed range of 4.5 – 6m/s, C_P ranged from more than 20% to around 30% for pitch settings of 18° and 20° (table 6.4). At 6m/s C_P at $\beta = 18°$ and 20° pitch was close to 30% (29% and 28% respectively).

The minimum variations of C_P graph for the 3 pitch angles is plotted in figure 6.20. The graph shows that C_P at 18° pitch setting dominates performance compared to the other 2 pitch settings. Turbine performance at $\beta = 15°$ is observed to be marginally greater than at $\beta = 20°$ uptill 6m/s wind speed. Table 6.5 shows that the minimum C_P values reaches more than 20% after 5.5 m/s for $\beta = 18°$. C_P at 6m/s is 24% and 20% for $\beta = 18°$ and 20° respectivily.

Figure 6.21 shows the average variation of C_P curves for the 2-bladed rotor at different β settings and the 3-bladed stock rotor. The average performance of Air X is most important compared to the other 2 extreme performances (maximum and mimimum) as it give a true indication of the turbine's general performance level at the respective wind speeds. The turbine has maximum performance at $\beta = 18°$. It is seen that performance at $\beta = 18°$ and 20° coincides with each other up to 4.5m/s wind speed. Beyond 4.5m/s, the 18° pitch setting dominates all other C_P curves. Compared with the performance of Air X turbine with the stock rotor, the 2-bladed rotor configuration achieves greater performance at all pitch settings over the given wind speed range. The performance curve of Air X with the stock rotor matches only with the 2-bladed rotor configuration at $\beta = 15°$ up to 4m/s wind speed. Beyond 4m/s its performance was considerably lower than C_P at $\beta = 15°$.

Table 6.6 shows that Air X wind turbine achieves more than 20% performance at 5m/s wind speed and above at $\beta = 18°$ and 20°. At 6m/s, the turbine attains 20.8%, 25.5% and 24% performance at 15°, 18° and 20° pitch settings respectively whereas with the 3-bladed stock rotor, the turbine achieves 15% performance.

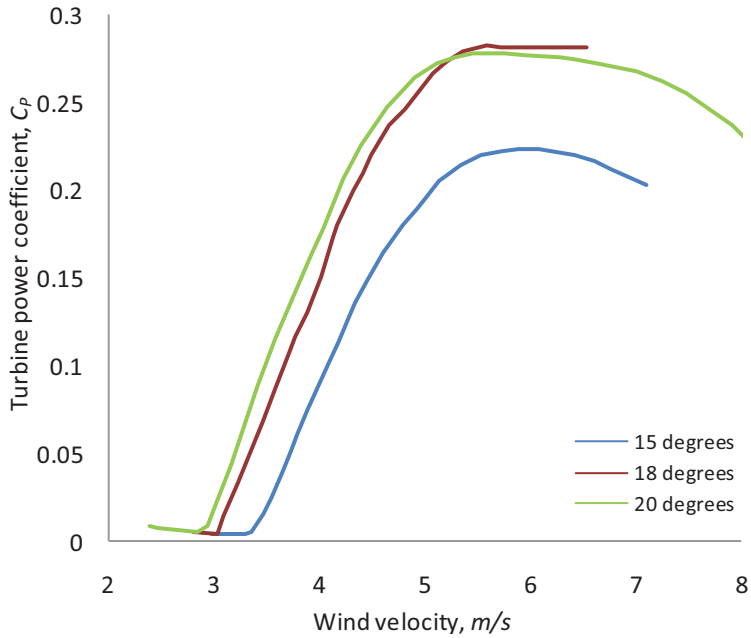

Fig. 6.19 Comparison of maximum performance variations at different pitch settings vs. wind speed

Table 6.4 Comparison of maximum turbine performance with different pitch settings at different wind speeds

Wind speed (m/s)	Maximum turbine performance at different pitch angles (%)		
	15°	18°	20°
3	0.38	1.56	1.47
3.5	2.38	8.23	9.89
4	9.99	15.07	16.94
4.5	15.25	22.71	23.21
5	20.46	27.12	26.94
5.5	22.2	28.2	27.65
6	22.4	29.1	27.7

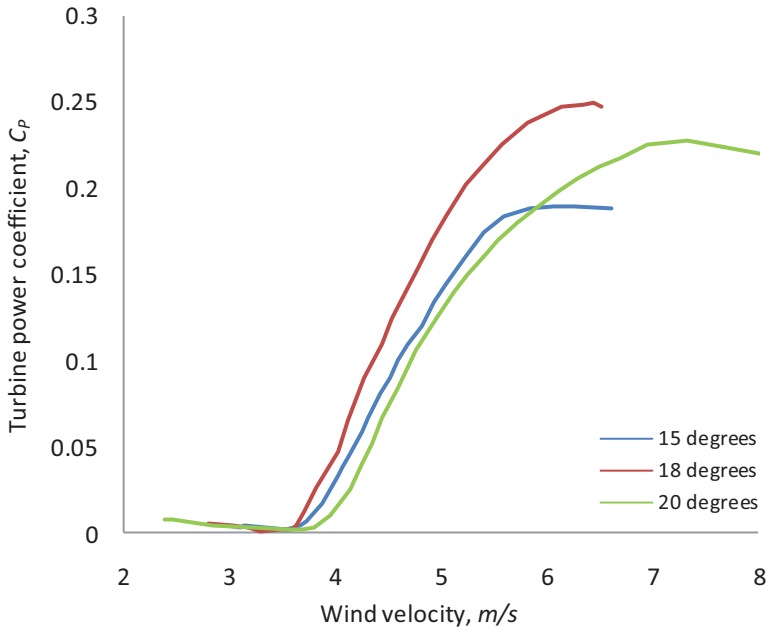

Fig. 6.20 Comparison of minimum performance variations at different pitch settings vs. wind speed

Table 6.5 Comparison of minimum turbine performance with different pitch settings at different wind speeds

Wind speed (m/s)	Minimum turbine performance at different pitch angles (%)		
	15°	18°	20°
3	0.38	0.41	0.41
3.5	0.25	0.25	0.26
4	3.28	4.77	1.81
4.5	8.99	12.48	7.93
5	14.4	18.35	12.6
5.5	17.88	22.07	17.01
6	18.9	24.3	20

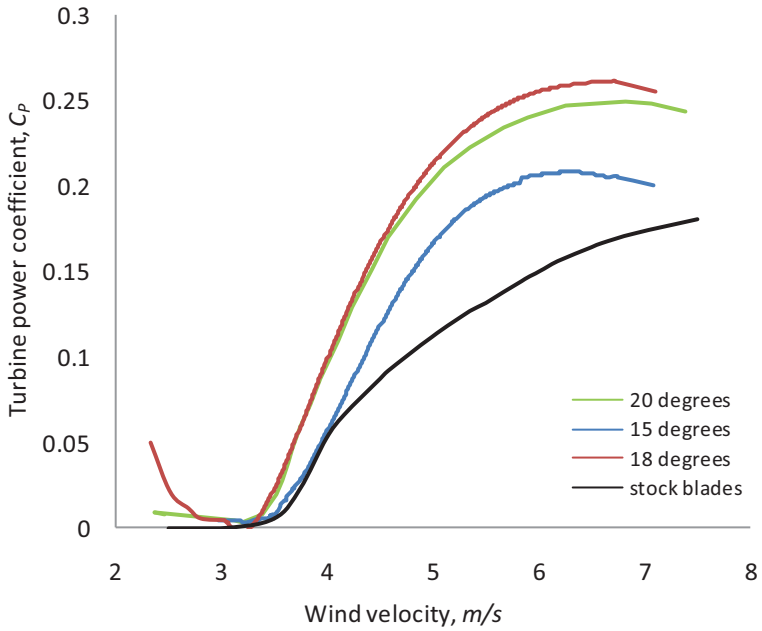

Fig. 6.21 Comparison of average performance variations of a 2-bladed rotor at different pitch settings and 3-bladed stock rotor vs. wind speed

Table 6.6 Comparison of average turbine performance of 2-bladed rotor with different pitch settings and 3-bladed stock rotor at different wind speeds

Wind speed (m/s)	Average turbine performance at different pitch angles (%)			Turbine performance with stock 3-blades (%)
	15°	18°	20°	
3	0.38	0.41	0.41	0
3.5	0.9	2.28	1.95	0.49
4	5.5	10.01	9.52	5.21
4.5	11.8	16.63	15.89	8.67
5	16.61	21.65	21	11.19
5.5	19.36	24.07	22.64	13.15
6	20.8	25.5	24	14.96

6.4.9 Stall and shutdown mode of Air X wind turbine

As discussed earlier in section 6.1.4, the turbine enters stall mode at 15.6m/s wind speed and shuts down completely when the wind speed exceeds 22m/s. During the field testing with the 2-bladed rotor installed, the turbine entered stall mode at an average wind speed of 8m/s during which the turbine had slowed down to slow spin. At higher wind speeds of about 10m/s, the turbine had completely shut down. The rotor was observed to come to a standstill. The graph in

figure 6.22 shows the power variations vs. wind speed during continuous heavy wind speeds, having mean wind speeds of 8.39m/s, peaking to 13m/s (table A3.4 in appendix 3). During this time the rotor was pitched to 20°. The graph shows that the turbine has completely shut down and no power is being produced. Since each shutdown lasts for 5 minutes before the turbine starts rotating again, the turbine was left with very little chance of producing any meaningful power since the wind was constantly blowing at an average speed of 8m/s and above. Only a small amount of power was produced as observed from the graph around 8m/s and 11.5m/s. This most probably occurred during the 5 minute interval when the turbine allowed the rotor to spin and brake it when it sensed too high a wind speed. In between this time the turbine would have trickle charged the battery. The flat line in the power curve from 1m/s to 13m/s indicates a complete shutdown. Since the turbine goes into complete shutdown mode for 5 minutes, it does not monitor the wind speed for the next 5 minutes. In between this time, even if the wind decreases and stays say for example at 5 or 6m/s, the turbine would still be in shutdown mode. For this reason, the turbine produces no power at the low wind speeds that was captured momentarily. The wind speed variations in figure A3.4 in appendix 3 shows that the turbine was operating on average, between a minimum average speed of 6.5m/s and a maximum average speed of 9m/s.

Figure 6.23 shows the comparison of normal operation to shutdown mode of Air X wind turbine with the 2-bladed rotor. Figure 6.24 shows the operation of Air X wind turbine with the 3-bladed rotor tested by NREL [**63**]. The NREL test of Air X was conducted at a height of 13m. The power variation in the graph in figure 6.24 is made up of 10sec data points. All the 3 modes of operation of Air X are depicted in the graph. They consist of normal power production, stall mode and shutdown mode. From the graph, instantaneous cut-in wind speed occurs around 3.5 – 3.6m/s analogous to a cut-in wind speed of 3.58m/s as claimed in the Air X owner's manual [**61**]. Similar tests of Air X wind turbine were also conducted by Paul Gipe [**64**] and Southwest wind power (SWWP) [**65**]. The comparison is shown in figure 6.25 where there is good correlation between Paul Gipe's data, NREL's bin 10min data and SWW's turbulent data below 10m/s wind speed. Above 10m/s, Paul Gipe's and NRELs power curve data do not match with SWWP because of the difference in sampling rate taken for the power plots. Paul Gipe recorded 1min average data for power while NRE and SWWP recorded 10min average and instantaneous data respectively. Power characteristics between normal operation and stall mode have been omitted

by SWWP and thus the observation of a straight drop in power from the point of maximum power production to minimal power production (stall).

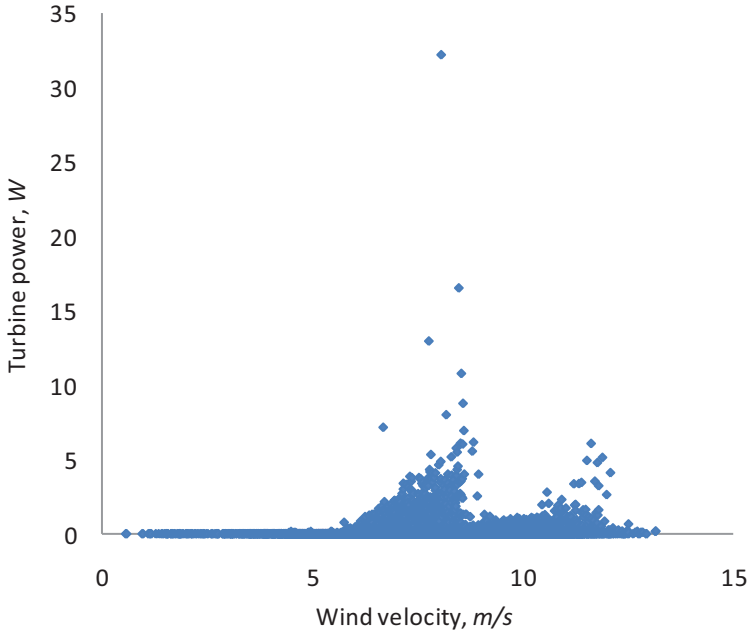

Fig. 6.22 Wind turbine power variation vs. wind speed for 20° pitch angle

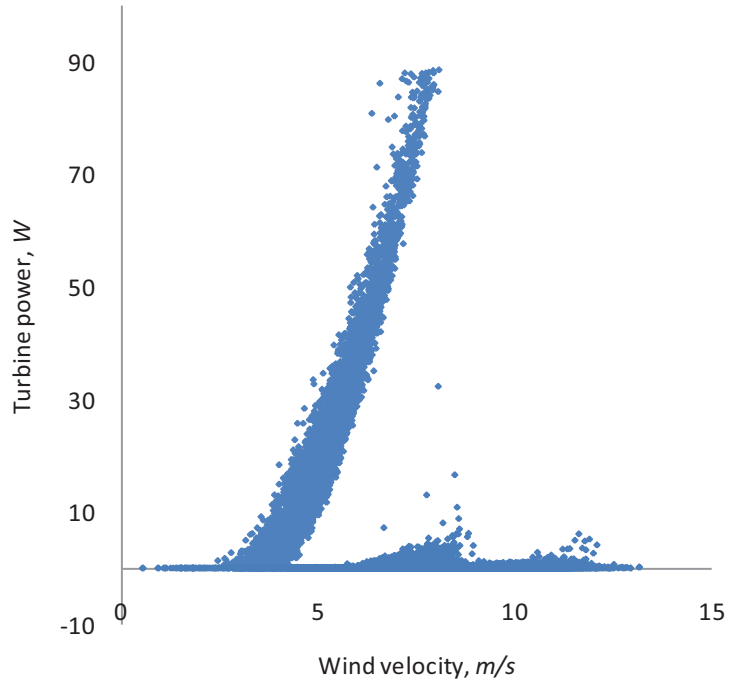

Fig. 6.23 Wind turbine power variation vs. wind speed for 20° pitch angle during normal operation and shutdown mode

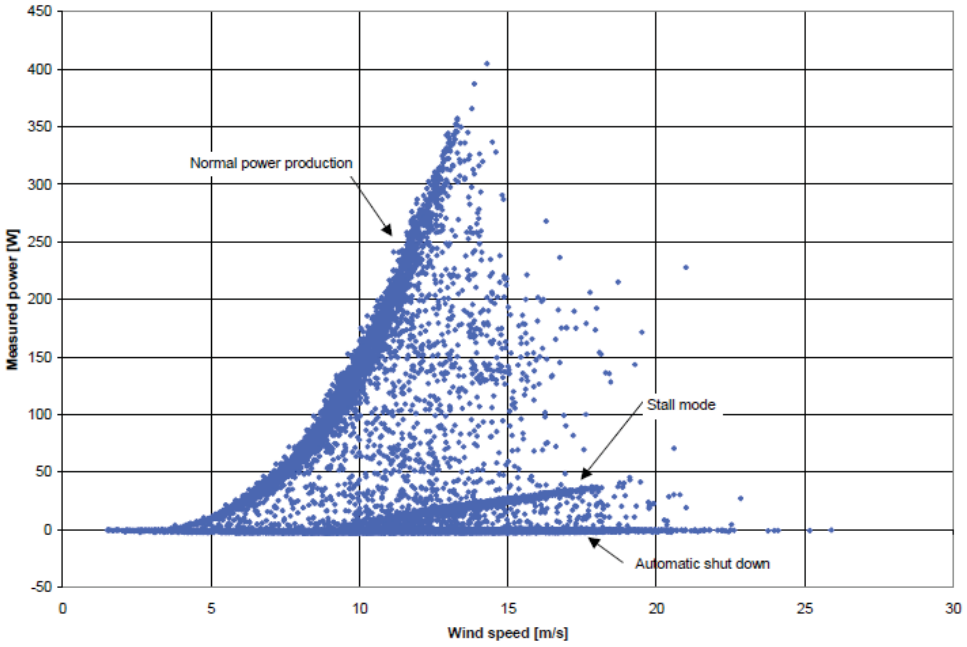

Fig. 6.24 Power variation of Air X with stock rotor at different wind speeds [**63**]

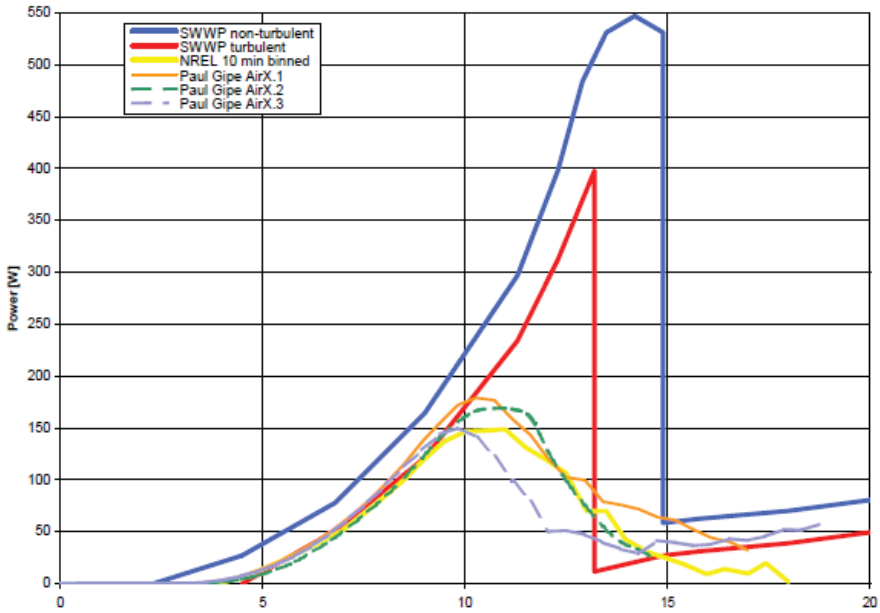

Fig. 6.25 Power variation of Air X with stock rotor by NREL, SWWP and Paul Gape at different wind speeds [**63**]

6.4.10 Performance of 2-bladed rotor compared to stock 3-bladed rotor

The 2-bladed rotor blades attained faster startup and cut-in wind speed when compared to the stock 3-bladed rotor. With the stock blades, the Air X goes into stall mode and shutdown mode at 15.6m/s and 22m/s respectively. With the 2-bladed rotor it went into stall mode around 8m/s and shutdown mode at around 10m/s wind speed. The turbine stalls and shuts down at lower

wind speeds with the 2-bladed rotor as it achieves faster rpm compared to the stock rotor. Not only did the 2-bladed rotor achieve high rpm, but it also achieved high torque at lower wind speeds as proved in figure 6.21 where at all the 3 pitch angles, the 2-bladed rotor out performed the stock rotor. The way Air X sensors the wind speed is through a magnetic rpm sensor (figure 6.26). The sensor senses the magnetic fluxes of the spinning alternator that is connected directily to the rotors. The turbine's microprocessor is programed to relate rpm to wind speed through a reference equation or ratio in relation to the stock blades only. That is to say that a relationship between wind speed and rotor rpm has been found specific to the stock blades and stored in the microprocessorsrs memory. The microprocessor simply measures rpm and from the relation between rpm and wind speed matches it to the corrosponding wind speed. This method of judging the wind speed through rpm sensing has been responsible for the early shutdown of the turbine with 2-bladed rotor at 10m/s instead of 22m/s. This shows that the 2-bladed rotor gained the same amount of rotational speed at 10m/s that the 3-bladed stock rotor did at 22m/s. Also, since the 2-bladed rotor did this under load, it produced more torque at the same rpm as the 3-bladed stock rotor, since it had greater performance at the same wind speeds.

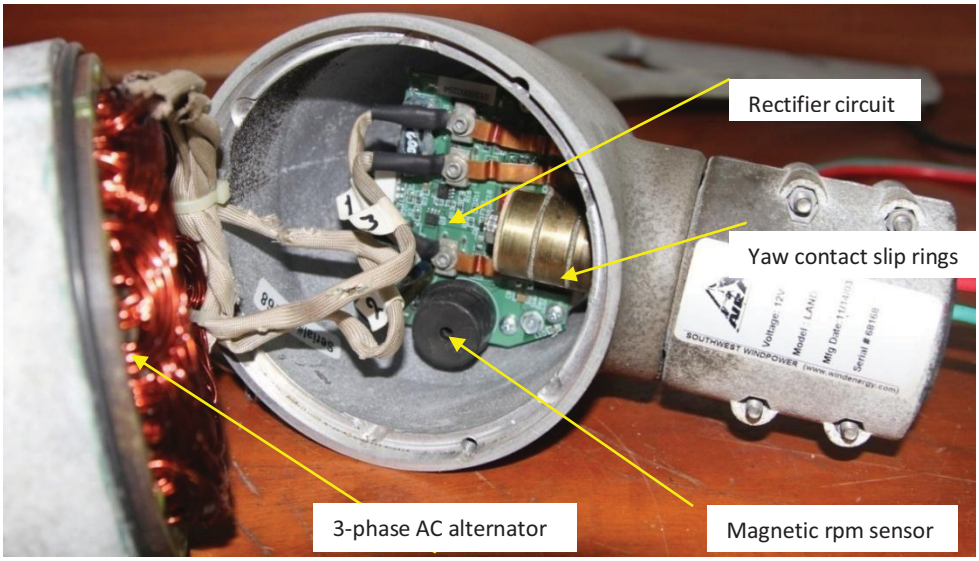

Fig. 6.26 Air X internal circuitry showing the rpm senor

Chapter 7 Conclusion

A 2-bladed rotor was designed for the Air X wind turbine to operate in low wind speed conditions that are experienced in Fiji. The blades incorporated twist and taper distribution for a more aerodynamic efficient design. The cross section of the blades consisted of the AF300 flatback airfoil, specially designed to achieve high lift at low Reynolds numbers and provide structural stability to the blades. The added structural strength as a result of the flatback trailing edge meant that the blades could be made from even lighter materials benefiting the rotor with low inertia thus producing lower startup and cut-in wind speeds.

The AF300 airfoil was designed and improved from existing low speed airfoils through *xfoil* code. The airfoil was tested in the Reynolds number range of 38000 – 205000 that correspond to 6 – 32m/s design specific relative velocities, V_{rel}. Extensive wind tunnel testing was performed to evaluate the aerodynamic characteristics of the airfoil at low Reynolds number. Together with experimentation, *ansys* CFX, PIV tests and smoke flow visualization of the airfoil were conducted. The airfoil showed good lift characteristics at low Reynolds numbers and maintained fully attached flow at angle of attack as high as 14° due to the flatback trailing edge that delayed flow separation. Experimental results of the variation of lift coefficients showed that at Re = 38000, C_L values ranged from 0.41 – 1.05 for α = 0 – 18°. At Re = 75000, 128000 and 205000, C_{Lmax} = 1.72, 1.81 and 1.86 respectively for α_{stall} = 14°. Smoke flow visualization showed that the airfoil had fully attached flow regime at α_{stall} for Reynolds number as low as 75000. Experimental, *xfoil* and *ansys* CFX plots of pressure distribution showed good agreement with each other.

The 2-bladed rotor was manufactured from wood to be light and designed to operate in wind speeds as low as 5m/s which is common to Fiji. The rotor incorporated an exponential twist and taper distribution and the AF300 airfoil for increased aerodynamic performance at low wind speeds. The chord distribution of the blades resulted in the outer portion to have higher solidity compared to the stock blades to have a fast start up and low cut-in wind speed. The 2-bladed design had a solidity of 8.27% as compared to 8.42% of the stock blades.

Air X marine turbine was field tested at 3 different pitch angels of 15°, 18° and 20°, with the blades performing best at 18°. The 2-bladed rotor achieved an instantanious and average cut-in

wind speed of 2.34m/s and 3.24m/s respectively compared to the 3.58m/s cut-in wind speed of the stock blades. Performance of Air X with the 2-bladed rotor was compared to the stock rotor and found that the 2-bladed rotor had better C_P in the low wind speed range of 3 – 6m/s. The 2-bladed rotor achived C_P values of 10%, 21.7% and 25.5% at 4, 5 and 6m/s wind speed respectively wherease the stock bladed Air X achieved only 5.2%, 11.2% and 15%. Peak performance attained by the 2-bladed rotor design was 29% at 6m/s wind speed.

In conclusion, the 2-bladed rotor with the same rotor solidity as the stock 3-bladed rotor was aerodynamically improved with twist and chord distribution and a high lift, low *Re* airfoil cross section to have faster start-ups, have low cut-in wind speeds and achieve good performance around wind speeds of 5m/s.

References

[1] A. Kumar and S. Prasad, Examining wind quality and wind power prospects on Fiji Islands, (Technical Note), Journal of Renewable Energy, 2010; 35: 536–540.

[2] E. Hau, Wind Turbines – Fundamentals, Technologies, Application, Economics, 2006, 2nd ed, Springer, United Kingdom.

[3] F. Wang, L. Bai, J. Fletcher, J. Whiteford and D. Cullen, The methodology for aerodynamic study on a small domestic wind turbine with scoop, Journal of Wind Engineering and Industrial Aerodynamics, 2008; 96:1–24.

[4] O. Ozgener and L. Ozgener, Exergy and reliability analysis of wind turbine systems: A case study, Journal of Renewable and Sustainable Energy Reviews, 20007; 11:1811–1826.

[5] G.M.J. Herbert, S. Iniyan, E. Sreevalsan and S. Rajapandian, A review of wind energy technologies, Journal of Renewable and Sustainable Energy Reviews, 2007; 11:1117–1145.

[6] K. Abe, M. Nishida, A. Sakurai, Y. Ohya, H. Kihara, E. Wada and K. Sato, Experimental and numerical investigations of flow fields behind a small wind turbine with a flanged diffuser, Journal of Wind Engineering and Industrial Aerodynamics, 2005; 93: 951–970.

[7] H. Reents,Windkonzentratoren,Munich, Deutscher Physiker-Tag, 1985.

[8] P. Cooper, P.B. Kosasih and L. Ledo, Roof mounting site analysis for micro-wind turbines, Renewable Energy Journal, 2010; 36:1379-1391.

[9] M.A Badr and K.Y. Maalawi, A practical approach for selecting optimum wind rotors, Journal of Renewable Energy, 2003; 28: 803 – 822.

[10] H.F. Fasel and A. Gross, Numerical Investigation of Different Wind Turbine Airfoils,2007, The University of Arizona, Tucson, Orlando, Florida.

[11] C. Mayer, M.E. Bechly, M. Hampsey and D.H. Wood, The starting behaviour of a small horizontal-axis wind turbine, Journal of Renewable Energy, 2001; 22:411-417.

[12] P. D. Clausen and D. H. Wood, Research and Development Issues for Small Wind Turbines, Journal of Renewable Energy, 1999; 16: 922 - 927.

[13] A.D. Peacock, D. Jenkins, M. Ahadzi, A. Berry and S. Turan, Micro wind turbines in the UK domestic sector, Energy and Buildings, Journal of Renewable Energy, 2008; 40:1324–1333.

[14] B. D. McGranahan and M. S. Selig, Wind Tunnel Aerodynamic Tests of Six Airfoils for Use on Small Wind Turbines, 2004, National Renewable Energy Laboratory, Colorado.

[15] P. Giguère and M. S. Selig, Low Reynolds Number Airfoils for Small Horizontal Axis Wind Turbines, Journal of Wind Engineering, 1997; 21:379.

[16] J. Hall, K. Mohseni and M. Sahin, Direct Numerical Simulation of Separated Low-Reynolds Number Flows around an Eppler 387 Airfoil, 2007, Department of Aerospace Engineering Sciences, University of Colorado, Boulder, Colorado.

[17] J. L. Tangler, The Evolution of Rotor and Blade Design, 2000, National Renewable Energy Laboratory, Colorado.

[18] S. J. Miley, A Catalog of Low Reynolds Number Airfoil Data for Wind Turbine Applications, 1982, Department of Aerospace Engineering Texas A&M University College Station, Texas.

[19] J. Elizondo, J. Martı´nez and O. Probst, Experimental study of a small wind turbine for low- and medium-wind regimes, International Journal of Energy Research, 2009; 33: 309-326.

[20] P. B. S. Lissaman, Low-Reynolds-Number Airfoils, Annual Reviews of Fluid Mechanics, 1983; 15:223-239

[21] P. Giguère and M. S. Selig, New Airfoils for Small Horizontal Axis Wind Turbines, Journal of Wind Engineering, 1998; 120:111.

[22] J. D. Anderson, Fundamentals of Aerodynamics, 2001, 3rd ed., McGraw Hill, New York.

[23] M. Drela, Low-Reynolds-Number Airfoil Design for the M.I.T. Daedalus Prototype: A Case Study, Journal of American Institute of Aeronautics and Astronautics, 1988; 24.

[24] J.C.C. Henriques, F. Marques da Silva, A.I. Estanqueiro and L.M.C. Gato, Design of a new urban wind turbine airfoil using a pressure-load inverse method, Journal of Renewable Energy, 2009; 34:2728–2734.

[25] A.K. Wright and D.H. Wood, The starting and low wind speed behaviour of a small horizontal axis wind turbine, Journal of Wind Engineering and Industrial Aerodynamics, 2004; 92: 1265 – 1279.

[26] P. R. Ebert and D. H. Wood, Observations of The Starting Behaviour of A Small Horizontal axis wind Turbine, Journal of Renewable Energy, 1997; 12: 245 – 257.

[27] R. Lanzafame and M. Messina, Design and performance of a double-pitch wind turbine with non-twisted blades, Journal of Renewable Energy, 2009; 34: 1413 – 1420.

[28] M. S. Selig and J. J. Guglielmo, High-Lift Low Reynolds Number Airfoil Design, Journal of Aircraft, 1997, Vol. 34.

[29] R. Lanzafame and M. Messina, Fluid dynamics wind turbine design: Critical analysis, optimization and application of BEM theory, Journal of Renewable Energy, 2007; 32: 2291 – 2305.

[30] J. F. Manwell, J. G. Mcgowan and A. L. Rogers, Wind energy explained – theory, design and application, John Wiley and Sons Ltd, England, 2002.

[31] M.L.Hansen, Aerodynamics of wind turbines, 2nd ed. Earthscan publishing,2008, London, UK.

[32] N. A. Cenaelle, Aerodynamic optimization of a small scale wind turbine, for low wind turbine blade for low speed conditions, 2006, University of Stellenbosch.

[33] T. Chitsomboon, C. Thumthae, Optimal angle of attack for untwisted blade wind turbine, Journal of Renewable Energy, 2009; 34: 1279 – 1284.

[34] Y. Kamada, H. Kawabuchi, E. Ismaili and T. Maeda, Surface Pressure Distribution on a Blade of a 10 m Diameter HAWT (Field Measurements versus Wind Tunnel Measurements), Journal of Solar Energy Engineering, 2005; 127.

[35] P. Devinant, J. Hureau, S. Loyer and C. Sicot, Rotational and turbulence effects on a wind turbine blade. Investigation of the stall mechanisms, Journal of Wind Engineering and Industrial Aerodynamics, 2008; 96: 1320 – 1331.

[36] M. Robinson and S. Schreck, Wind Turbine Blade Flow Fields and Prospects for Active Aerodynamic Control, 2007, National Renewable Energy Laboratory, Colorado.

[37] H. Himmelskamp, Profile investigations on a rotating airscrew, 1945, Gottingen, Germany.

[38] W. Banks, G. Gadd, Delaying effect of rotation on laminar separation, Journal of American Institute of Aeronautics and Astronautics, 1963; 1: 941 – 942.

[39] J. L. Tangler, Insight into wind turbine stall and post-stall aerodynamics, Journal of Wind Energy, 2004; 7: 247 – 260.

[40] G. Ronsten, Static pressure measurements on a rotating and a non-rotating 2.375m wind turbine blade. Comparison with 2D calculations, Journal of Wind Engineering and Industrial Aerodynamics, 1992; 39: 105 – 115.

[41] Ph. Devinant, J. Hureau and T. Laverne, Experimental study of wind-turbine airfoil aerodynamics in high turbulence, Journal of Wind Engineering and Industrial Aerodynamics, 2002; 90: 689 – 707.

[42] G. M. Craig, Stop abusing Bernoulli – how airplanes really fly, 1997, Regenerative Press,

Anderson Indiana.

[43] UIUC Applied Aerodynamics Groups, Airfoil Database accessed online on 8th August, 2009 at 9.34am from www.ae.illinois.edu/m-selig/ads/coord_database.html

[44] M. Drela, xfoil 6.94 user guide, MIT Aero and Astro, 2001.

[45] S. Duran, computer-aided design of horizontal-axis wind turbine blades, The Graduate School of Natural and Applied Sciences, 2005, Middle East Technical University.

[46] J. M. Jonkman, Modeling of the UAE Wind Turbine for Refinement of FAST_AD, 2003, National Renewable Energy Laboratory, Colorado.

[47] P. S. Lissaman and R. E. Wilson, Applied aerodynamics of wind power machines, Oregon State University, Oregon, 1974.

[48] P. Giguère and M. S. Selig, Desirable Airfoil Characteristics for Large Variable – Speed Horizontal Axis Wind Turbines, Journal of Solar Energy, 1997:119:255.

[49] J. P. Baker, C.P. Van Dam, and B. L. Gilbert, Flatback Airfoil Wind Tunnel Experiment, 2008, Sandia National Laboratories Albuquerque, New Mexico.

[50] E. N. Duque, C. P. Stone and S. M. Tebo, Computational Fluid Dynamics of Flatback Airfoils for Wind Turbine Applications, Journal of American Institute of Aeronautics and Astronautics, 2006; 2006-194.

[51] J. B. Barlow, W. H. Rae and A. Pope, Low Speed Wind Tunnel Testing, 1999, (Third Edition), John Wiley and Sons, New York.

[52] M. R. D'Angelo, The Effects of Trailing Edge Bluntness on Airfoil Performance as calculated approximately by a Viscid-Inviscid Vortex Panel Method, 1988, Massachusetts Institute of Technology, Massachusetts.

[53] P. Giguère and M.S. Selig, Design of a Tapered and Twisted Blade for the NREL Combined Experiment Rotor, 1999, National Renewable Energy Laboratory, Colorado.

[54] A. D. Sahin, Progress and recent trends in wind energy, Journal of Progress in Energy and Combustion Science, 2004; 30: 501 – 543.

[55] S.M. Habali and I.A. Saleh, Local design, testing and manufacturing of small mixed airfoil wind turbine blades of glass fiber reinforced plastics Part I: Design of the blade and root, Journal of Energy Conversion & Management, 2000; 41: 249 – 280.

[56] R. Lanzafame and M. Messina, Power curve control in micro wind turbine design, Journal of Energy, 2009; 1 – 6.

[57] H. Hirahara, M. Z. Hossain and Y. Nonomura, Testing basic performance of a very small wind turbine designed for multi – purposes, Journal of Renewable Energy, 2005; 30: 1279 – 1297.

[58] K. Ameku, B. M. Nagai and J. N. Roy, Design of a 3 kW wind turbine generator with thin airfoil blades, Experimental Thermal and Fluid Science, 2008; 32: 1723 – 1730.

[59] A. S. Alston, Timbers of Fiji: properties and potential uses, 1982, Department of Forestry, Suva, Fiji.

[60] Air X owner's manual, Southwest Windpower, Inc, 2002, Flagstaff, Arizona.

[61] Air X owner's manual, Southwest Windpower, Inc, 2008, Flagstaff, Arizona.

[62] Location of USPs Marine campus, accessed online on 12th May, 2011 at 2pm from, http://www.googleearth.com

[63] J. van Dam, P. Migliore, M. Meadors and H. Link, Power Performance Test Report for the Southwest Windpower AIR-X Wind Turbine, 2003, National Renewable Energy Laboratory, Colorado.

[64] P. Gipe, Air X Fails Power Curve Tests, accessed online on 10th January, 2011 at 10am from: http://homepages.enterprise.net/huge0pigg/gipe.

[65] IEC 61400-12: Wind Turbine Generator Systems—Part 12: Wind Turbine Power Performance Testing, 1st ed, 2002, International Electro technical Commission.

Appendix 1

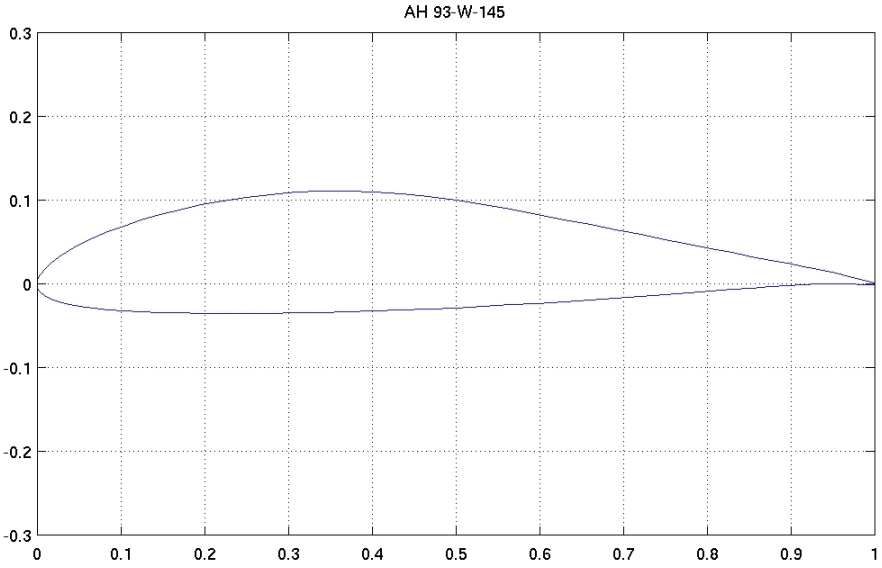

Fig. A1.1 A1 - ah93w145 Althaus AH 93-W-145 airfoil for use on wind turbines [43]

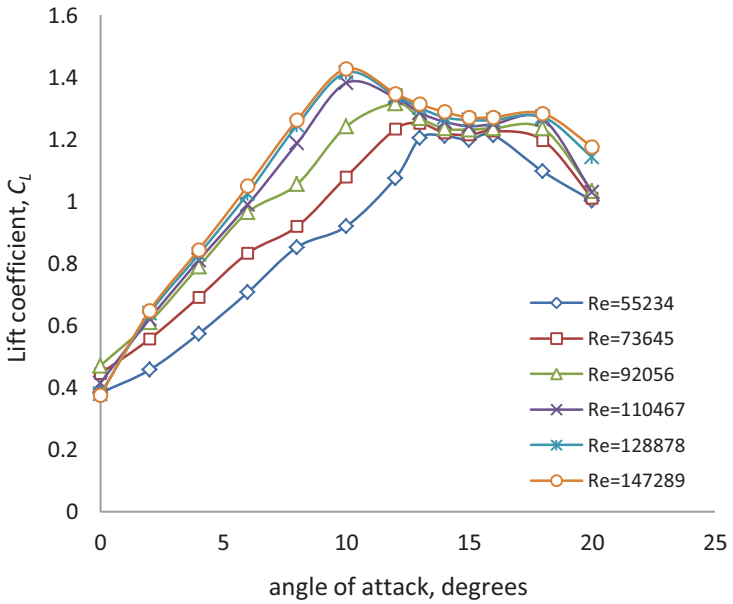

Fig. A1.2 Graph of lift vs. angle of attack at various Reynolds number

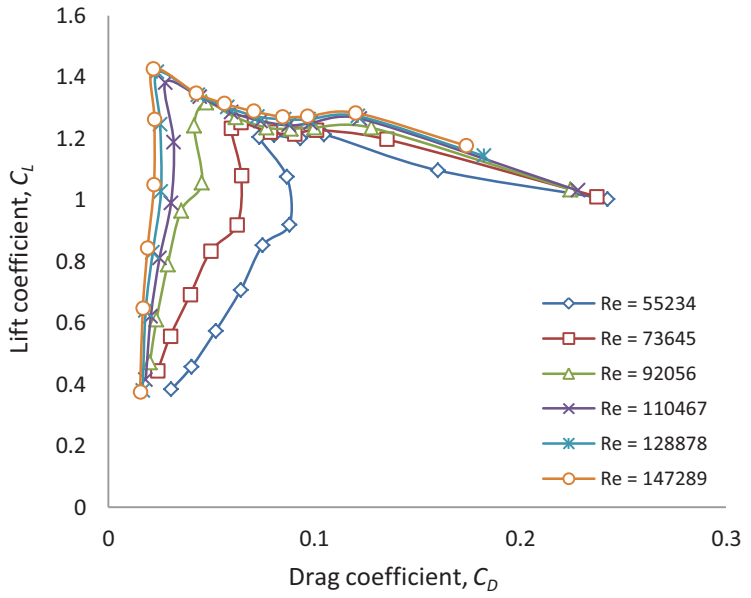

Fig. A1.3 Drag polar plot – lift vs. drag at various Reynolds number

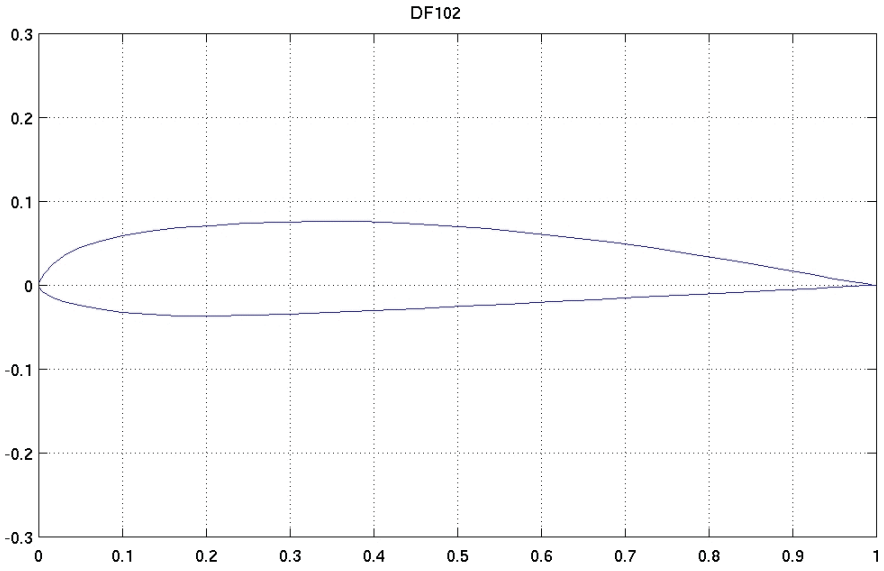

Fig. A1.4 A2 - df102 David Fraser DF 102 low Reynolds number airfoil [43]

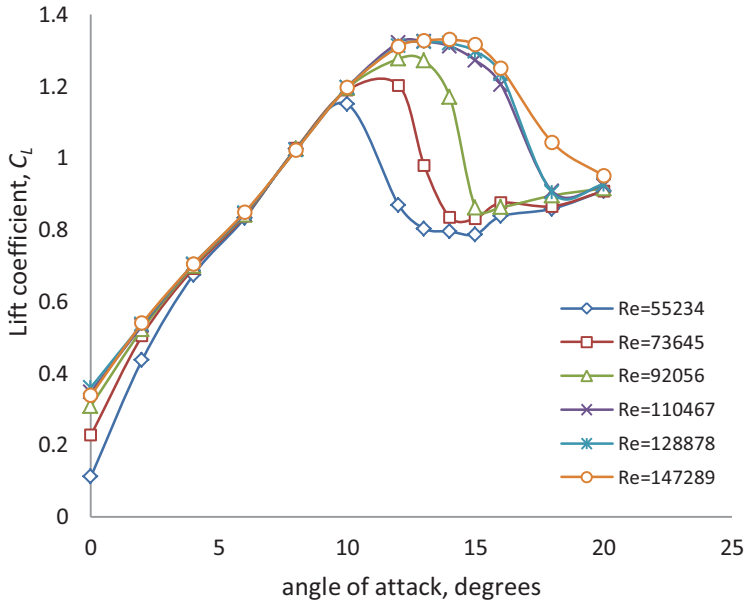

Fig A1.5 Graph of lift vs. angle of attack at various Reynolds number

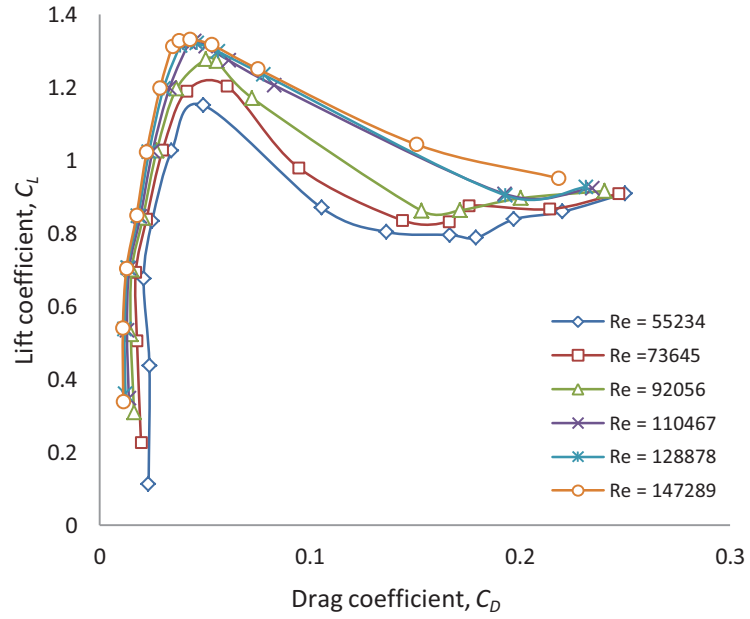

Fig. A1.6 Drag polar plots – lift vs. drag at various Reynolds number

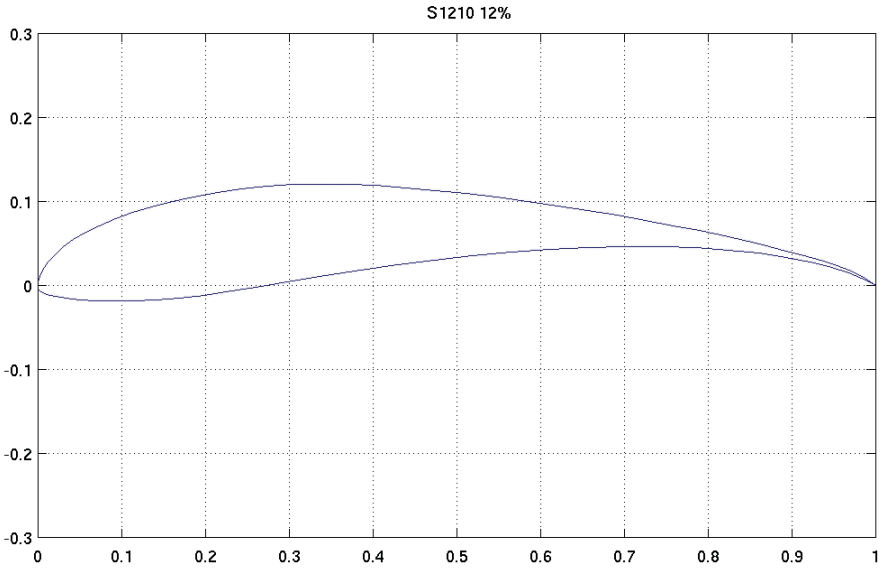

Fig. A1.7 A3 - s1210 Selig high lift low Reynolds number airfoil [43]

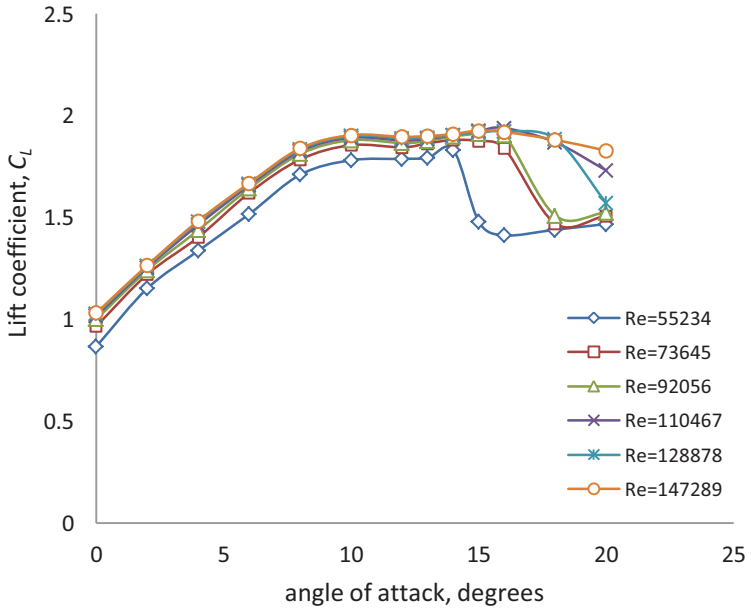

Fig. A1.8 Graph of lift vs. angle of attack at various Reynolds number

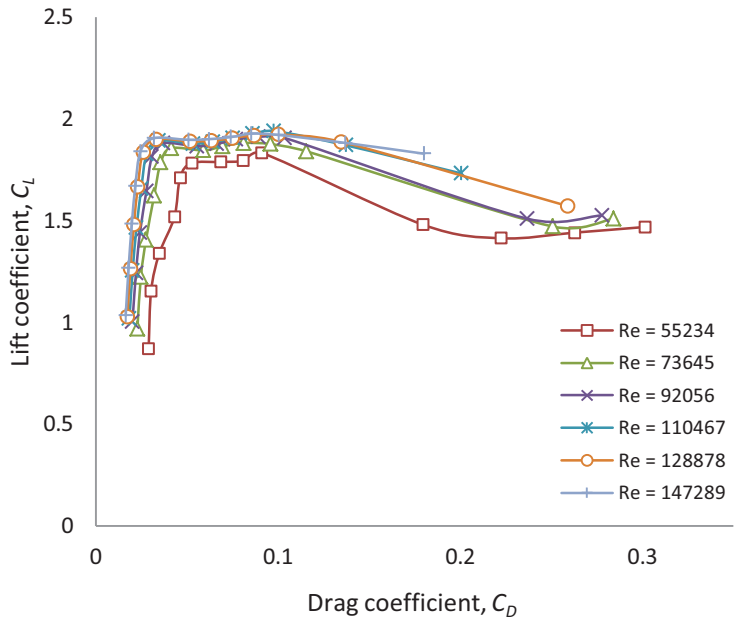

Fig. A1.9 Drag polar plots – lift vs. drag at various Reynolds number

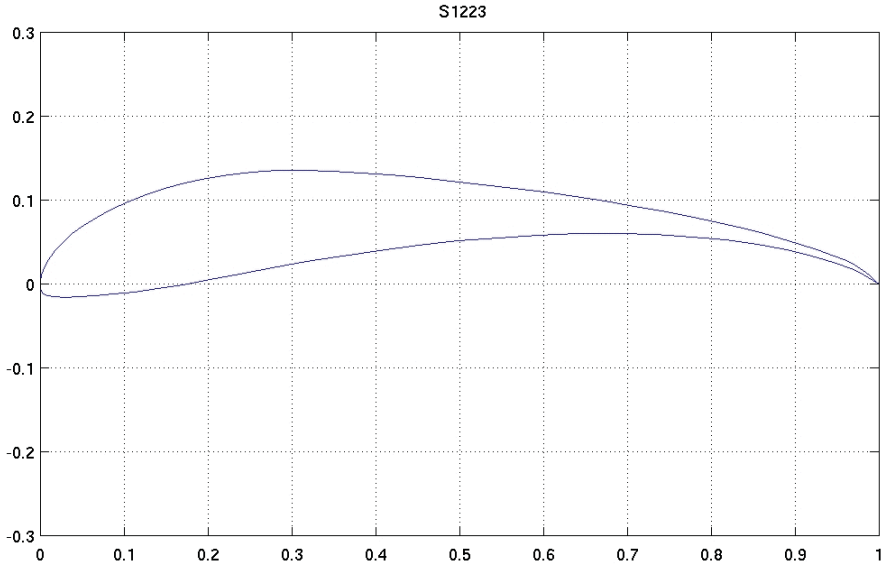

Fig. A1.10 A4 - s1223 Selig high lift low Reynolds number airfoil [43]

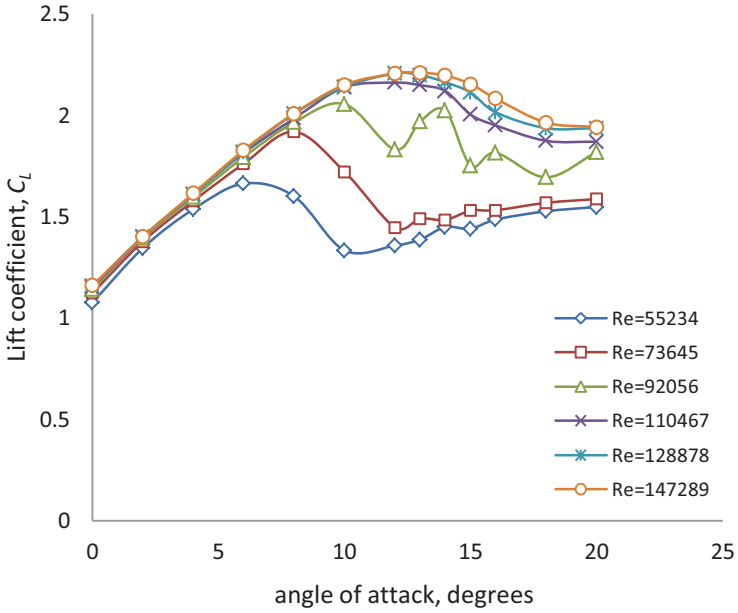

Fig. A1.11 Graph of lift vs. angle of attack at various Reynolds number

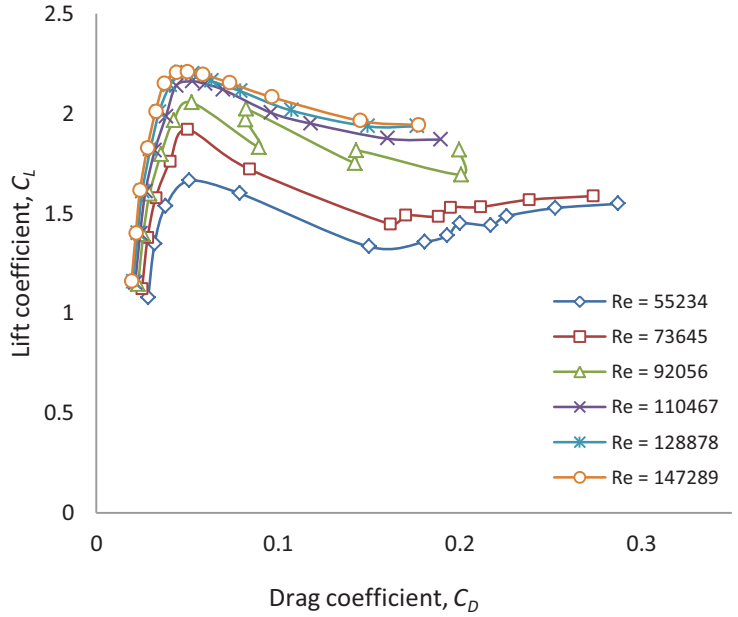

Fig. A1.12 Drag polar plots – lift vs. drag at various Reynolds number

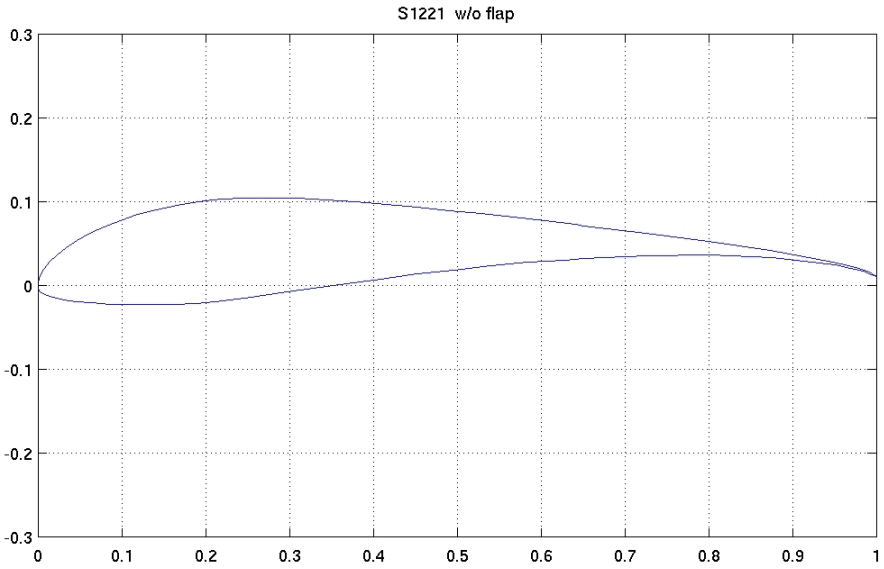

Fig. 1.13 A5 - s1221 Selig airfoil [43]

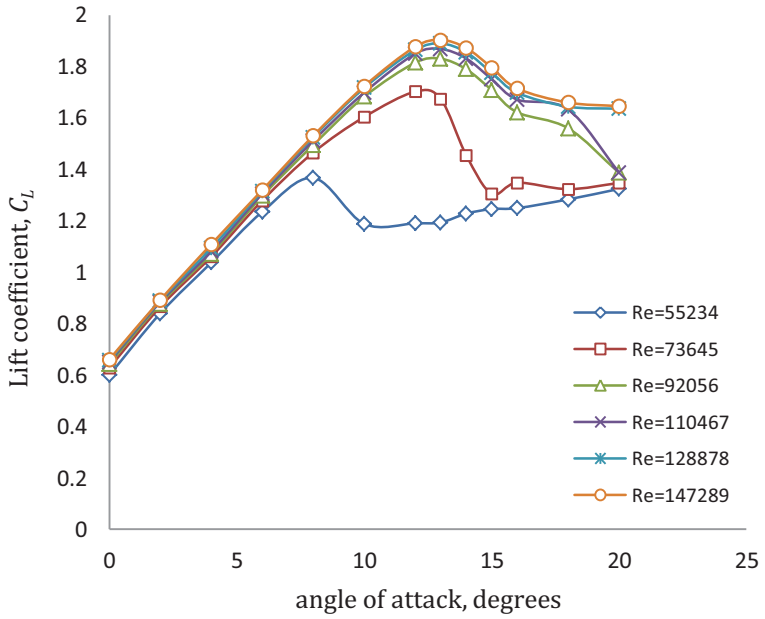

Fig. A1.14 Graph of lift vs. angle of attack at various Reynolds number

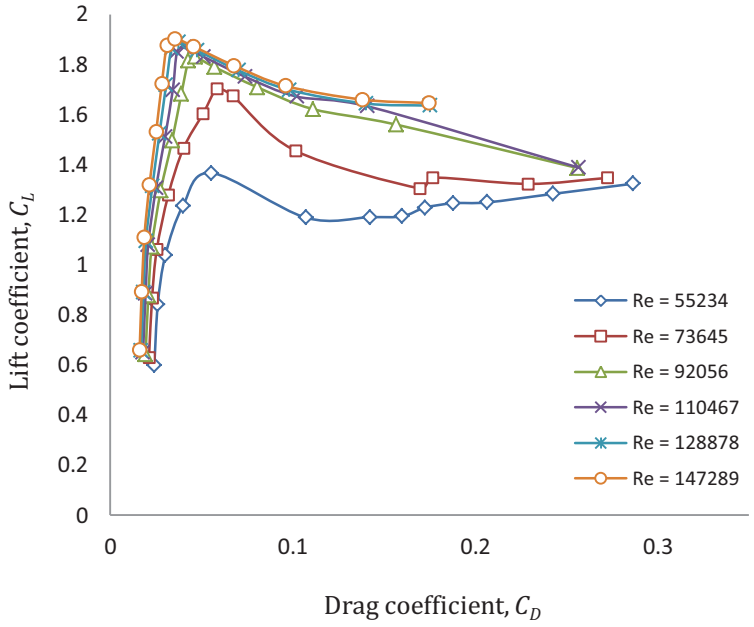

Fig. A1.15 Drag polar plots – lift vs. drag at various Reynolds number

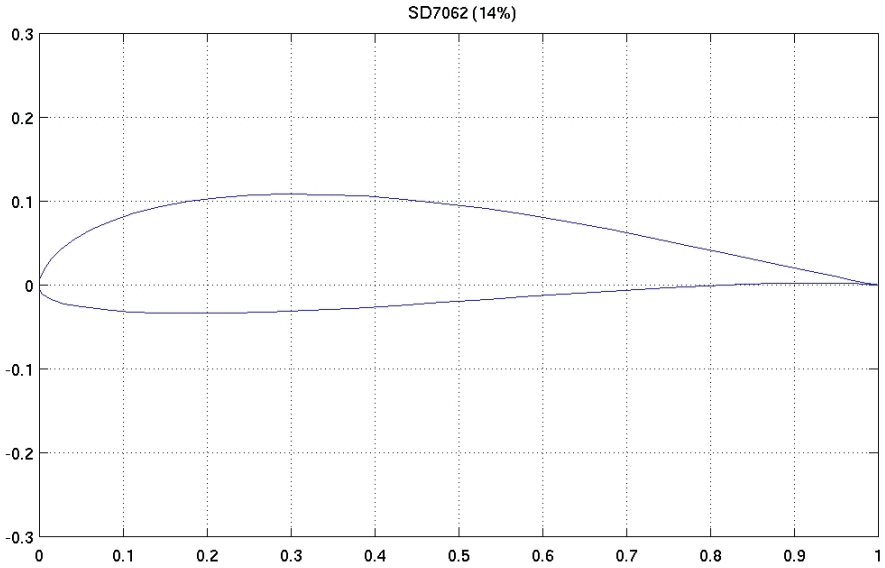

Fig. A1.16 A6 – Selig/Donovan SD7062 low Reynolds number airfoil [43]

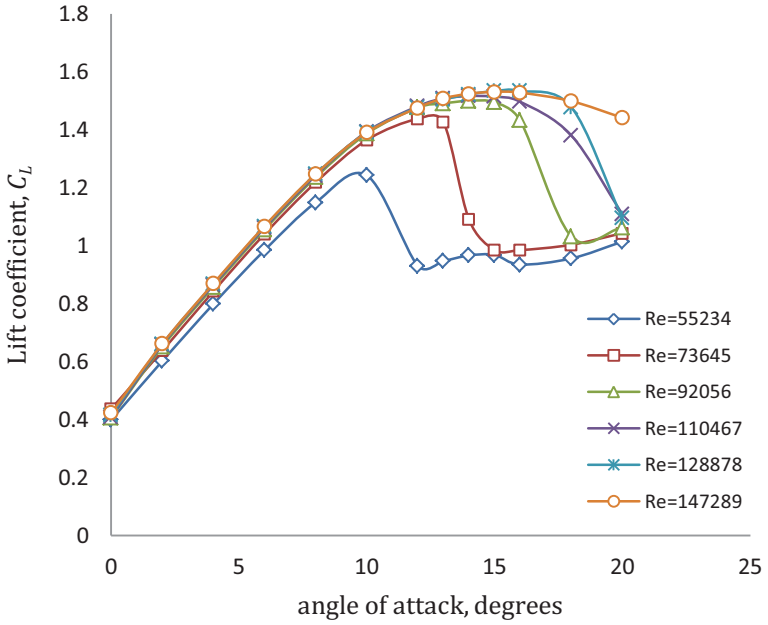

Fig. A1.17 Graph of lift vs. angle of attack at various Reynolds number

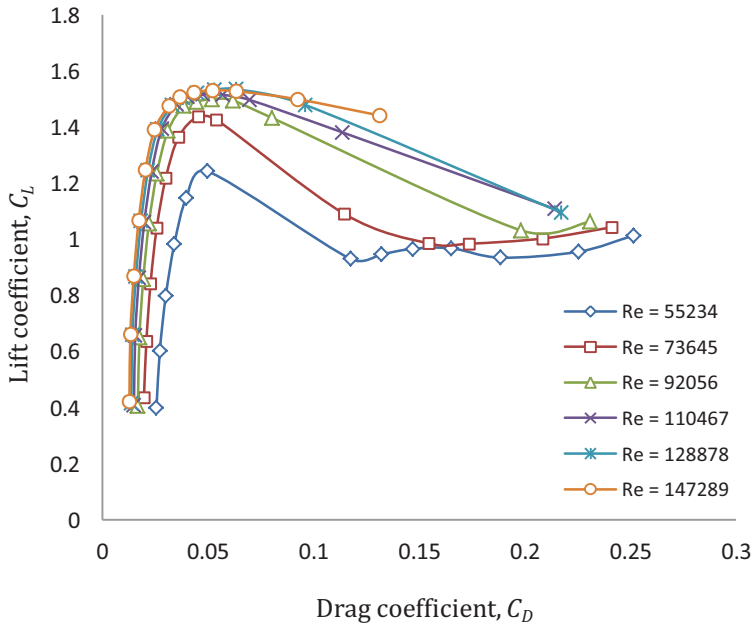

Fig. A1.18 Drag polar plots – lift vs. drag at various Reynolds number

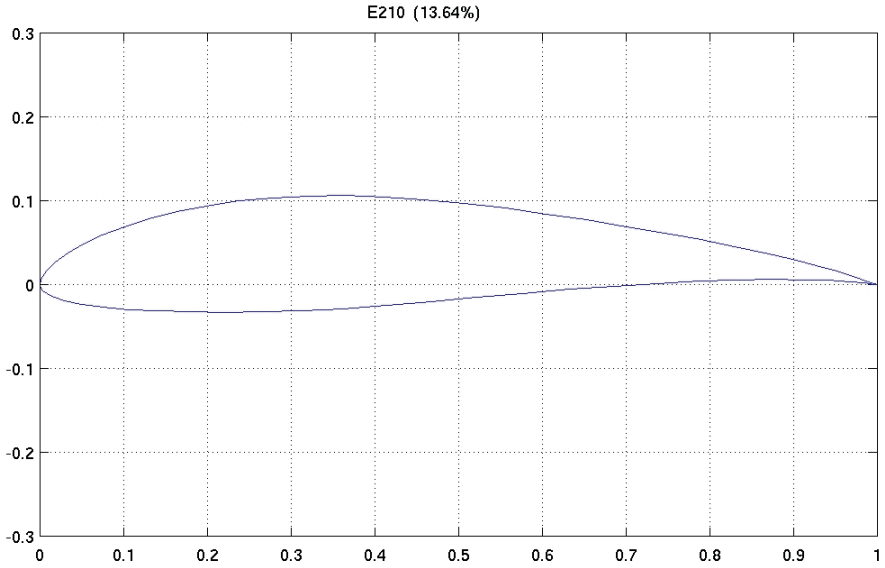

Fig. A1.19 A7 - E210 Eppler low Reynolds number airfoil [43]

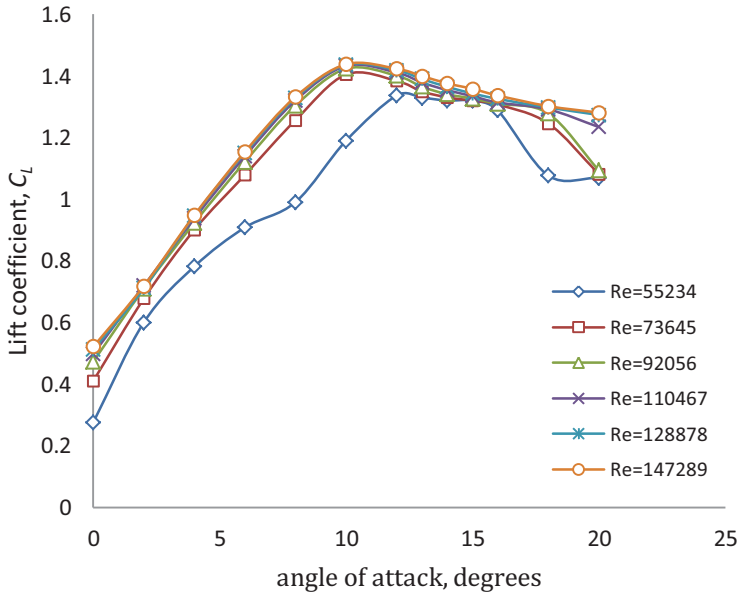

Fig. A1.20 Graph of lift vs. angle of attack at various Reynolds number

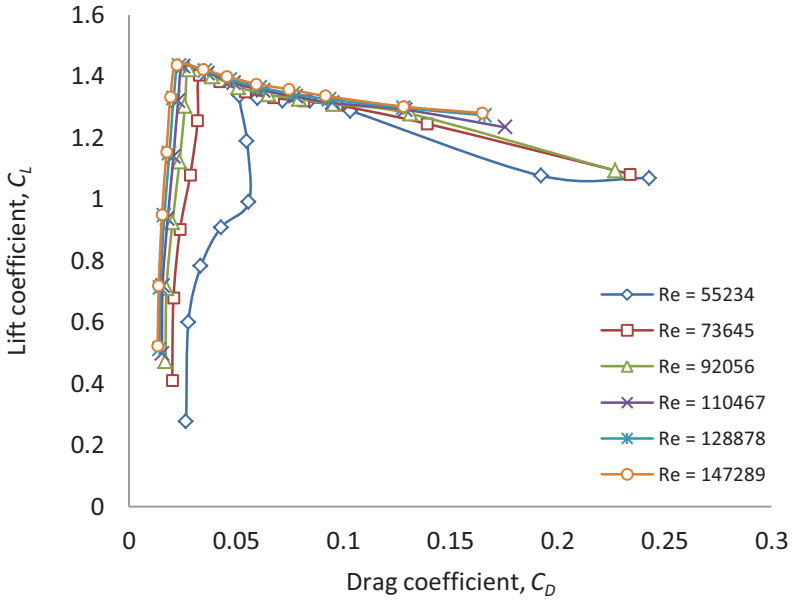

Fig. A1.21 Drag polar plot – lift vs. drag at various Reynolds number

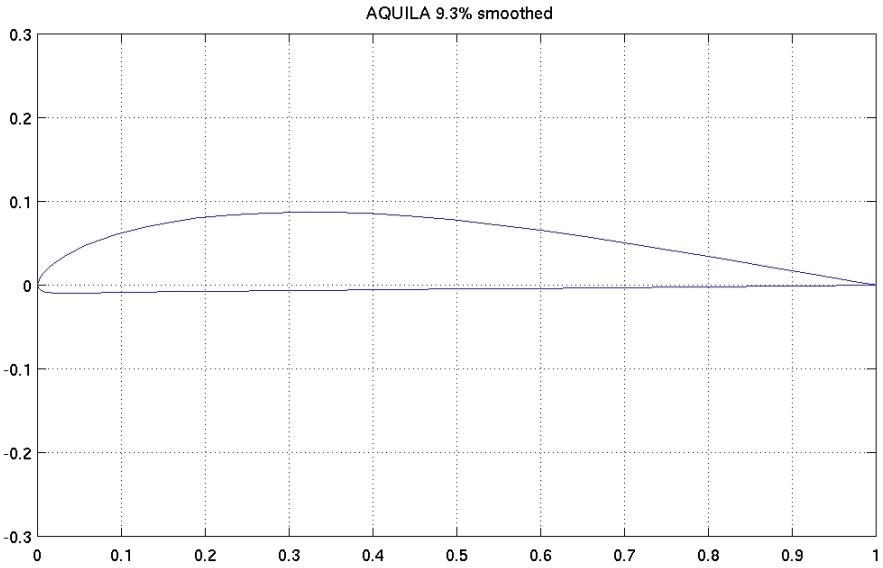

Fig. A1.22 A8 - aquilasm AQUILA R/C sailplane airfoil [43]

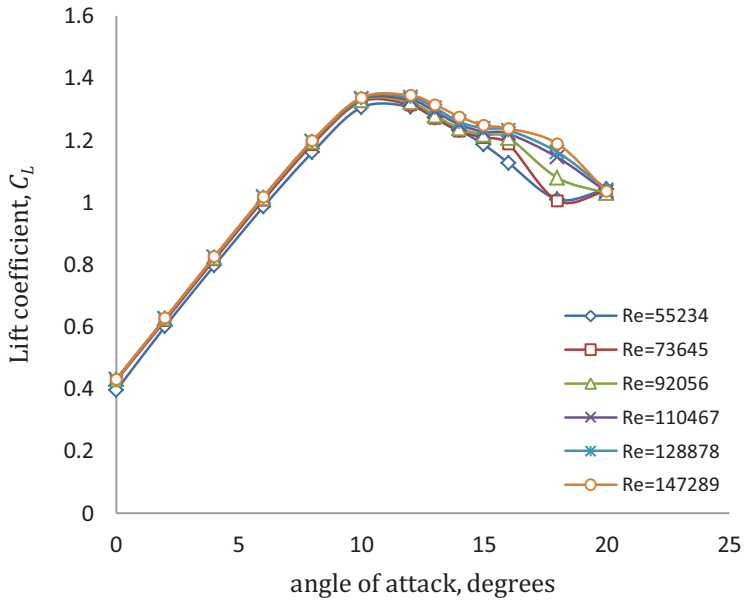

Fig. A1.23 Graph of lift vs. angle of attack at various Reynolds number

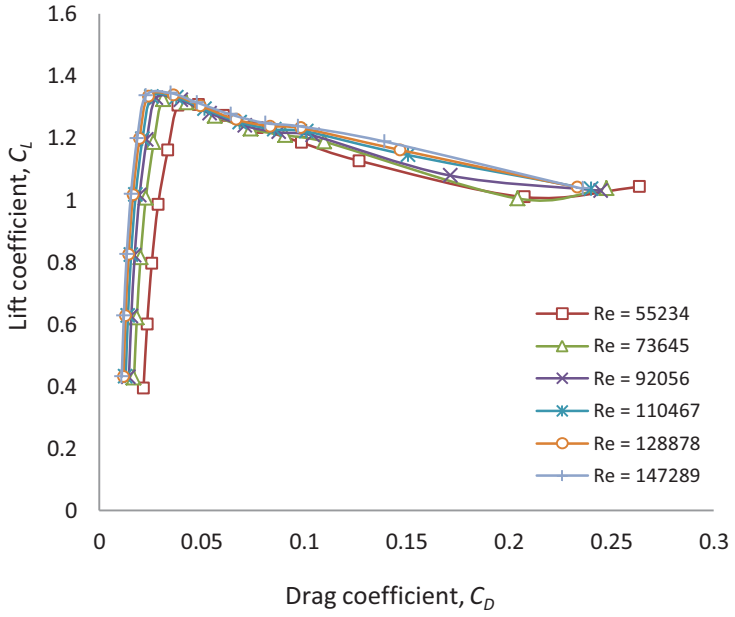

Fig. A1.24 Drag polar plots – lift vs. drag at various Reynolds number

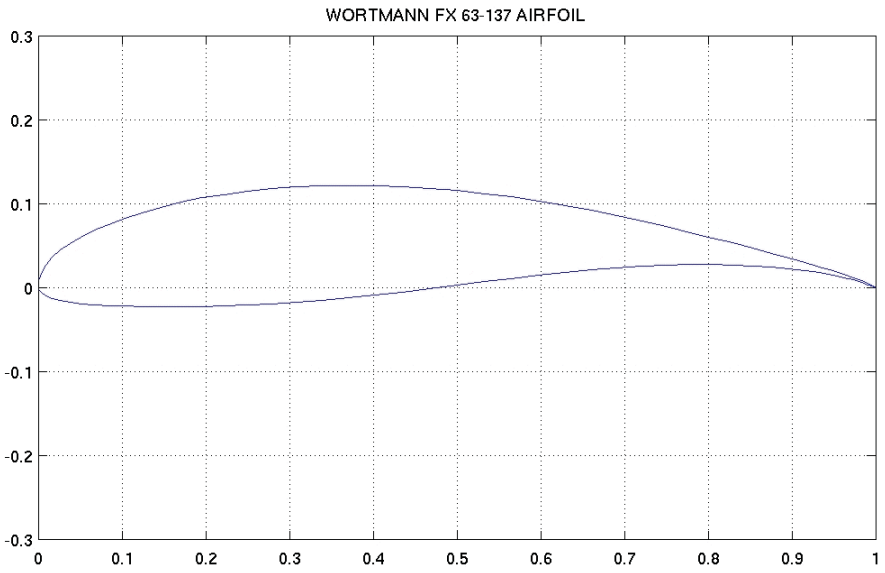

Fig. A1.25 A9 - FX 63-137 Wortmann human power aircraft airfoil (Liver Puffin) airfoil [43]

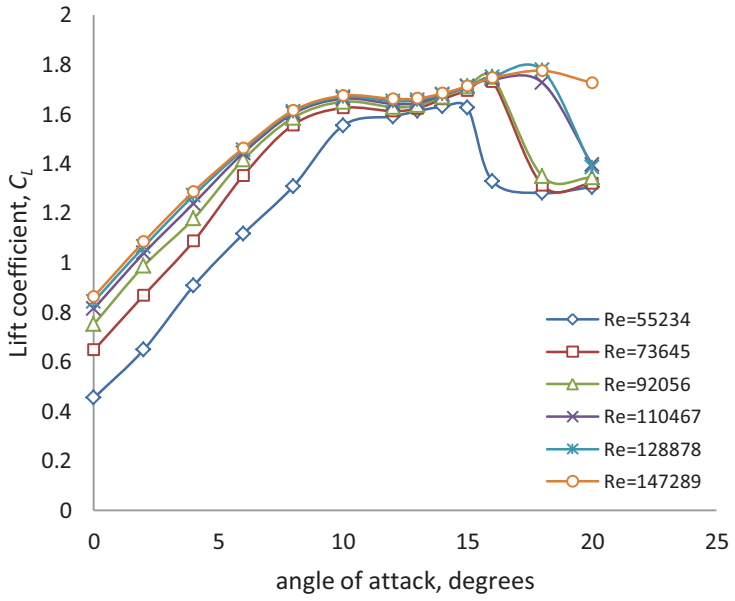

Fig. A1.26 Graph of lift vs. angle of attack at various Reynolds number

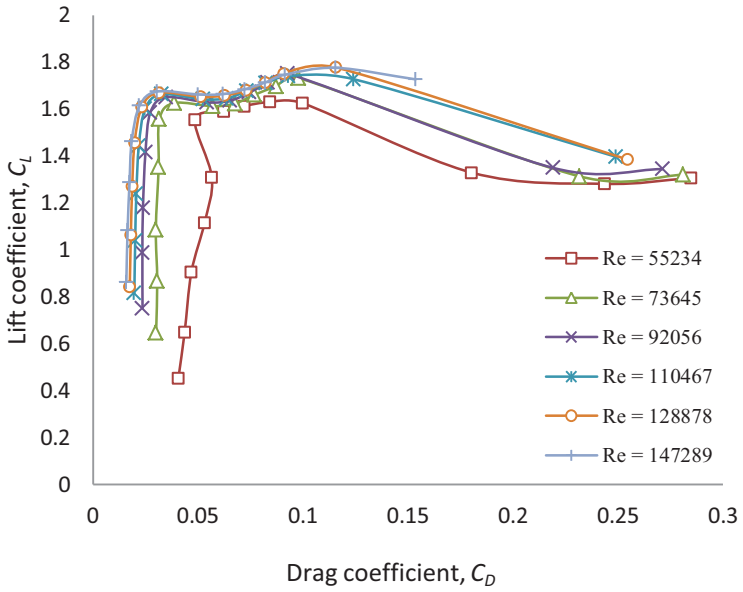

Fig. A1.27 Drag polar plots – lift vs. drag at various Reynolds number

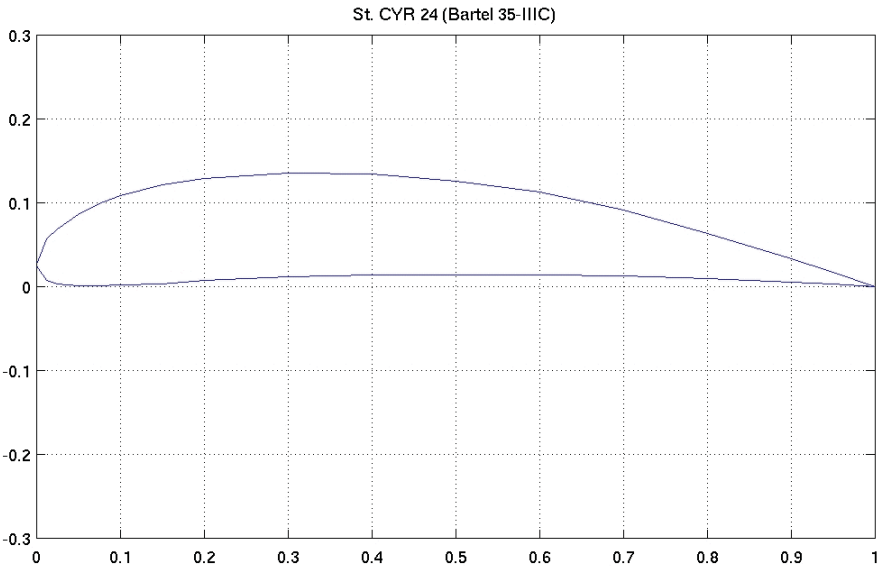

Fig. A1.28 A10 - stcyr24 St. CYR 24 (Bartel 35-IIIC) airfoil [43]

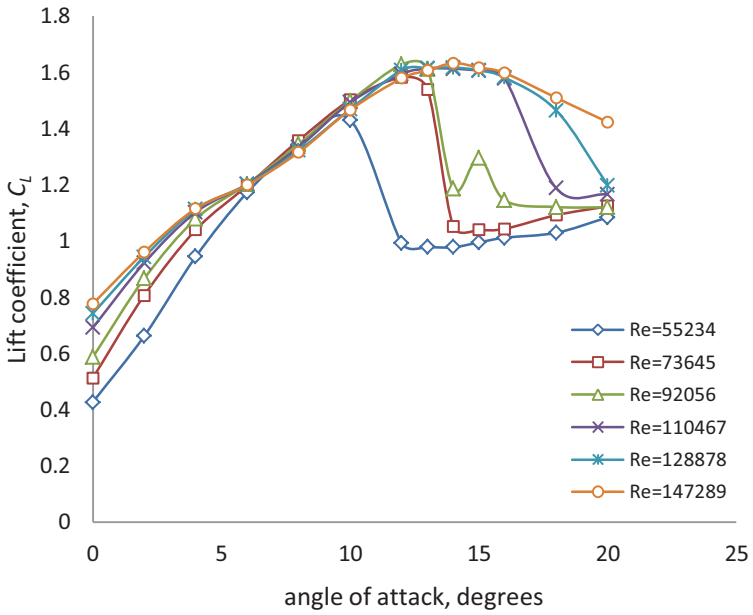

Fig. A1.29 Graph of lift vs. angle of attack at various Reynolds number

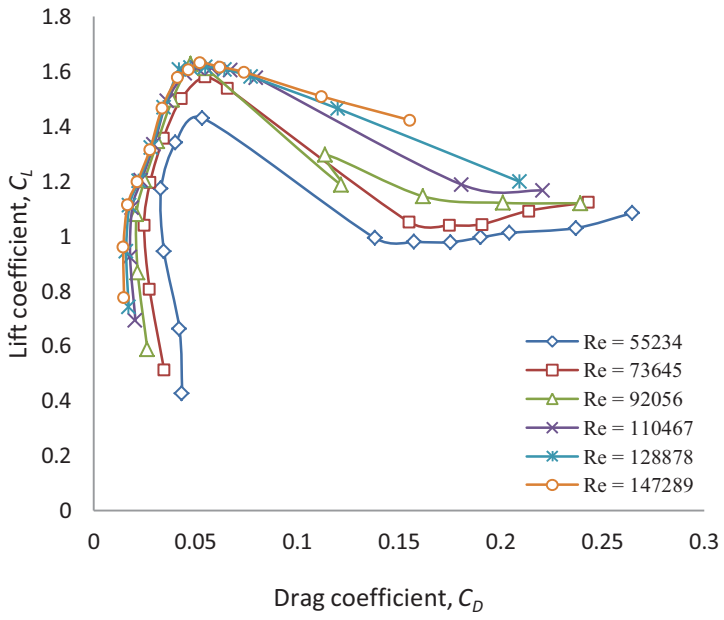

Fig. A1.30 Drag polar plots – lift vs. drag at various Reynolds number

Appendix 2

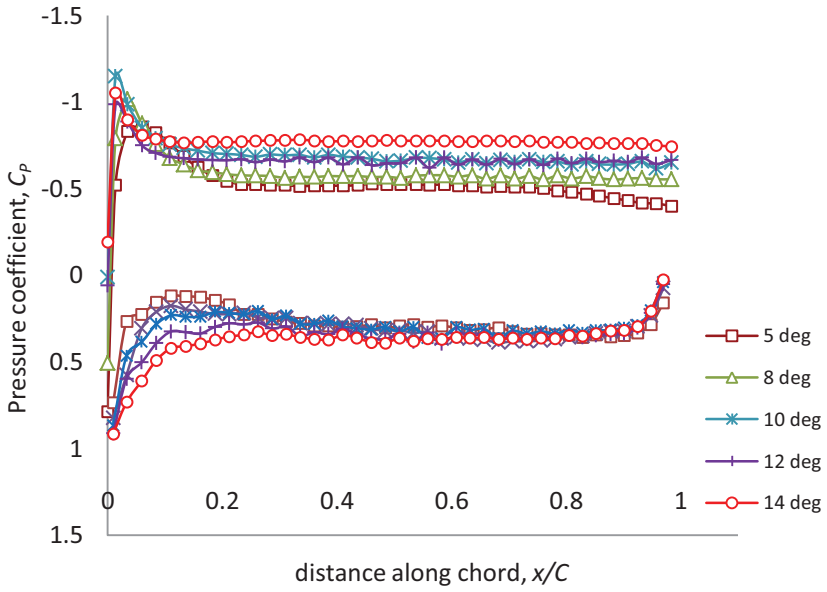

Fig. A2.1 Graph of pressure distribution vs. x/C at various angles of attack for Reynolds number = 55000 (V_∞ = 8.77m/s)

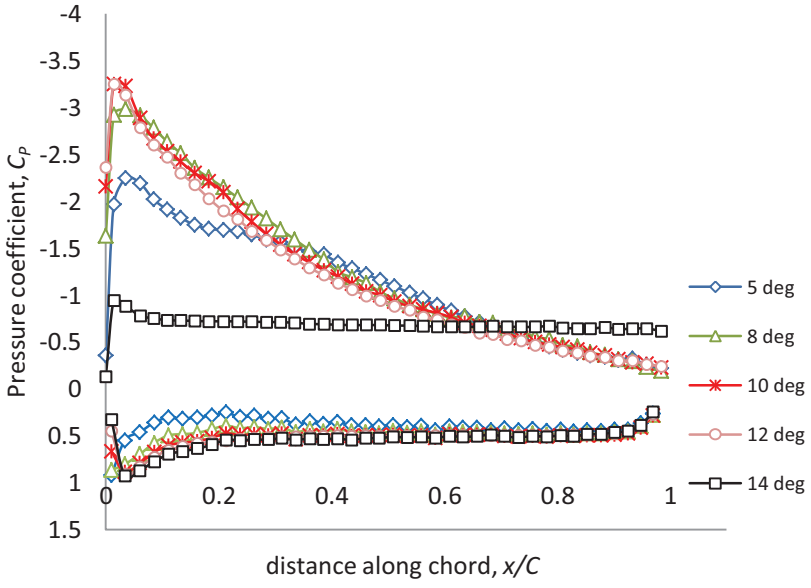

Fig. A2.2 Graph of pressure distribution vs. x/C at various angles of attack for Reynolds number = 92000 (V_∞ = 14.63m/s)

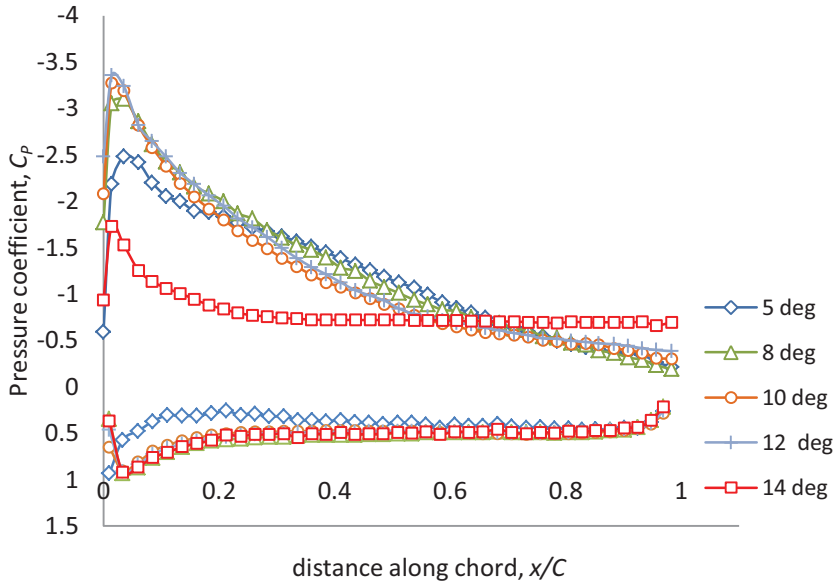

Fig. A2.3 Graph of pressure distribution vs. *x/C* at various angles of attack for Reynolds number = 150000 (V_∞ = 23.41m/s)

Appendix 3

Data logger program for recording wind speed, turbine voltage and current

```
'CR1000 Series Datalogger
'Program to monitor electrical output from 2-bladed HAWT research project of MSc(Eng)
student Ronit Singh
'program author: VT Buadromo
'date: 04/02/2011
'modified: 31/03/2011

'Declare Public Variables
Public PTemp, batt_volt, V_r1, V_r2, V_r3, V_r4, V_r5, V_shunt, windspeed
Public V_load, I_out, WindPower, EPowerIn

'Declare Constants
Const R_shunt=0.08
Const rho=1.184
Const Pi=3.141592654
Const RotorRad=0.63

'Define Data Tables
DataTable (LogrStat,1,-1)
       DataInterval (540,1440,Min,10)
       Minimum (1,batt_volt,FP2,0,False)
       Sample (1,PTemp,FP2)
EndTable
DataTable (WTData,1,-1)
       DataInterval (0,10,Sec,10)
       Average (1,V_load,FP2,False)
       Average (1,I_out,FP2,False)
       Average (1,windspeed,FP2,False)
       Average (1,WindPower,FP2,False)
       Average (1,EPowerIn,FP2,False)
EndTable

'No subroutines used in this program

'Main Program
BeginProg
       Scan (1,Sec,0,0)
              PanelTemp (PTemp,250)
              Battery (batt_volt)
              VoltDiff (V_r1,1,mV5000,1,True ,0,250,0.001,0)
              VoltDiff (V_r2,1,mV5000,2,True ,0,250,0.001,0)
              VoltDiff (V_r3,1,mV5000,3,True ,0,250,0.001,0)
              VoltDiff (V_r4,1,mV5000,4,True ,0,250,0.001,0)
              VoltDiff (V_r5,1,mV5000,5,True ,0,250,0.001,0)
              VoltDiff (V_shunt,1,mV5000,6,True ,0,250,0.001,0)
              PulseCount (windspeed,1,1 ,2,1,0.097924,0)
              If V_r1<>V_r2-0.01  Then
              V_r1=V_r2-0.01
              EndIf
              V_load=V_r1+V_r2+V_r3+V_r4+V_r5
              I_out=V_shunt/R_shunt
              WindPower=0.5*rho*Pi*RotorRad^2*windspeed^3
              EPowerIn=V_load*I_out

              'Call Output Tables
              CallTable LogrStat
              CallTable WTData
       NextScan
EndProg
```

Wind speed statistics

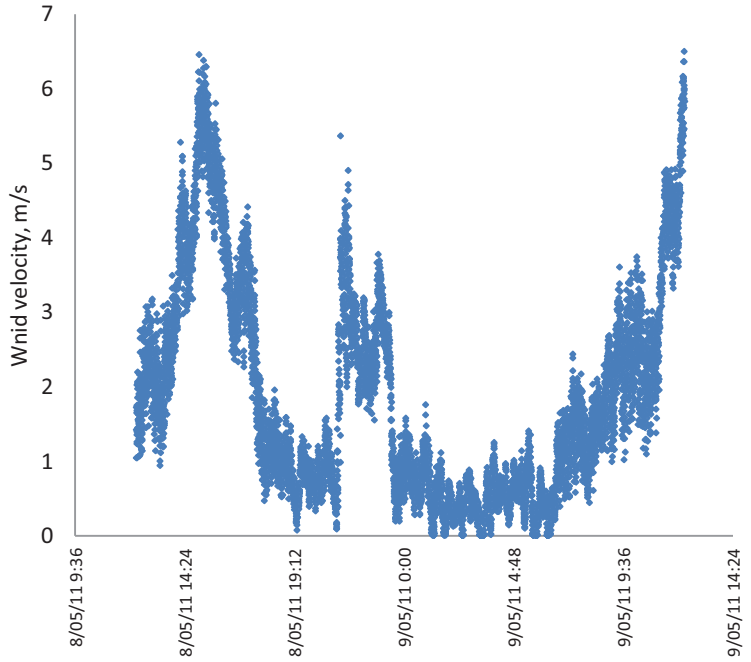

Fig. A3.1 Wind speed variation vs. time during 15° blade pitch angle setting

Table A3.1 24hour statistics during 15° blade pitch angle setting

Mean wind speed (m/s)	1.86
Maximum 10-sec gust (m/s)	6.49
Std. Dev. of wind speed (m/s)	1.43
Mean power density (W/m^2)	3.81

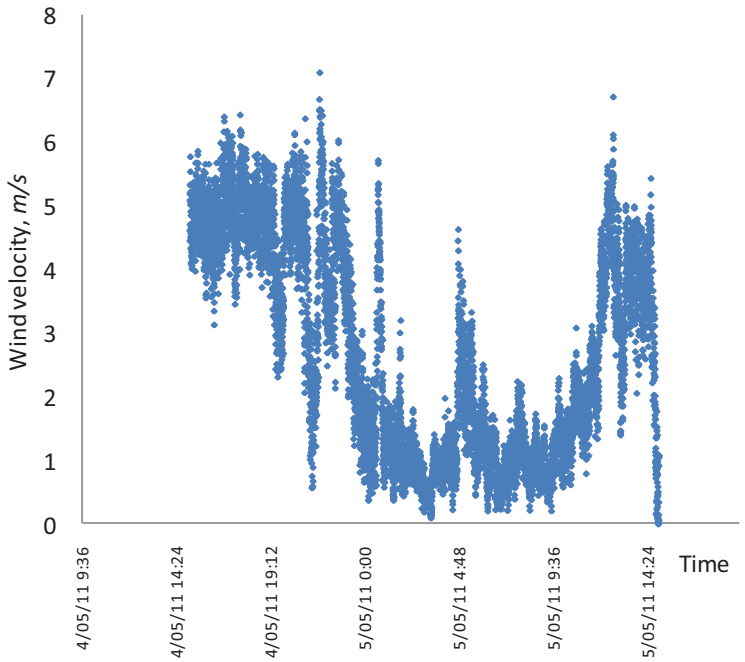

Fig. A3.2 Wind speed variation vs. time during 18° blade pitch angle setting

Table A3.2 24hour statistics during 18° blade pitch angle setting

Mean wind speed (m/s)	2.72
Maximum 10-sec gust (m/s)	7.11
Std. Dev. of wind speed (m/s)	1.69
Mean power density (W/m^2)	11.92

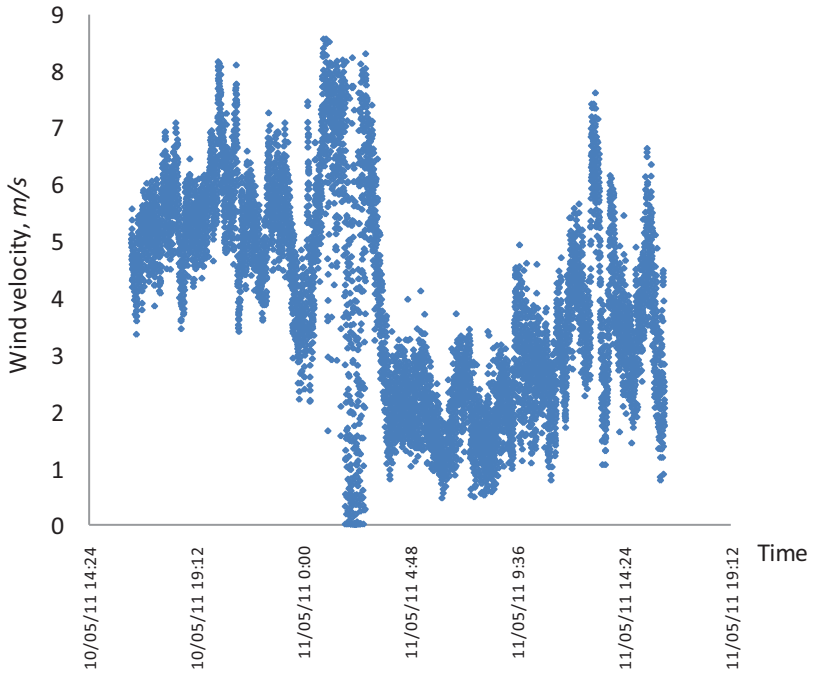

Fig. A3.3 Wind speed variation vs. time during 20° blade pitch angle setting

Table A3.3 24hour statistics during 20° blade pitch angle setting

Mean wind speed (m/s)	3.94
Maximum 10-sec gust (m/s)	8.56
Std. Dev. of wind speed (m/s)	1.81
Mean power density (W/m^2)	36.22

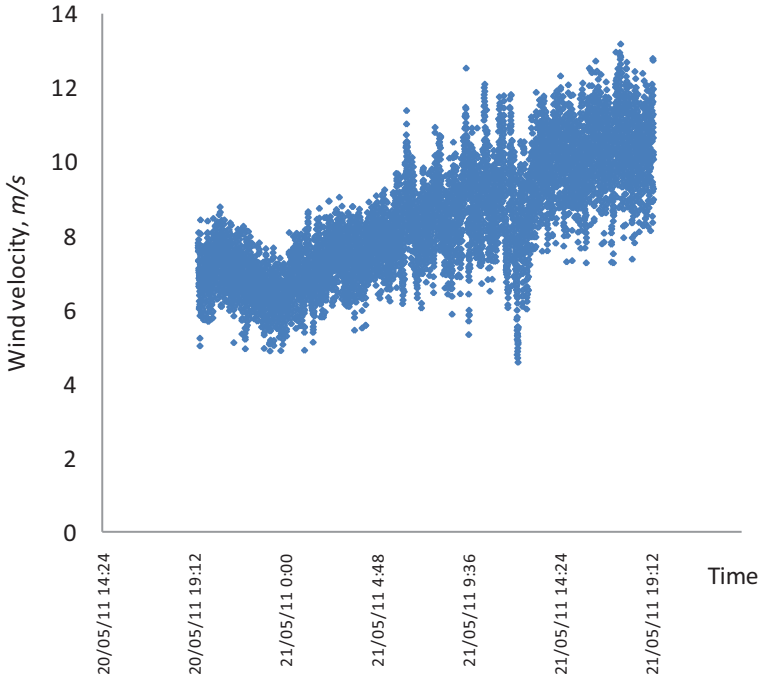

Fig. A3.4 Wind speed variation vs. time during 20° blade pitch angle setting during heavy gust

Table A3.4 24hour statistics during 20° blade pitch angle setting (heavy gust)

Mean wind speed (m/s)	8.39
Maximum 10-sec gust (m/s)	13.15
Std. Dev. of wind speed (m/s)	1.56
Mean power density (W/m^2)	349.75

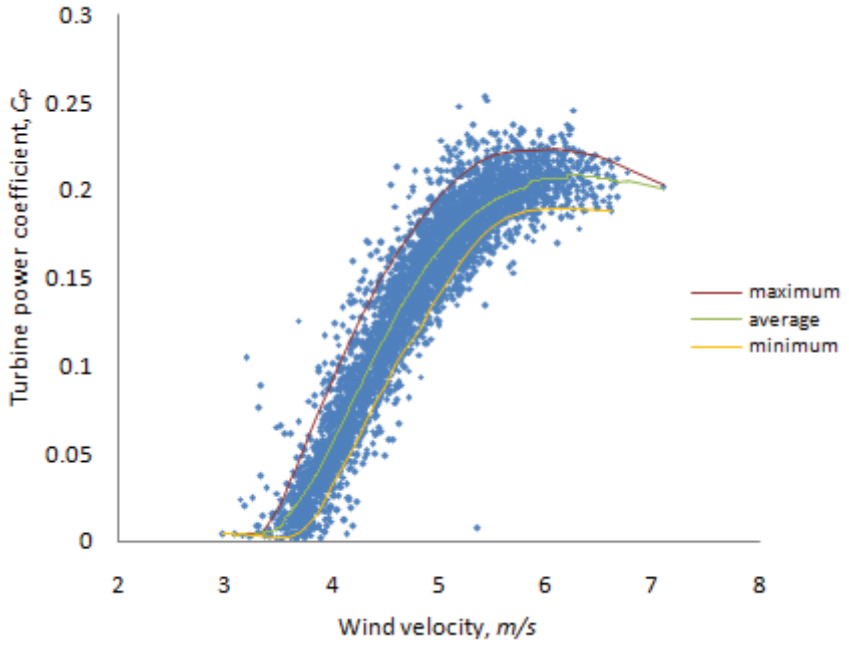

Fig. A3.5 Wind turbine power coefficient variation vs. wind speed for 15° pitch angle

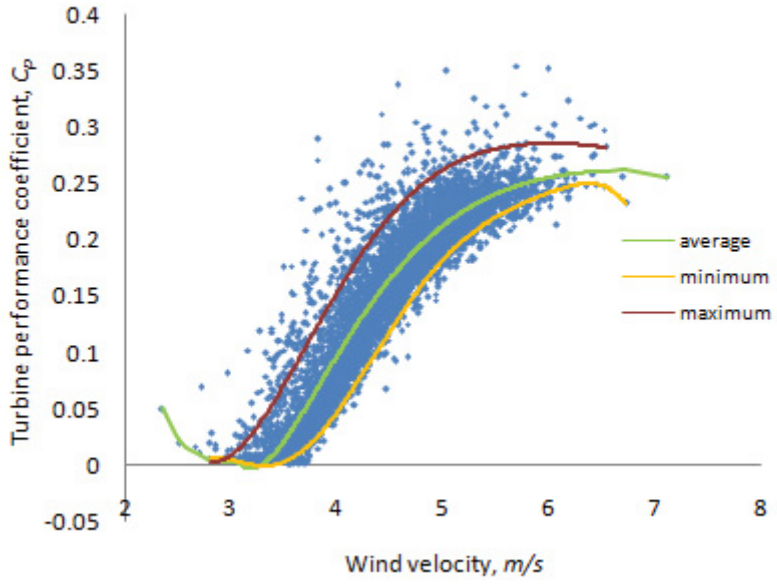

Fig. A3.6 Wind turbine power coefficient variation vs. wind speed for 18° pitch angle

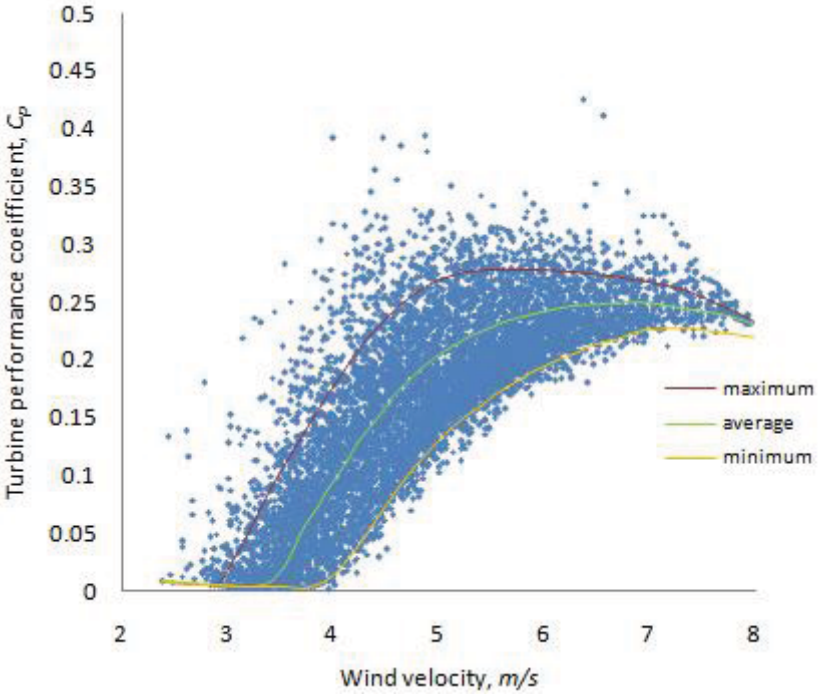

Fig. A3.7 Wind turbine power coefficient variation vs. wind speed for 20° pitch angle